OPTICAL REFERENCE GYRO CHARACTERIZATION AND PERFORMANCE ENHANCEMENT

by

Christopher Richard Doerr

Submitted to the

DEPARTMENT OF ELECTRICAL ENGINEERING AND COMPUTER SCIENCE

in partial fulfillment of the requirements

for the degrees of

BACHELOR OF SCIENCE

and

MASTER OF SCIENCE

at the

MASSACHUSETTS INSTITUTE OF TECHNOLOGY

June, 1990

Signature of Author _____
Department of Electrical Engineering and Computer Science, May 15, 1990

Certified by _____
W. M. Siebert
Thesis Supervisor

Certified by _____
T. T. Chien
Technical Supervisor, The Charles Stark Draper Laboratory, Inc.

Accepted by _____
Arthur C. Smith, Chair, Department Committee on Graduate Students

OPTICAL REFERENCE GYRO CHARACTERIZATION

AND PERFORMANCE ENHANCEMENT

by

Christopher Richard Doerr

Submitted to the Department of Electrical Engineering and Computer Science on May 1, 1990 in partial fulfillment of the requirements for the Degrees of Master of Science and Bachelor of Science in Electrical Engineering and Computer Science.

ABSTRACT

The Optical Reference Gyro (ORG), a dry-tuned two-degree-of-freedom gyroscope, has a light beam emanating from its rotor along the rotor spin axis. The goal was to measure and improve the performance of this beam for use in inertially stabilized pointing systems. The isolation of the beam from gyro case disturbances is investigated. It was found most of the rotor-to-case coupling is due to gas torques. The noise in the beam is characterized. It was found nearly all of the noise is contained at the spin frequency. The rest of the noise is primarily made up of spin-frequency harmonics, light source noise, air noise, and gas noise. The design, construction, and performance of two types of a special phase-locked loop notch filter that removes the spin-frequency noise is described. One type electronically subtracts the noise from the signal, and the other torques the ORG rotor to remove the noise. It was found this notch filter could reduce the spin-frequency noise to the beam noise floor while affecting only the signal within ±1 Hz of the spin frequency.

Thesis Supervisor: William M. Siebert
Title: Ford Professor of Engineering in Electrical Engineering and Computer Science

Acknowledgments

I am very thankful to my parents, who always supported me in my endeavors and who always stressed the importance of a good education. I am thankful to the United States of America for paying my tuition as an undergraduate. I am thankful to the Charles Stark Draper Laboratory for paying my tuition as a graduate student and giving me a great place to work in and great people and equipment to work with. I am thankful to Dale Woodbury for helping me throughout the entire thesis and teaching me to never take anything for granted and to never believe something until I have proven it myself. I am thankful to Professor William Siebert for being by thesis supervisor and looking out for me. I am thankful to Tom Thorvaldsen for funding my project and helping me. I am thankful to Mike Luniewicz for answering all my questions and giving me advice. I am thankful to many other people for helping me, including Rich Walker, Steve Nichols, Ray Carroll, Paul Tuck, Steve Christensen, Adrian Stecyk, Bruno Nardelli, Jim Hacunda, Andy Brabson, Dan Chang, Bill Sartanowicz, and many others.

I am most thankful to T. T. Chien, my supervisor. He worked very hard for me and helped me throughout my entire thesis. He taught me many things, one of which is to always be in control of what I am doing. To him, I am very grateful.

This research was done at The Charles Stark Draper Laboratory, Inc. under IR&D #18419.

Table of Contents

List of Tables

List of Figures

1 Introduction

1.1 The Optical Reference Gyro

Suppose an astronomer is looking at a very faint star. If the platform the telescope and astronomer are sitting on is not very rigid, the image of the star will jitter around. But if a very still light beam, a pseduo-star, was sent through the telescope, it could be used to stabilize the real star image. This could be done by placing a steerable mirror at the telescope output. The telescope image would reflect off the mirror into an optical detector. If the pseudo-star moved on the detector, the mirror could be steered to bring the pseudo-star back. Then the astronomer could look into the mirror and watch the real star without the image moving.

The Optical Reference Gyro (ORG) (see figs. 1.1-1, 1.1-2, and 1.1-3) can create the very still light beam. It does this by launching the beam from the center of a spinning wheel. A spinning wheel prefers to maintain its orientation in inertial space. Thus, ideally, the light beam emanating from the wheel always points in the same direction in inertial space.

The spinning wheel is actually a dry-tuned, two degree-of-freedom gyroscope. The light beam is created from a monochromatic light source at the back of the gyro. The light enters the inside of the rotor through a pinhole and is collimated into a beam by a lens at the top of the rotor.

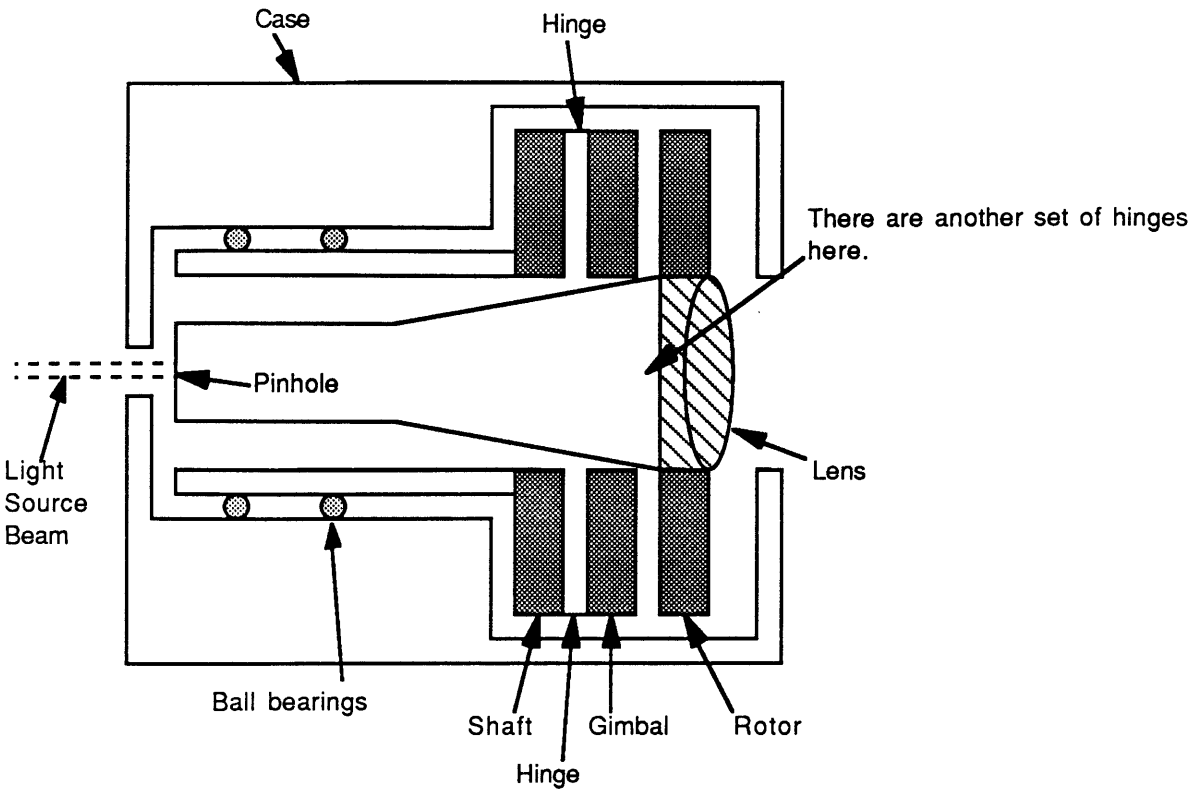

Figure 1.1-1. Simplified drawing of cross-section of ORG. The light enters through the pinhole and is collimated by the lens. The beam ends up using the rotor as an inertially stable platform.

It is desirable that the rotor orientation remain fixed in inertial space no matter how the gyro case is moved. This is achieved by using a gimbal ring to connect the rotor to the motor shaft. The rotor is connected to the gimbal so the rotor may pivot with respect to the gimbal. Likewise, the gimbal is connected to the shaft so it may pivot also, but on an axis perpendicular to the gimbal-rotor pivot. But these connections must not apply any additional torques to the rotor. These perfect "hinges" are achieved by using flexural springs as the connections and opposing these springs with negative dynamic springs. If the rotor is spun at a certain rate (89.4 Hz for the ORG), the mechanical and dynamic spring forces exactly cancel, and the rotor can move completely independently of the case motion, similar to a universal joint (see refs. 8 and 9).

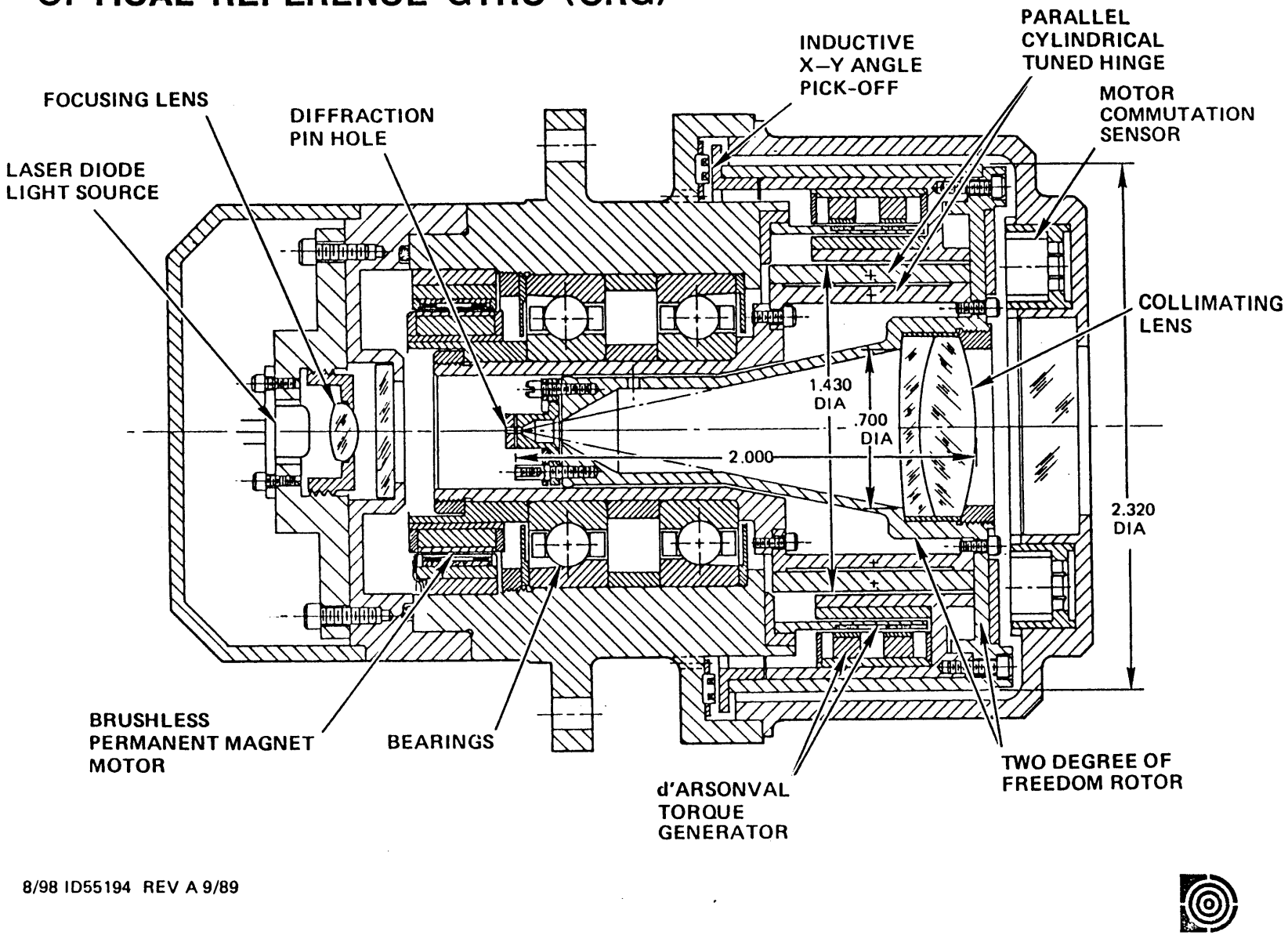

Figure 1.1-2. Detailed drawing of cross-section of ORG. Note: the laser diode light source and its focusing lens were not used for most of this thesis.

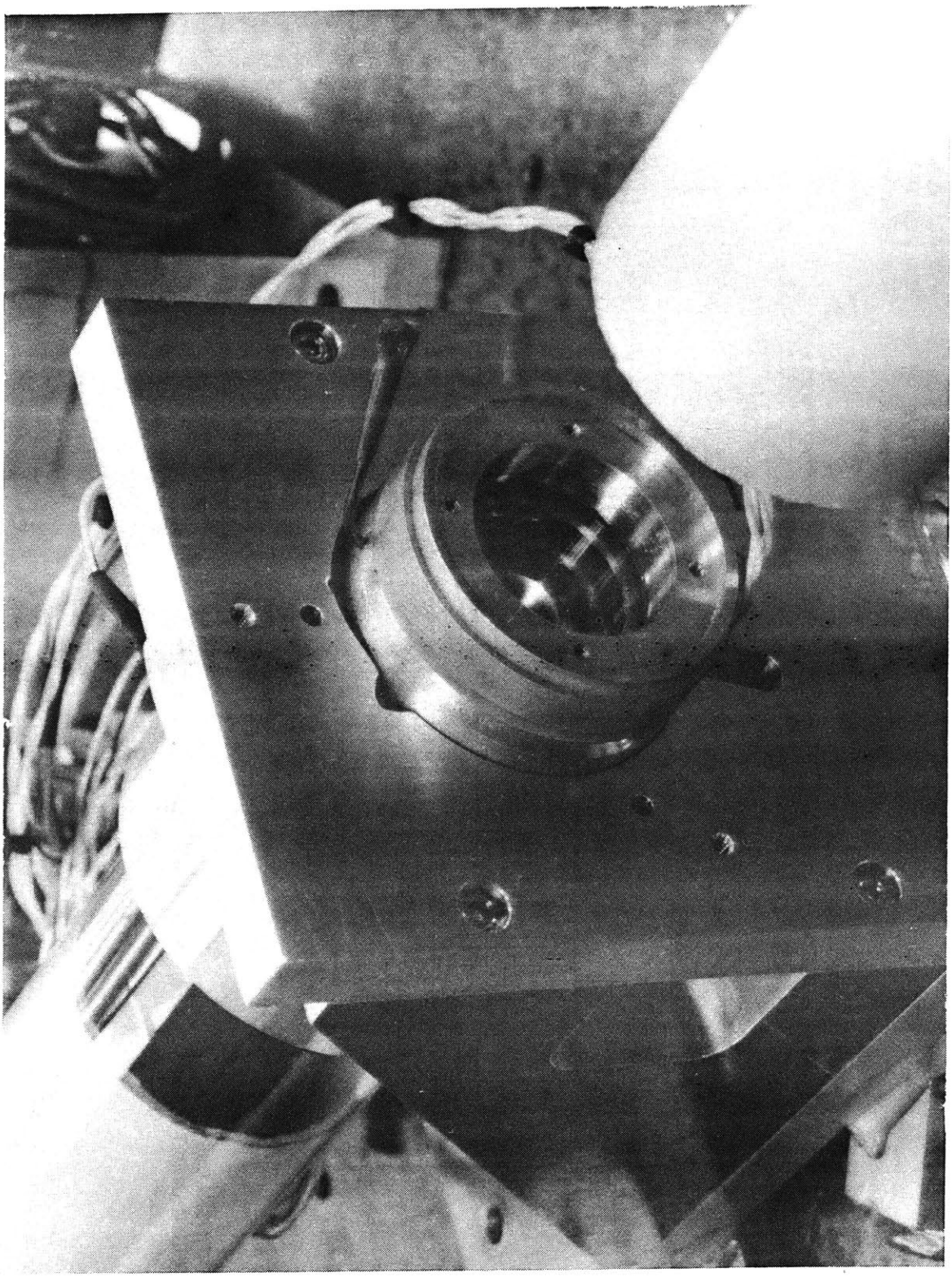

Figure 1.1-3. Photograph of back of ORG. This is where the light source is shined on the pinhole.

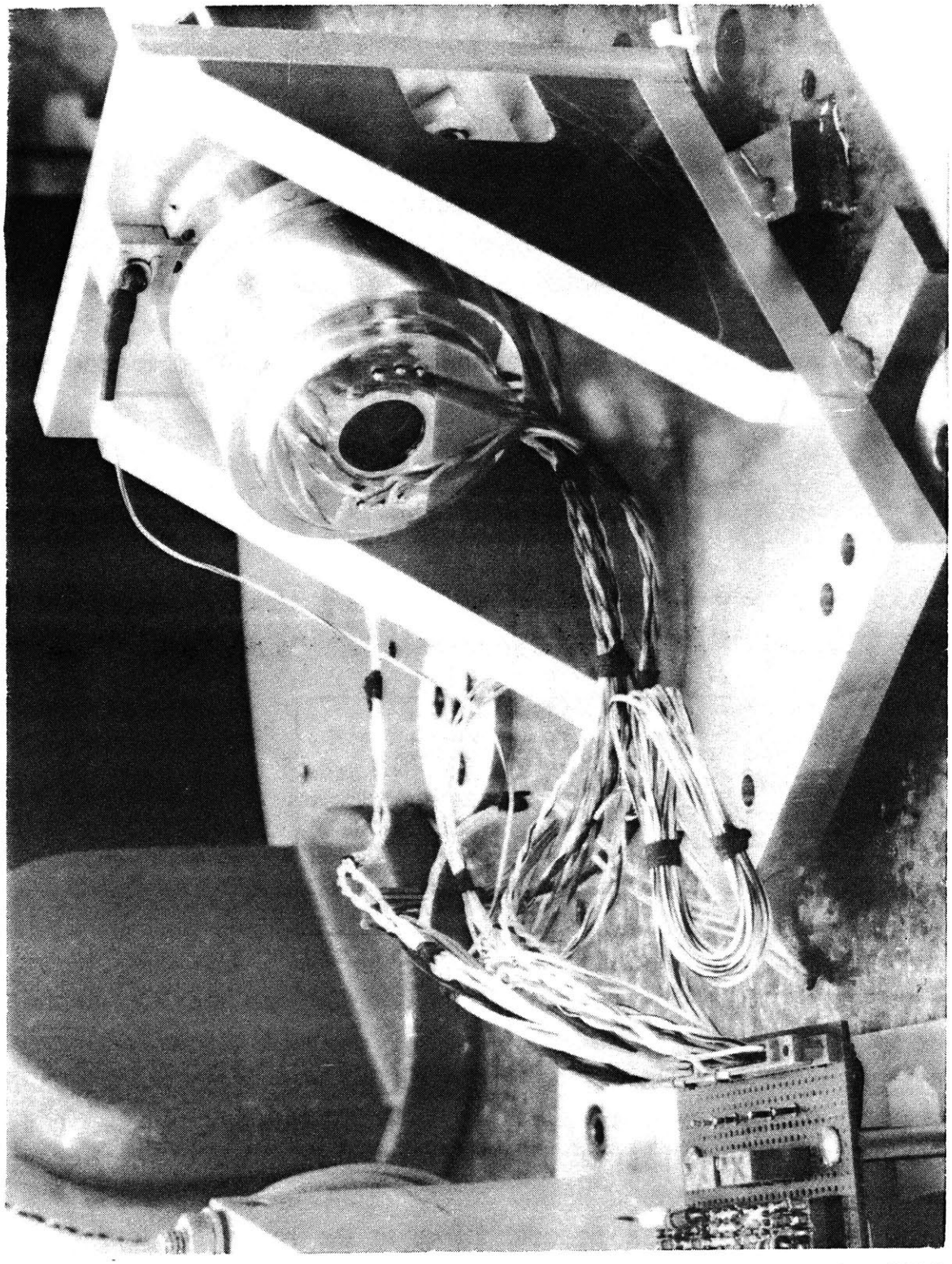

Figure 1.1-4. Photograph of front of ORG. This is where the ORG beam emerges.

As mentioned earlier, one use for the ORG is to stabilize a scene viewed through a telescope (see fig. 1.1-5) (see ref. 7). The telescope, mirror, and detector will have jitter due to mechanical resonances in the structure they are mounted on, so the scene image will be smeared out. In order to stabilize the scene image, an ORG beam is fed through the same optical path as the scene. The ORG output of the optical detector is used to steer the fast-steering mirror so the ORG beam spot remains at a fixed point on the detector. As a result of this steering, the scene will no longer be smeared.

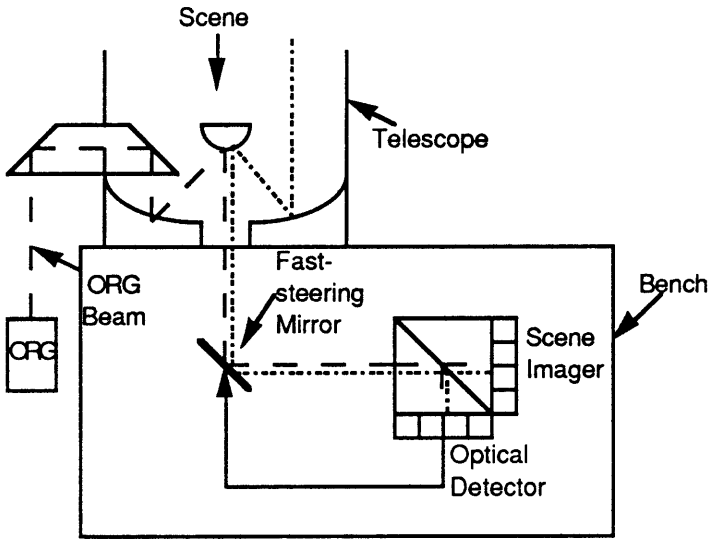

Figure 1.1-5. Possible application of the ORG. The ORG beam serves as an inertial reference or "pseudo-star" so that the scene may be viewed without smearing.

The main problem with the ORG is discrete-frequency noise. The ORG beam "wobbles", mainly because of misalignment of the optics with the natural spin-axis of the rotor. This "wobble" causes the optical detector to see a periodic signal at the rotor spin frequency that is much larger than the actual beam movement the detector must measure, and the fundamental frequency of this periodic signal is within the required stabilization bandwidth for many

applications. This discrete-frequency noise must be compensated for before the ORG can be used in an inertial stabilization application.

1.2 Thesis Goals

The goal of this thesis was to characterize and enhance the performance of an ORG prototype built by the Charles Stark Draper Laboratory. More specifically, the goals were to

1. characterize the noise in the ORG, both wide-band and discrete-frequency
2. study the performance of the ORG beam as a pseudo-star
3. find a way to reduce the discrete-frequency noise while minimizing the damage to the performance
4. find other ways to enhance the ORG performance.

1.3 Thesis Roadmap

This paper starts out by describing the basic principles of the ORG. In this section, the dynamics are modeled, the optics are described, and the optical detector used to measure the ORG beam is presented.

Next, the noise in the ORG outputs (the ORG beam and the electrical pick-offs that measure case-to-rotor angle) is examined. Measurements are given, and the sources of the noise are investigated.

Next, a device designed and built by the author that can reduce the discrete-frequency noise is described. The two modes of operation of the device, subtraction and torquing, are described, and the device performance is presented.

Then the performance of the ORG as pseudo-star is analyzed. An experiment measuring the isolation of the ORG rotor from ORG case

movement is described. The results of this experiment are given, and the causes of the rotor-to-case coupling are investigated.

Finally, conclusions and recommendations for improvements to the ORG are given.

2 Basic Principles of the ORG

This section presents the basic principles of the ORG. First, a model for the ORG dynamics is derived. Then the optics of the ORG are described. Finally, the operation of an optical detector to measure the ORG beam is described.

2.1 Dynamics

The ORG is a two-degree-of-freedom, dry-tuned gyro. The basic model for any two-degree-of-freedom, dry-tuned gyro is a free spinning wheel. See fig. 2.1-1.

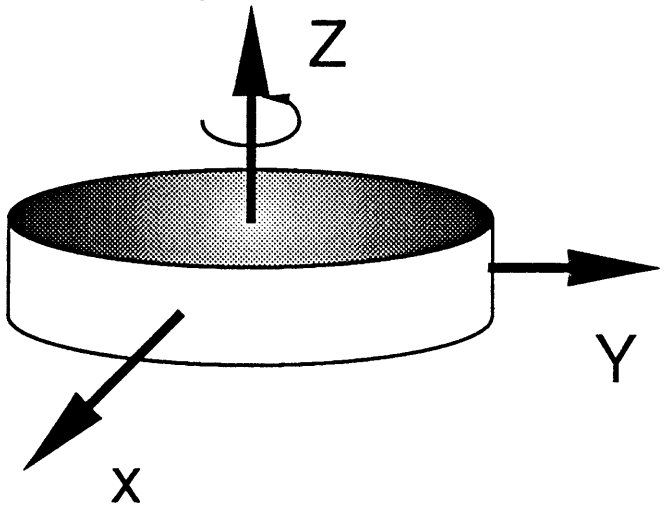

Figure 2.1-1. Simple representation of a two-degree-of-freedom gyro rotor.

It is shown in ref. 1 the dynamics of a wheel spinning in space are

$$M_x = I_x \dot{\omega}_x + H\omega_y \qquad (2\text{-}1)$$

$$M_y = I_y \dot{\omega}_y - H\omega_x \qquad (2\text{-}2)$$

where

M_x = torque applied to wheel about fixed x-axis
M_y = torque applied to wheel about fixed y-axis
I_x = moment of inertia about wheel x-axis
I_y = moment of inertia about wheel y-axis
ω_x = angular rate of wheel with respect to inertia about fixed x-axis
ω_y = angular rate of wheel with respect to inertia about fixed y-axis
H = angular momentum of wheel about wheel z-axis (spin axis).

Note that

$$H = I_z\omega_z \qquad (2\text{-}3)$$

where

I_z = moment of inertia about wheel z-axis
ω_z = angular rate of wheel about wheel z-axis.

The open-loop poles of this gyro model consist of two pure integrators and two poles on the jω-axis. The two poles on the jω-axis correspond to a wheel wobble called nutation. The two integrators show why a spinning wheel is a good inertial reference. The wheel maintains its orientation unless acted on by a torque. Thus the spinning wheel does nothing more than integrate torques applied to it.

But in reality, the wheel is attached to a shaft and is inside a gas-filled case. The attachment to the shaft and the gas cause extraneous torques on the rotor, and cause coupling between the case and wheel. With the help of refs. 1 and 2, it was found the model becomes

$$M_x = -(k_x - \omega_s^2 J)(\theta_x - \theta_{Cx}) + \omega_s c_p(\theta_y - \theta_{Cy}) + I_x \ddot{\theta}_x + H\dot{\theta}_y + c_d\dot{\theta}_x \qquad (2\text{-}4)$$

$$M_y = -(k_y - \omega_s^2 J)(\theta_y - \theta_{Cy}) - \omega_s c_p(\theta_x - \theta_{Cx}) + I_y \ddot{\theta}_y - H\dot{\theta}_x + c_d\dot{\theta}_y \qquad (2\text{-}5)$$

M_x = torque applied to rotor about case x-axis
M_y = torque applied to rotor about case y-axis
ω_s = ω_z = angular rate of rotor about spin axis
K_x and K_y = elastic restraint coefficients
c_p = gas damping coefficient
c_d = gas viscous damping coefficient
J = average gimbal z-axis quadruple moment
θ_x = angle of rotor with respect to inertia about inertia x-axis
θ_y = angle of rotor with respect to inertia about inertia y-axis
θ_{Cx} = angle of case with respect to inertia about inertia x-axis
θ_{Cy} = angle of case with respect to inertia about inertia y-axis.

Note: θ_x-θ_{Cx} and θ_y-θ_{Cy} are the rotor-to-case angles. If θ_x-θ_{Cx}=0 and θ_y-θ_{Cy}=0, then the rotor is in the center of the case.

Also note that bias torques have been neglected, since it is desired to only look at the dynamics and not the absolute position of the rotor.

The parameters for the ORG are

I_z = 1175 gm-cm (note: this was calculated from the geometry and density of the rotor and is not a precise number)

ω_z = 89.4 Hz

$H = I_z\omega_z$ = (1175 gm-cm)(2πx89.4 Hz) = 6.60×10^5 dyn-cm-s

nutation = 133 Hz (note: this is the resonant frequency of the gyro and was measured accurately from the gyro output)

$I_x = I_y$ = H/(nutation frequency) = $6.60 \times 10^5/(2\pi \times 133$ Hz) = 790 gm-cm.

The first terms in equations 2-4 and 2-5 are the spring restraints. The rotor is attached to the gimbal and the gimbal is attached to the shaft by torsional springs. These springs are opposed by "dynamic springs". If $K_x \neq K_y$ or the rotor is not spun at the tuned speed (i.e. $\omega_s \neq (K/J)^{0.5}$), then the physical springs and "dynamic springs" won't exactly cancel, and there will be a residual torque. If the rotor is spun too slowly, the rotor will have a tendency to return to the center of the case, and if it is spun too fast, the rotor will have a tendency to move away from the center.

The second terms in equations 2-4 and 2-5 are the gas torques. If the rotor moves off of the gas null in the case, the distance between the rotor and the inner wall of the case will be smaller on one side. Since the rotor is spinning, it will build up a higher pressure on one side of the rotor. This pressure will tend to push the rotor back towards the center of the case.

The third and fourth terms in equations 2-4 and 2-5 are straight from equations 2-1 and 2-2.

The fifth term is the damping from the gas. Without this term, the model is unstable.

To obtain the gas coefficient c_p, it is desired to get a transfer function $\theta_x(s)/\theta_{Cx}(s)$. Assume the gyro is perfectly tuned (i.e. $K_x=K_y=\omega_s^2 J$) and let $M_x=M_y=0$. Then equations 2-4 and 2-5 become

$$0=\omega_s c_p(\theta_y-\theta_{Cy})+I_x\ddot{\theta}_x+H\dot{\theta}_y+c_d\dot{\theta}_x \qquad (2\text{-}6)$$

$$0=-\omega_s c_p(\theta_x-\theta_{Cx})+I_y\ddot{\theta}_y-H\dot{\theta}_x+c_d\dot{\theta}_y. \qquad (2\text{-}7)$$

Taking the Laplace transform of both sides, one obtains

$$0=\omega_s c_p(\theta_y-\theta_{Cy})+I_x s^2\theta_x+Hs\theta_y+c_d s\theta_x \qquad (2\text{-}8)$$

$$0=-\omega_s c_p(\theta_x-\theta_{Cx})+I_y s^2\theta_y-Hs\theta_x+c_d s\theta_y. \qquad (2\text{-}9)$$

Now assume the case is moving, but only about the x-axis, i.e. $\theta_{Cx}\neq 0$, $\theta_{Cy}=0$. Solving equation 2-8 for θ_y, one obtains

$$\theta_y(s)=\frac{I_x s^2+c_d s}{Hs+\omega_s c_p}\theta_x(s). \qquad (2\text{-}10)$$

This shows for low frequencies, $\theta_y(s)\approx 0$. Thus, equation 2-9 becomes

$$\frac{\theta_x(s)}{\theta_{Cx}(s)}=\frac{\omega_s c_p}{Hs+\omega_s c_p}. \qquad (2\text{-}11)$$

This means if the gyro case is rotated back and forth, the rotor will follow the case for frequencies below $\omega_s c_p/H$ rad/s. This also means if the rotor is displaced from the center of the case, it will return to the center of the case with a time constant of $H/\omega_s c_p$ sec. Thus by knowing the time constant, H, and ω_s, one can calculate c_p. Table 2-1 displays some time constants that were measured for different amounts and types of gas inside the ORG. Note the bandwidths of θ_x/θ_{Cx} were also measured, and they were nearly

exactly what they should have been as predicted by the time constants.

Gas Inside ORG	Time Const. (sec)	Bandwidth (Hz)	c_p (dyn-cm-s)
air at 1 atm	1.3	0.12	904
He at 2 psi	2.7	0.059	435
air at ≈7μm*	9.8	0.016	120
air at ≈6μm*	18	0.0088	65

* denotes pressure in height of mercury. Note: 6 or 7 μm is a near vacuum and is hereafter referred to as a vacuum.

Table 2-1. Rotor characteristics for various amounts and types of gas inside ORG.

There is no simple way to measure the viscous damping coefficient, c_d, but it was found from calculations that if $c_d<0.7c_p$, the model is unstable. Since the ORG was stable, it must be that $c_d>0.7c_p$. Setting $c_d=c_p$ produced results that closely matched the measured ones. Thus for the simulations, $c_d=c_p$.

Now the parameters for the spring restraint torques must be found. Neither K_x, K_y, or J can be measured easily. But from the geometry and type of metal used in the springs, K_x and K_y were calculated in ref. 1 to be about $3.5\text{x}10^5$ dyn-cm/rad. Since the tuned speed is 89.4 Hz, this implies

$$J = K/\omega_s^2 = (3.5\text{x}10^5 \text{ dyn-cm/rad})/(2\pi\text{x}89.4 \text{ Hz})^2 = 1.1 \text{ gm-cm}.$$

To perform simulations using the model, equations 2-4 and 2-5 can be written in a state-space form as follows:

$$\begin{bmatrix} \dot{\omega}_x \\ \dot{\omega}_y \\ \dot{\theta}_x \\ \dot{\theta}_y \end{bmatrix} = \begin{bmatrix} -\frac{C_d}{I_x} & -\frac{H}{I_x} & \frac{k_x - \omega_s^2 J}{I_x} & -\frac{\omega_s C_p}{I_x} \\ \frac{H}{I_y} & -\frac{C_d}{I_y} & \frac{\omega_s C_p}{I_y} & \frac{k_y - \omega_s^2 J}{I_y} \\ 1 & 0 & 0 & 0 \\ 0 & 1 & 0 & 0 \end{bmatrix} \begin{bmatrix} \omega_x \\ \omega_y \\ \theta_x \\ \theta_y \end{bmatrix} + \begin{bmatrix} \frac{1}{I_x} & 0 \\ 0 & \frac{1}{I_y} \\ 0 & 0 \\ 0 & 0 \end{bmatrix} \begin{bmatrix} M_x \\ M_y \end{bmatrix} + \begin{bmatrix} -\frac{k_x - \omega_s^2 J}{I_x} & \frac{\omega_s C_p}{I_x} \\ -\frac{\omega_s C_p}{I_y} & -\frac{k_y - \omega_s^2 J}{I_y} \\ 0 & 0 \\ 0 & 0 \end{bmatrix} \begin{bmatrix} \theta_{Cx} \\ \theta_{Cy} \end{bmatrix}$$

(2-12)

Figs. 2.1-2 through 2.1-5 show bode plots of $\theta(j\omega)/M(j\omega)$ as generated by a computer simulation of the above system.

As one can see, the direct-axis transfer functions, θ_x/M_x and θ_y/M_y, start with a slope of -20 dB/decade and then fall off at -60 db/decade. The cross-axis transfer functions, θ_x/M_y and θ_y/M_x, start with a zero slope and then fall off at -40 dB/decade. It is interesting to note that the low-frequency phase of θ_x/M_x is +90°, while the low-frequency phase of θ_y/M_y is -90°. This shows that when torque is input into one axis, the rotor will move about both axes.

Figs. 2.1-6 through 2.1-9 show the measured transfer functions from the actual ORG.

The simulated transfer functions match the measured transfer functions well. The spike at 89 Hz (the spin speed) in the measured transfer functions is the spin-frequency noise that must be removed.

The θ/θ_C transfer functions tell how coupled the rotor is to the case and are analyzed in the "ORG Performance Study" section (section 4).

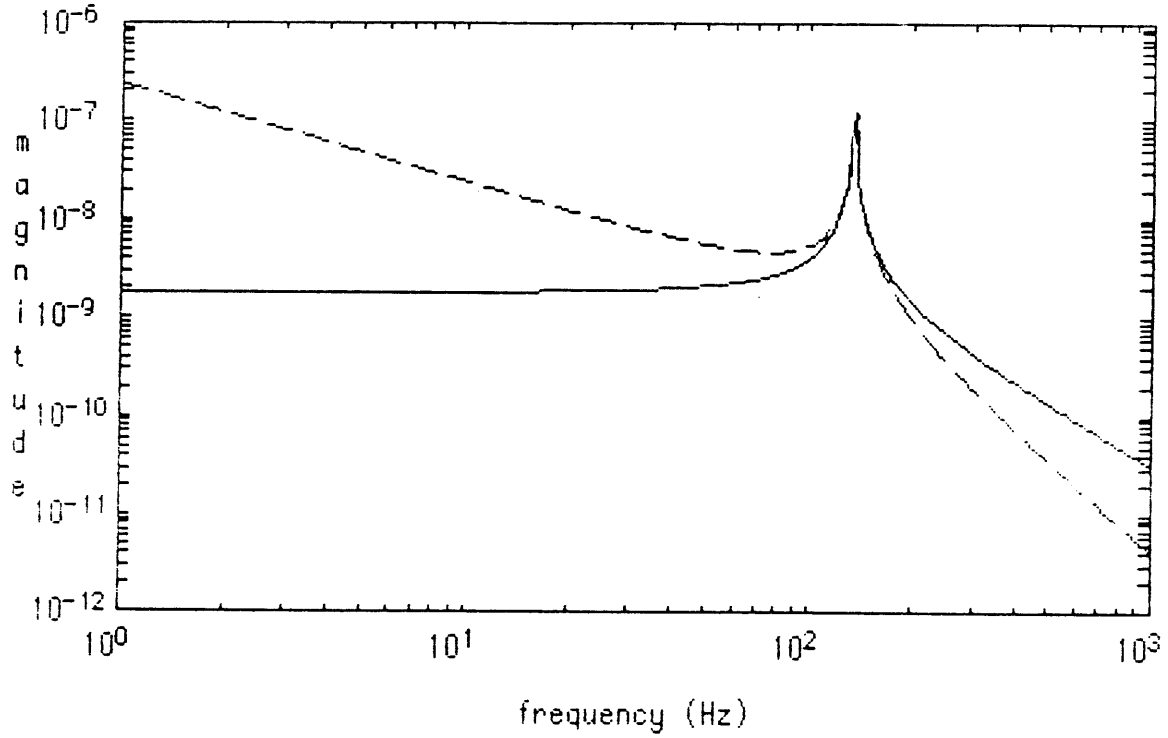

Figure 2.1-2. Solid line is $\theta x(j\omega)/Mx(j\omega)$. Dashed line is $\theta y(j\omega)/Mx(j\omega)$. Magnitude plot. ORG evacuated.

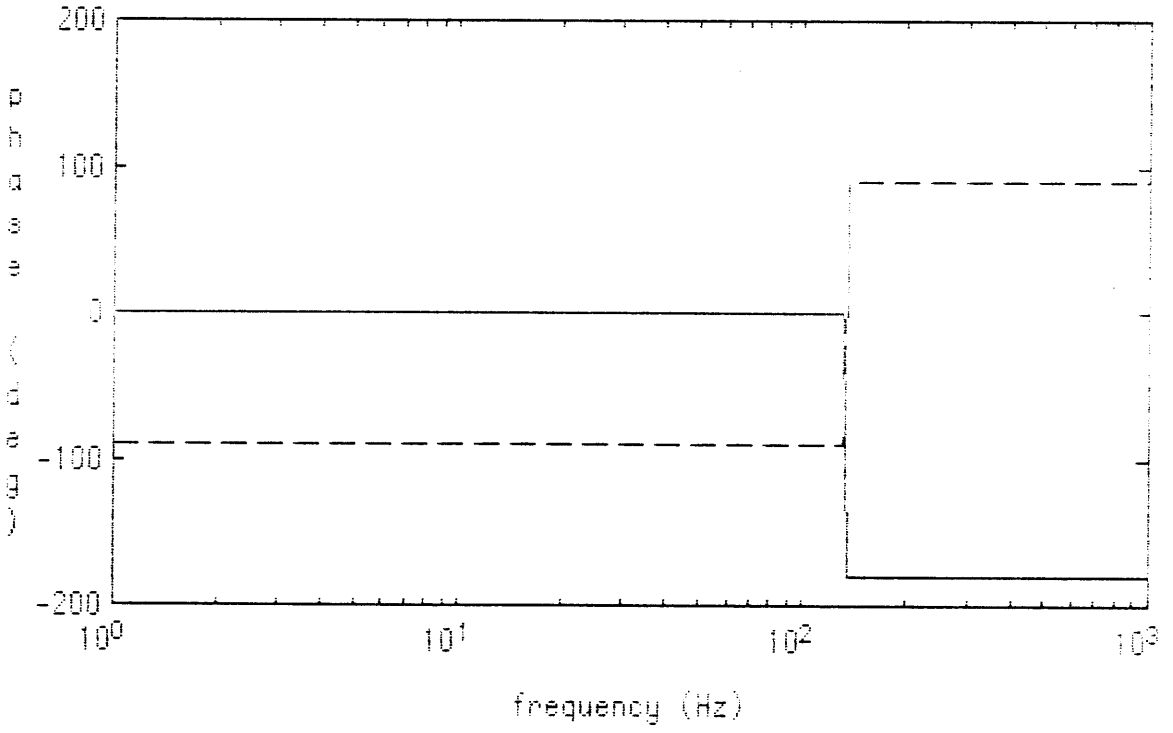

Figure 2.1-3. Solid line is $\theta x(j\omega)/Mx(j\omega)$. Dashed line is $\theta y(j\omega)/Mx(j\omega)$. Phase plot. ORG evacuated.

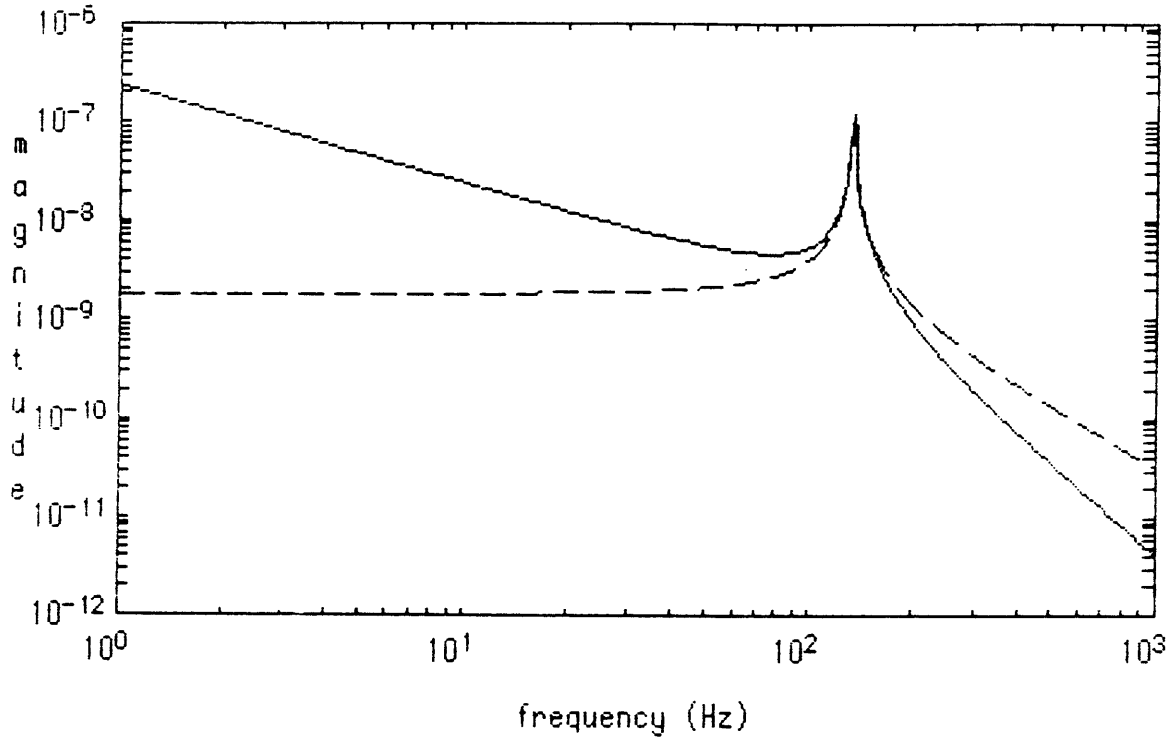

Figure 2.1-4. Solid line is $\theta x(j\omega)/My(j\omega)$. Dashed line is $\theta y(j\omega)/My(j\omega)$. Magnitude plot. ORG evacuated.

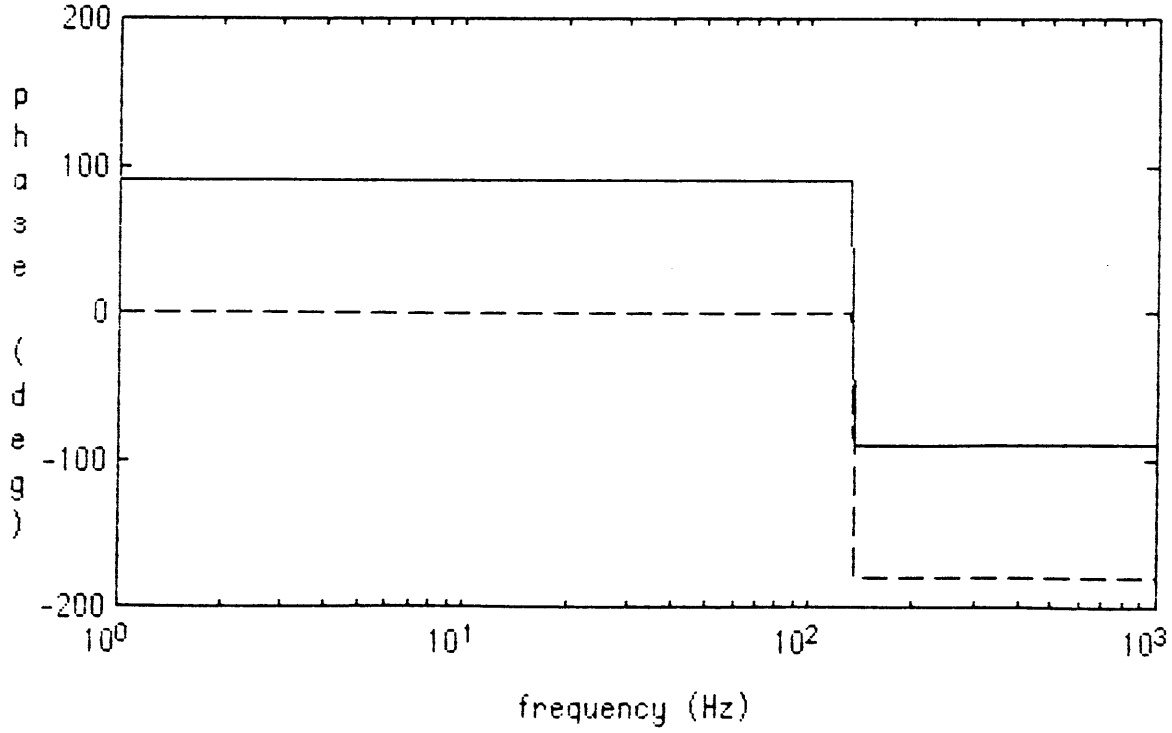

Figure 2.1-5. Solid line is $\theta x(j\omega)/My(j\omega)$. Dashed line is $\theta y(j\omega)/My(j\omega)$. Phase plot. ORG evacuated.

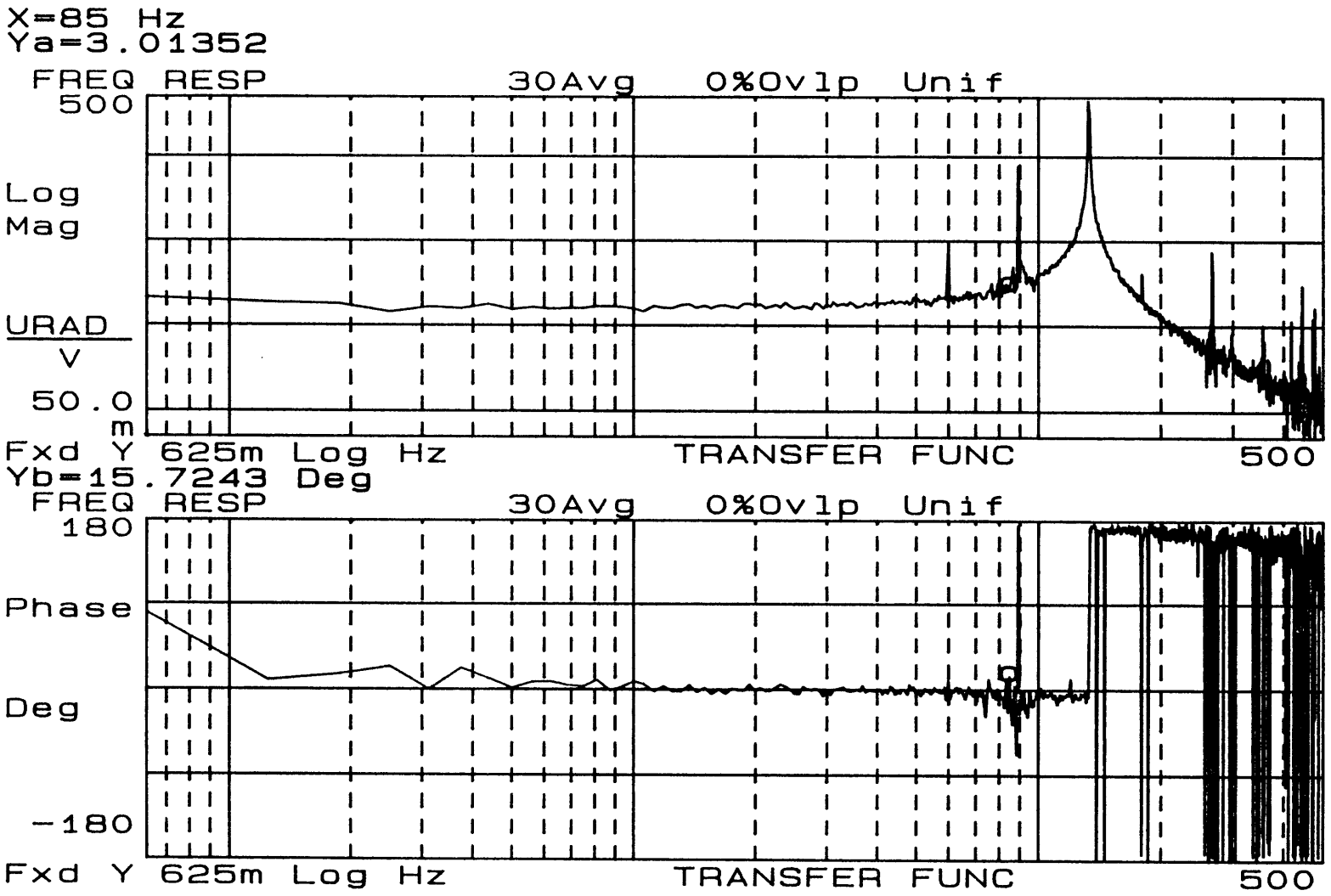

Figure 2.1-6. Measured transfer function of $\theta_X(j\omega)/M_X(j\omega)$. ORG evacuated.

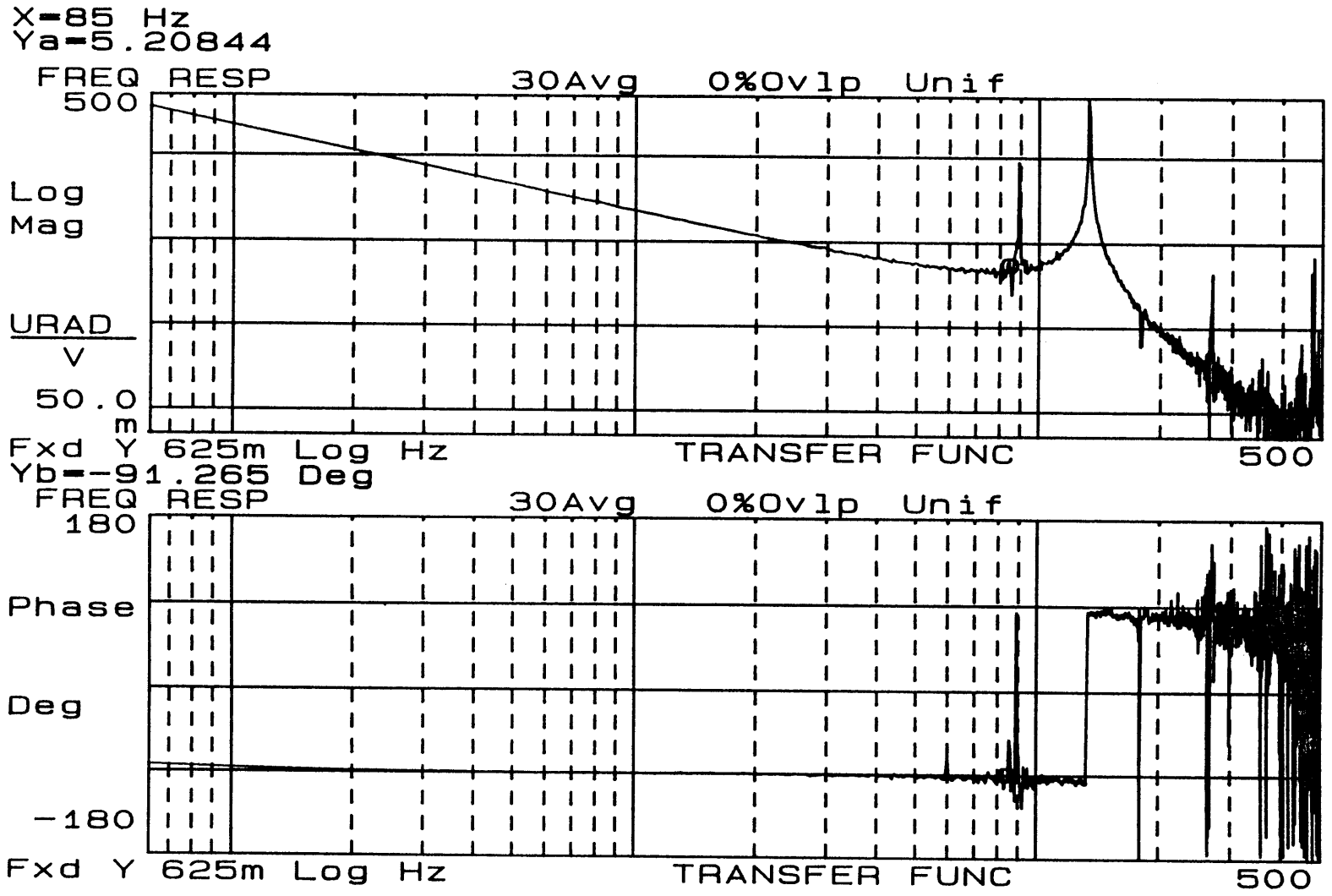

Figure 2.1-7. Measured transfer function of $\theta y(j\omega)/M_X(j\omega)$. ORG evacuated.

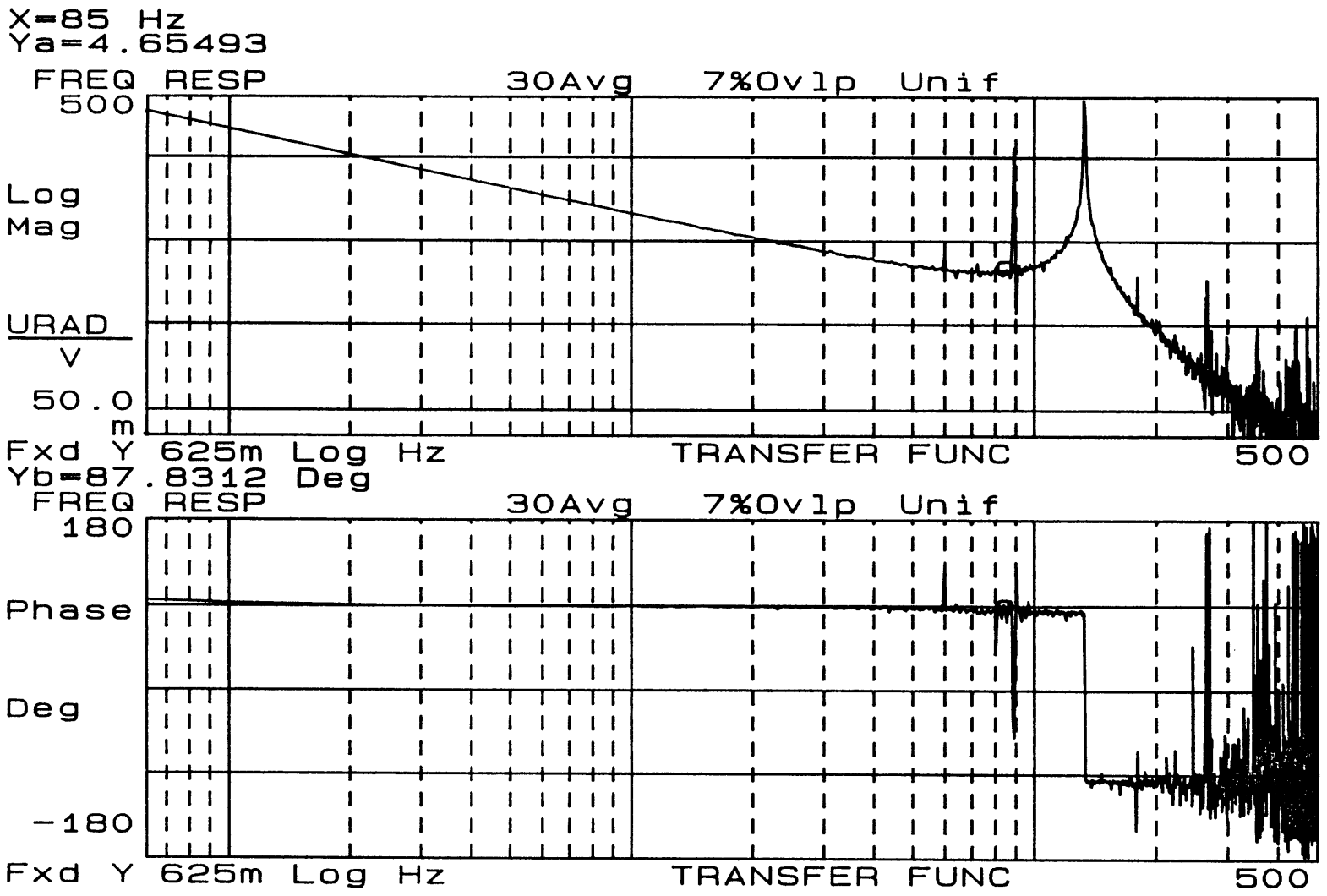

Figure 2.1-8. Measured transfer function of $\theta_X(j\omega)/My(j\omega)$. ORG evacuated.

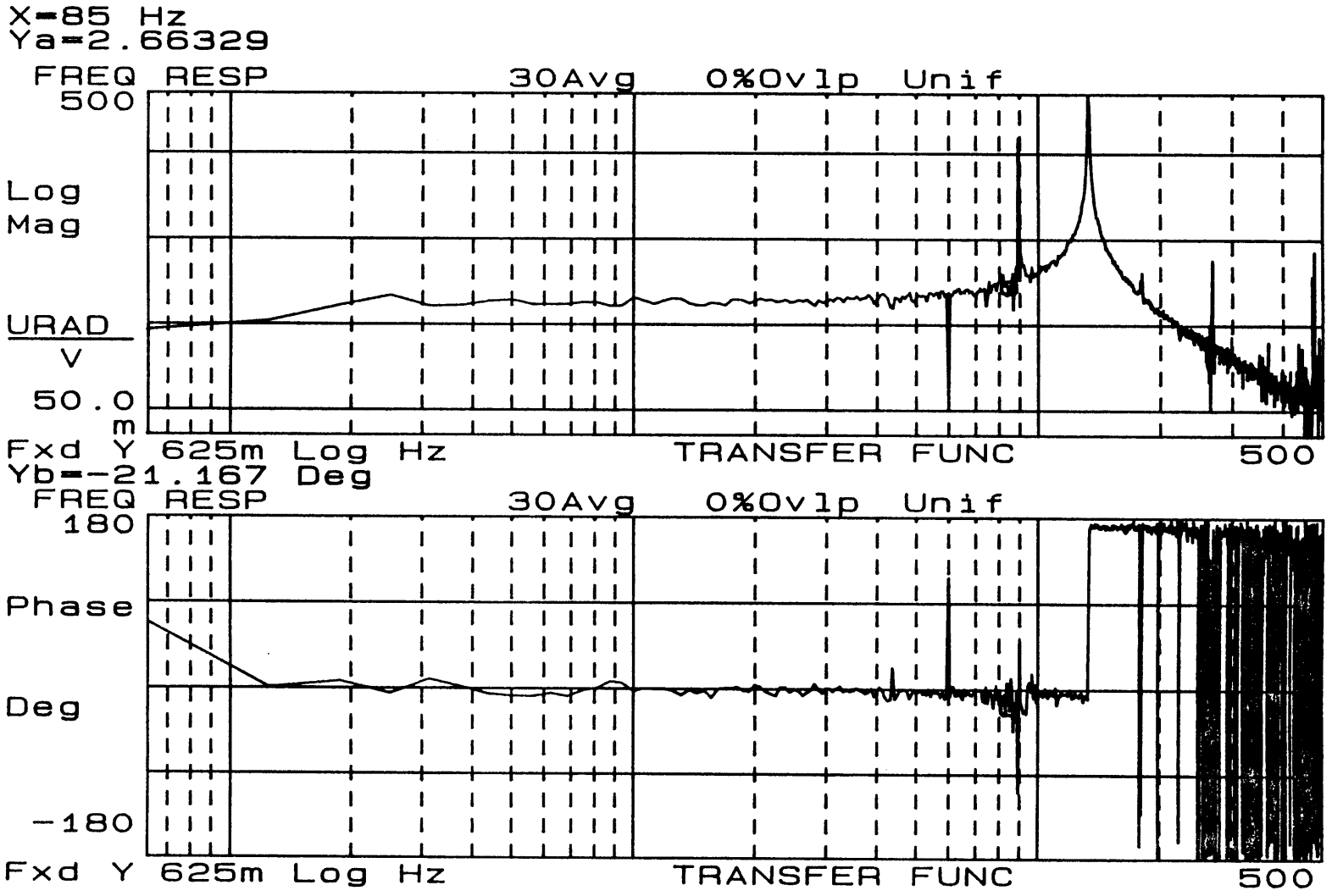

Figure 2.1-9. Measured transfer function of $\theta y(j\omega)/My(j\omega)$. ORG evacuated.

2.2 Optics

This section describes the optics of the ORG.

2.2.1 ORG Light Source

The purpose of the ORG is to serve as a pseudo-star. This means the ORG must produce light whose source doesn't move in inertial space. In reality, the ORG can only produce a light beam that doesn't move in *angle* in inertial space. In other words, the ORG light beam may translate but always points in the same direction.

2.2.1.1 Pinhole Mechanization

Ideally the light source must be placed on the rotor. But there is no simple way to supply power to something on the rotor. To solve this problem, a pinhole was placed at the back of the rotor with a collimating lens at the front of the rotor. Light is shone on the pinhole by an external source. This light is diffracted by the pinhole and then collimated into a beam by the lens. See fig. 2.2-1.

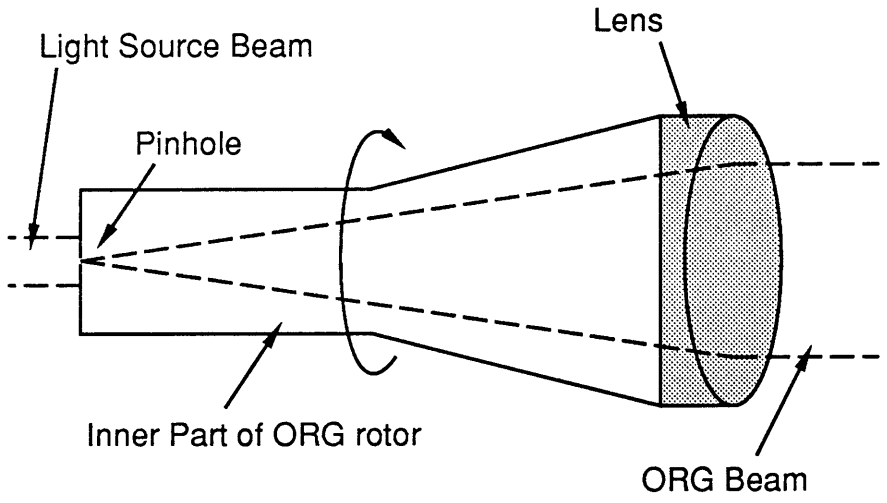

Figure 2.2-1. ORG pinhole and lens.

Before this discussion can precede further, the basic principles of diffraction must be explained.

Suppose a plane wave is incident on an opaque surface with a narrow slit in it. The Huygens-Fresnel Principle states that one can pretend each point in the slit is a spherical light source. The resulting diffraction pattern is simply the superposition of the light generated by all these light sources (see ref. 3).

Destructive interference will occur every time two waves are pointed in the same direction and are $\lambda/2$ out of phase. By looking at fig. 2.2-2, one can see that the smallest angle at which destructive interference goes on between all the point sources is

$$\theta = \pm\sin^{-1}(\lambda/a), \qquad (2\text{-}13)$$

where a is the width of the slit (see ref. 3).

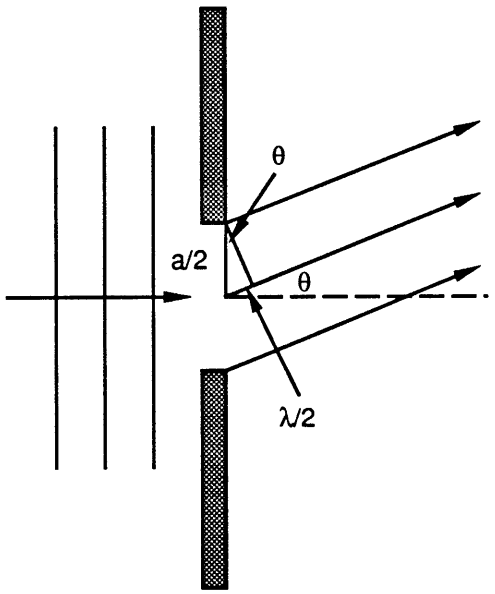

Figure 2.2-2. Diffraction through a slit.

Now suppose the plane wave hits the slit at an angle ø. One can see from fig. 2.2-3 that the smallest angle at which destructive interference goes on between all the point sources is

$$\theta = \text{ø} \pm \sin^{-1}(\lambda/a), \qquad (2\text{-}14)$$

provided ø and θ are small.

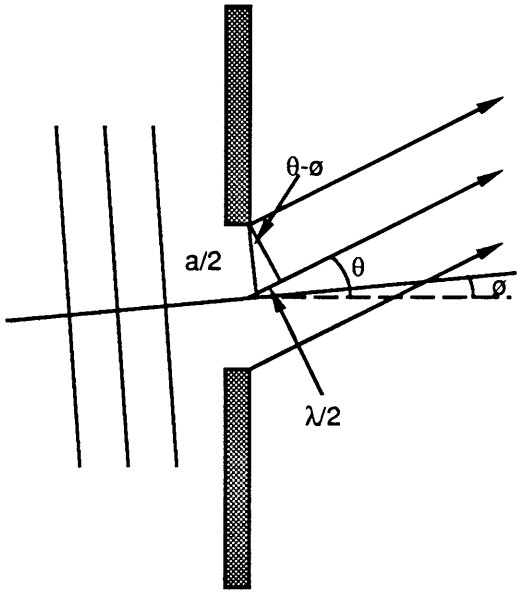

Figure 2.2-3. Diffraction through a slit when the incident light is at an angle.

But the pinhole is a circle and not a slit. To get the diffraction pattern from a circle, all the point sources in the circle must be superimposed using an integral. The integration is very lengthy, so just the result will be given.

As given in ref. 3, the angular position of the first null in the circular diffraction pattern is

$$\theta = \pm\sin^{-1}(1.22\lambda/a) \qquad (2\text{-}15)$$

where a is the diameter of the circle. Let d be the distance between the pinhole and the lens. Thus the distance from the center of the collimated ORG beam to the first dark ring is

$$r = d\tan[\sin^{-1}(1.22\lambda/a)] \approx 1.22d\lambda/a. \qquad (2\text{-}16)$$

Since most of the light is contained inside of the first dark ring, let r be the radius of the ORG beam.

For the ORG,

$d = 50 \times 10^{-3}$ m
$a = 8 \times 10^{-6}$ m
$\lambda = 680 \times 10^{-9}$ m

Thus, the first diffraction ring should occur at

$\theta = \pm 6.0°$
$r = 5.2$ mm.

Fig. 2.2-4 shows the dimensions of the diffraction pattern in the actual ORG beam. Note the theoretical value of r is little larger than what was measured but nevertheless fairly close.

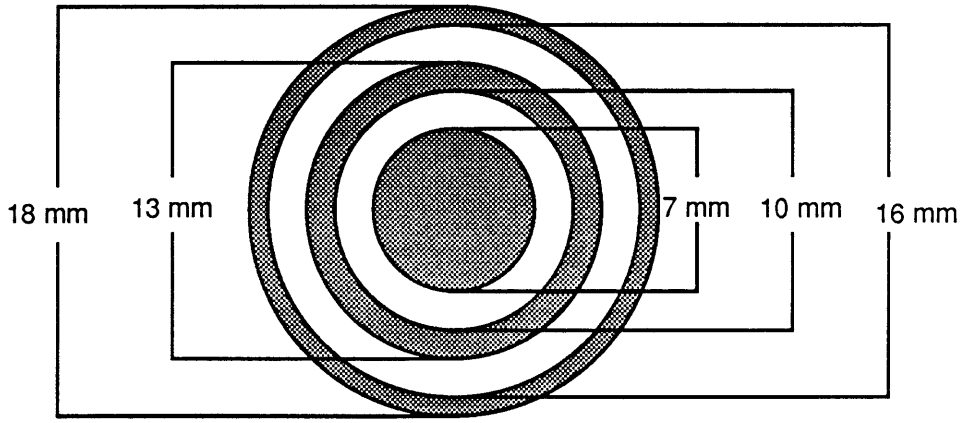

Figure 2.2-4. Measured dimensions of diffraction pattern in the ORG beam. The grey areas are where the light is.

If light enters a slit at an angle ø, the diffraction pattern is rotated by ø as shown in equation 2-16. Similarly, if light enters the pinhole at an angle ø, the diffraction pattern should also be rotated by ø. This means if the light source-to-rotor angle changes, the

diffraction pattern will move. But since the pinhole is placed in the focal plane of the collimating lens, the angle of the collimated ORG beam will remain unchanged. The beam will translate, but it will always point in the same direction. This is shown in fig. 2.2-5.

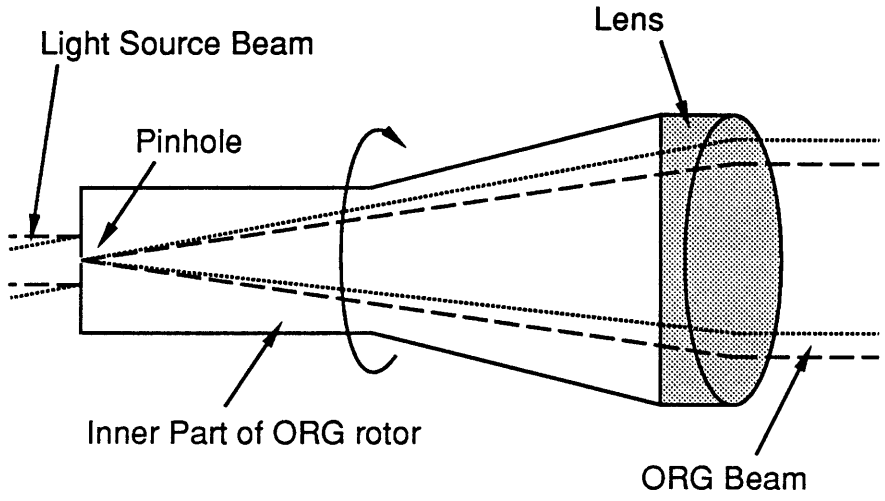

Figure 2.2-5. Effect on ORG beam of light source movement.

When the ORG was built by Draper Laboratory, the center of the collimating lens could not be placed exactly on the axis of rotation. If the pinhole is placed exactly on the axis of rotation, but the lens is off-center, the beam will have an angular wobble and will trace out a cone. See. fig. 2.2-6.

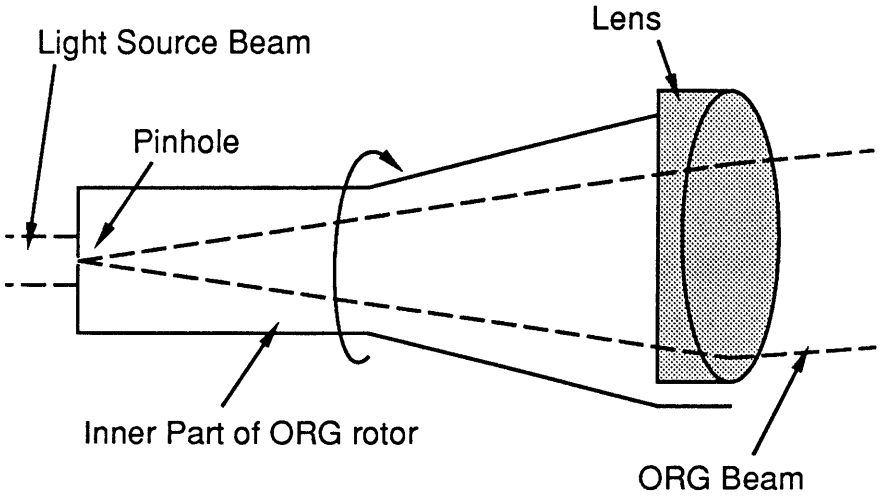

Figure 2.2-6. Lens center off axis of rotation, pinhole on axis of rotation.

Note: it doesn't matter if the lens is tilted or not as long as the pinhole is in the focal plane of the lens (this is because light passes through the center of a lens undeflected, and all other light which originates from the same point on the focal plane will leave the lens in the same direction). See fig. 2.2-7.

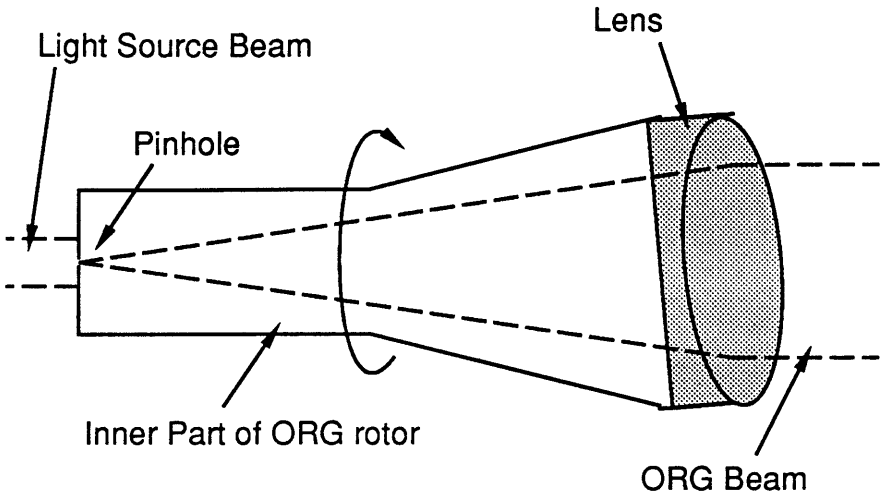

Figure 2.2-7. Tilted lens.

To reduce the angular wobble, the pinhole was moved off the axis of rotation by Draper Laboratory. The ideal location for the pinhole is shown in fig 2.2-8.

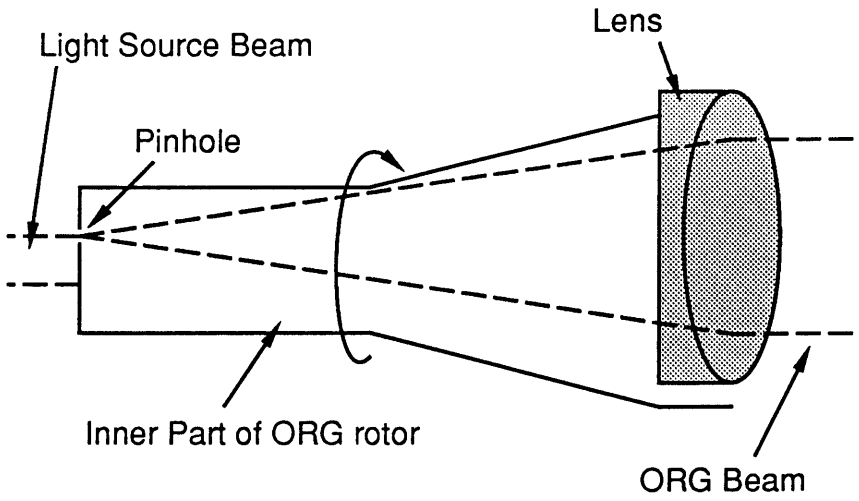

Figure 2.2-8. Lens center off axis of rotation, pinhole moved to eliminate angular wobble.

Perfect adjustment of the pinhole will cause the ORG beam to translate but always point in the same direction.

In the current ORG, it appears that both the lens and the pinhole are off-center, *and* the pinhole is not lined up with center of the lens. This means the ORG has translational and angular wobble.

2.2.1.2 Light Source Selection

The author had to find a suitable light source. Finding a suitable light source proved to be much more difficult than was anticipated.

The light source had to meet the following requirements:

1. Because the optical detector was a silicon detector, the light had to have wavelengths in the red to near infrared range (670 to 1000 nm) (preferably visible since visible light is much easier and safer to work with).
2. The light source spot on the pinhole had to be relatively large due to movement of the pinhole.

3. The intensity distribution across the light source spot on the pinhole had to be relatively uniform and rotationally symmetric.
4. The source had to be intense enough to have enough left over after passing through the pinhole (light source power > 3mW).
5. The light source intensity and spectrum had to be constant in time.

Several types of light sources were tried by the author. The first was a Sharp infrared laser diode. The diode was used with and without a focusing lens. The problem with the diode was the intensity distribution was very uneven across the beam and was not rotationally symmetric (it was more like a rectangle). This caused large intensity variations in the ORG beam as the rotor spun around.

A Toshiba visible laser diode (670 nm) was also tried. The output power was too low, though, and a reasonable ORG beam could not be created.

An incandescent light was tried. But since the light is generated by a filament, the intensity distribution of the focused light on the pinhole was not uniform. Also, the brightest sources found were driven by AC current, and thus the total intensity varied at 60 Hz.

Finally, several HeNe lasers were tried. At first, the laser beam was focused on the pinhole, but this made the light source spot on the pinhole so small, the pinhole would move in and out of the beam as the rotor turned. The best solution found was to shine the laser beam directly on the pinhole, using no extra optics. This gave about just the right size spot for the pinhole to stay in the beam during an entire rotor revolution. The spot size on the pinhole could be varied a little by exploiting the divergence of the laser beam and changing the laser-to-pinhole distance.

The main problem with the HeNe lasers was intensity variation with time. The output intensity of the laser would vary as much as 30%,

and the frequency of the variation would depend on how long the laser had been turned on, whether or not it was covered, etc.

Finally, a stabilized laser was found. It was a 4 mW Spectra Physics Model 117 that could maintain its intensity to ±1%. Unlike the other lasers, this laser's light was polarized. Polarization didn't seem to affect the behavior of the ORG beam, but it did affect the optical detector (see section 2.2.2.2)

Another problem with the HeNe lasers was increased noise due to back reflection. Very little of the laser light goes through the pinhole. The rest is reflected back. If the reflected light went back into the laser, the noise in the laser increased dramatically. See section 3.1.2 "Noise in Optical Signal Generator" to find out how much the noise changed.

2.2.2 Optical Detector

The optical detector that measured the ORG beam had to have the following characteristics:

1. It had to have an output proportional to angular movement of the ORG beam about the x- and y-axes.
2. It had to be insensitive to beam translation.
3. It had to be able to maintain a high signal-to-noise ratio despite the small power (about 10 μW) of the ORG beam.
4. It had to be able to measure angular movement on the order of 10^{-8} rad.

2.2.2.1 Photopot and Quad-Cell

The first optical detectors the author tried were the photopot and quad-cell, which were obtained from Draper Laboratory. The photopot is basically a square piece of semiconductor with a wire attached to each side. The quad-cell is four separate pieces of semi-conductor placed together. Both detectors can measure the

position of small spot of light shined on their surfaces. A telescope was placed between these detectors and the ORG (see fig. 2.2-9). A telescope was used because it ignores beam translation, magnifies angle, and can focus the ORG beam on the detector.

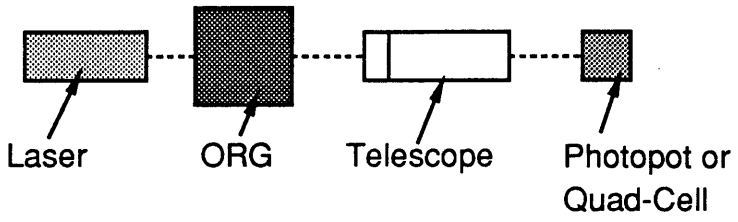

Figure 2.2-9. Photopot/quad-cell setup.

But neither the photopot nor the quad-cell worked well. Their responses were non-linear, and their signal-to-noise ratios were higher than the ORG instrument noise.

2.2.2.2 DYNAC

The DYNAC, or Dynamic Autocollimator, built by Draper Laboratory (see ref. 10), turned out to be the best optical detector. The DYNAC consists of a lens that focuses the incoming beam onto a bi-lens. A bi-lens is two lenses joined together. The bi-lens divides up the light between two photocells. As the angle of the input beam is changed, the spot the on the bi-lens is moved, changing the percentages of the light going to each photocell. Thus, if one labels the output of one photocell A and the other B, the angle of the incoming beam is proportional to A-B. See fig. 2.2-10.

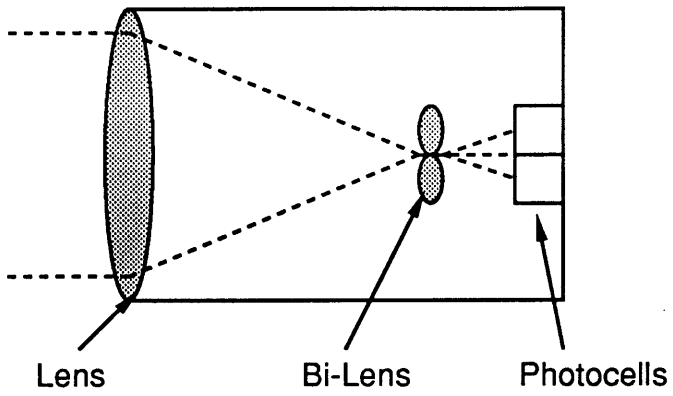

Figure 2.2-10. Simplified drawing of single-axis DYNAC.

Two types of DYNAC were tried--the single-axis DYNAC and the dual-axis DYNAC. The dual-axis DYNAC is like the single-axis DYNAC except it has a quad-lens instead of a bi-lens. The quad-lens allows the dual-axis DYNAC to detect angular movement in two axes simultaneously.

But regrettably, reasonable results could not be obtained with the dual-axis DYNAC. It is believed this was because the ORG beam diameter was too small for the dual-axis DYNAC. For any DYNAC, the larger the incoming beam diameter, the better. This is because the larger the spot, the more evenly divided the light on the photocells, and thus the larger the linear range of the measurement. This is because the ORG beam is a circle and not a square. In fact, the beam is not even a circle; instead it is a circular diffraction pattern cut off by the rotor opening. The non-linearity can be seen more easily in the extreme case: if the ORG beam diameter were infinitely small, the DYNAC would only be able to measure what side of null the beam was on.

So to measure two axes simultaneously, two single-axis DYNAC's were used. A beam splitter sent the ORG beam to both DYNAC's; one DYNAC was set to measure elevation while the other was set to measure azimuth (see fig 2.2-11).

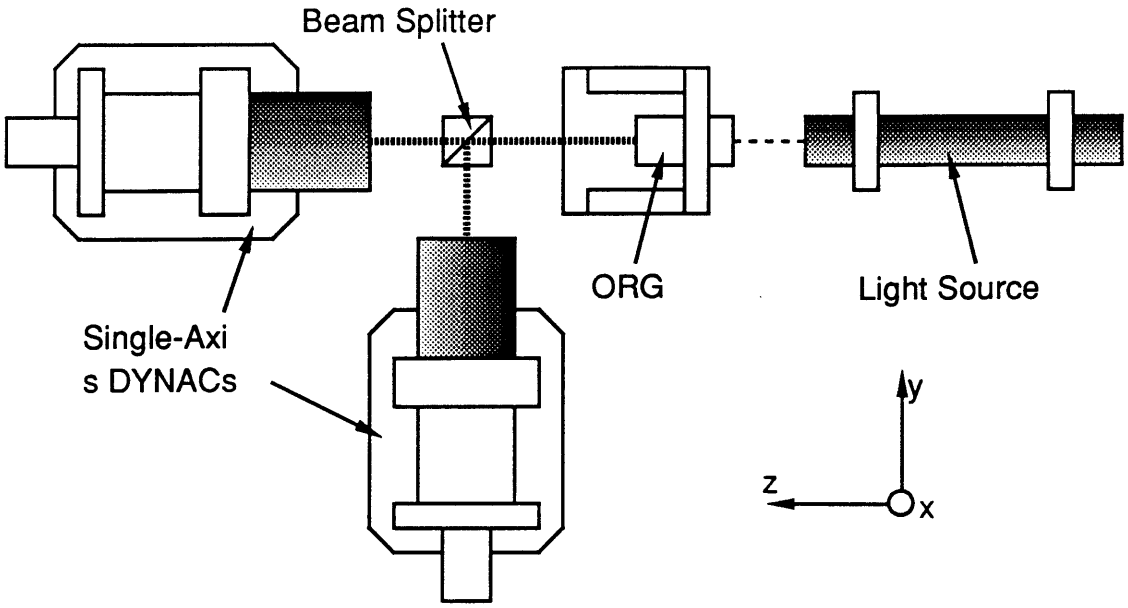

Figure 2.2-11. Measurement of both x- and y-axes of OSG simultaneously. One DYNAC was oriented to measure azimuth or x, and the other was oriented to measure elevation or y.

One of the problems with the DYNAC was reading polarized light. The DYNAC has an internal beam splitter, which can be used to send its own internal light source out and detect the movement of a mirror. The beam splitter acted like a polaroid, and the laser used as the ORG light source had to be rotated accordingly.

Another problem with the DYNAC was intensity changes in the ORG beam. As the pinhole moves around in the light source beam, the intensity of the ORG beam changes. If the angle is measured just by taking the difference of the intensities falling on the photocells in the DYNAC, the scale factor will change when the total intensity changes. It was found if the DYNAC measurement was normalized by the intensity of the ORG beam, the measurements became much more consistent. A circuit was built by the author that, instead of producing the regular DYNAC output A-B, produced (A-B)/(A+B). The improvement can be seen from the following test the author performed:

The laser beam was aligned on the pinhole to minimize intensity variation as much as possible. Then the scale factor of the DYNAC was measured. This was done by closing the torque-rebalance loop on the ORG rotor (so the rotor would move with the case), dithering the platform the ORG was on, and comparing the DYNAC output to a reference that measured the platform's motion. The scale factors were

With Intensity Normalization	Without Intensity Normalization
44.2 mV/μrad	37.8 mV/μrad.

Then the laser was aligned so the intensity varied about 30% during each rotor revolution. The new scale factors were

With Intensity Normalization	Without Intensity Normalization
43.8 mV/μrad	26.7 mV/μrad.

As one can see, the measurement with intensity normalization was more consistent.

2.3 Summary of Basic Principles of ORG

The basic model of the ORG is a free spinning wheel. A more accurate model that takes into account rotor-to-case coupling includes torques on the wheel by the shaft and gas inside the ORG. These torques cause the rotor to follow the case at low frequencies.

Having a light source on the rotor is simulated by having a pinhole at the back of the rotor in the focal plane of a lens at the front of the rotor. The best source to illuminate the pinhole was found to be a stabilized HeNe laser shone directly on the pinhole. The best detector to measure the angular movement of the beam was found to be the Draper-built single-axis DYNAC.

3 ORG Noise Characterization and Compensation

The ORG outputs (the ORG beam and the electrical pick-offs that measure rotor-to-case angle) have both wide-band and discrete-frequency noise. The first part of this section quantifies the noise and draws conclusions as to the sources of the noise. The rest of the section describes a device called the Eliminator, created by the author, that reduces the discrete-frequency noise.

3.1 ORG Noise Characterization

The ORG noise was measured by the author by observing the ORG outputs while the ORG was on a quiet platform. The quiet platform was a rectangular table with a thick granite slab top and four metal legs. The table sat directly on a concrete floor on the ground floor of Draper Laboratory. The platform did move a little, but primarily the ORG outputs were purely noise.

3.1.1 Noise in Electronic Signal Generator (ESG)

The electronic signal generator (ESG) is the electrical pick-offs inside the ORG that give the case-to-rotor angle about the x- and y-axes.

Fig. 3.1-1 shows a power spectral density (PSD) plot of the x ESG while the ORG was on a quiet platform. The top plot is the PSD, and the bottom is the integral of the PSD. The units of the top plot are rms $\mu rad^2/Hz$, and the units of the bottom plot are rms μrad^2. If one integrates the top plot over a certain frequency range, one will have the total power contained in that frequency range. This means the bottom plot is a plot of the power contained from 0.625 Hz to f vs. f.

To show that this PSD is mostly ORG noise, and not real motion, the PSD's in fig. 3.1-2 show table motion as measured by a Systron-Donner Angular Displacement Sensor (ADS) together with the ESG output. Note: an ADS consists of a float inside a fluid. When the ADS case is moved, the float resists the motion, and signal generators

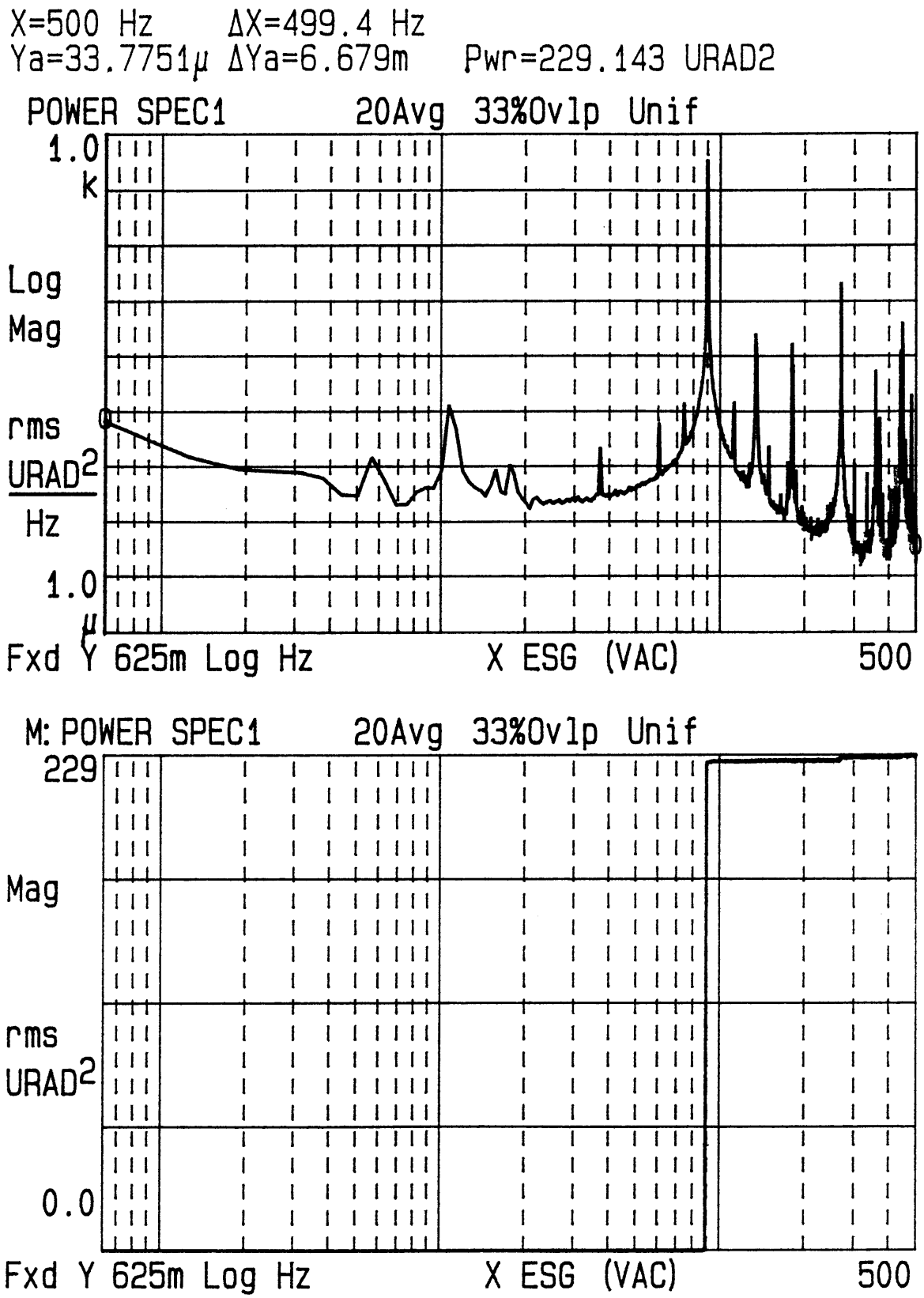

Figure 3.1-1. PSD of x ESG. ORG evacuated, low torque-rebalance loop.

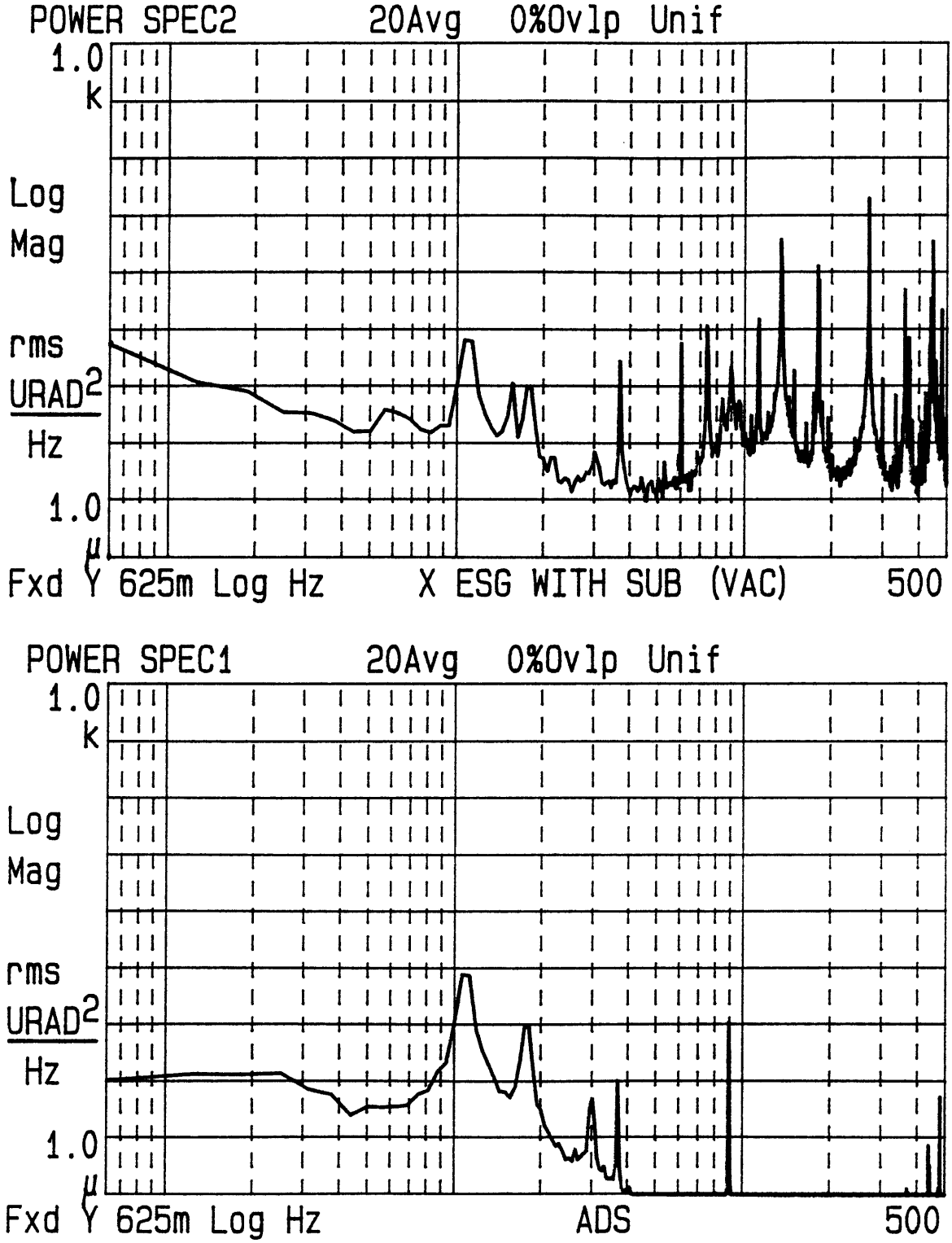

Figure 3.1-2. PSD's of x ESG and ADS. ORG evacuated, low torque-rebalance loop, Subtraction Eliminator on.

measure the movement of the float. A torque-rebalance holds the float at null inside the case for frequencies below 2 Hz, and thus the ADS just measures angular movement above 2 Hz. The ADS noise is extremely small.

Nearly all of the ESG noise is contained at the rotor spin-speed (89.4 Hz). The reason the spike at the spin-speed widens out at the bottom is because the data was taken using a rectangular window, and subsequently the spin-frequency discrete "leaked" into the other frequencies. Since the total power from 0.625 Hz to 500 Hz is 229 rms μrad^2 in the measurement in fig 3.1-1, and almost all of that power is at the spin speed, the amplitude of the spin-speed sinusoid must be approximately $(2*229\ \mu rad^2)^{0.5} = 21.4\ \mu rad$.

After the spin-speed discrete, the next largest discrete-frequency noises are the spin-speed harmonics. Fig. 3.1-3 shows another PSD of the ESG, but on a linear frequency scale. The arrow points to the spin-frequency, and the "V"'s point to the harmonics. Note the second-largest discrete-frequency noise is the third harmonic, or three times the wheel speed.

Another large discrete-frequency noise is a the nutation frequency (133 Hz). This is the natural resonant frequency of the gyro and corresponds to a wheel "wobble". The peak is due to wide-band disturbance-torque noise.

The spin-frequency discrete and its harmonics don't seem to be caused by accelerations from the gyro motor. Fig. 3.1-4 shows the integrals of the ESG and OSG (OSG stands for optical signal generator and is discussed in the next section) PSD's with the motor on, and fig. 3.1-5 shows them with the motor off and the rotor slowing down. By looking at the step sizes, it appears the magnitude of the harmonics didn't change much when the motor was shut off.

The spin-frequency discrete is most likely due to the fact that the ESG null axis is not coincident with the spin-axis. In other words, if

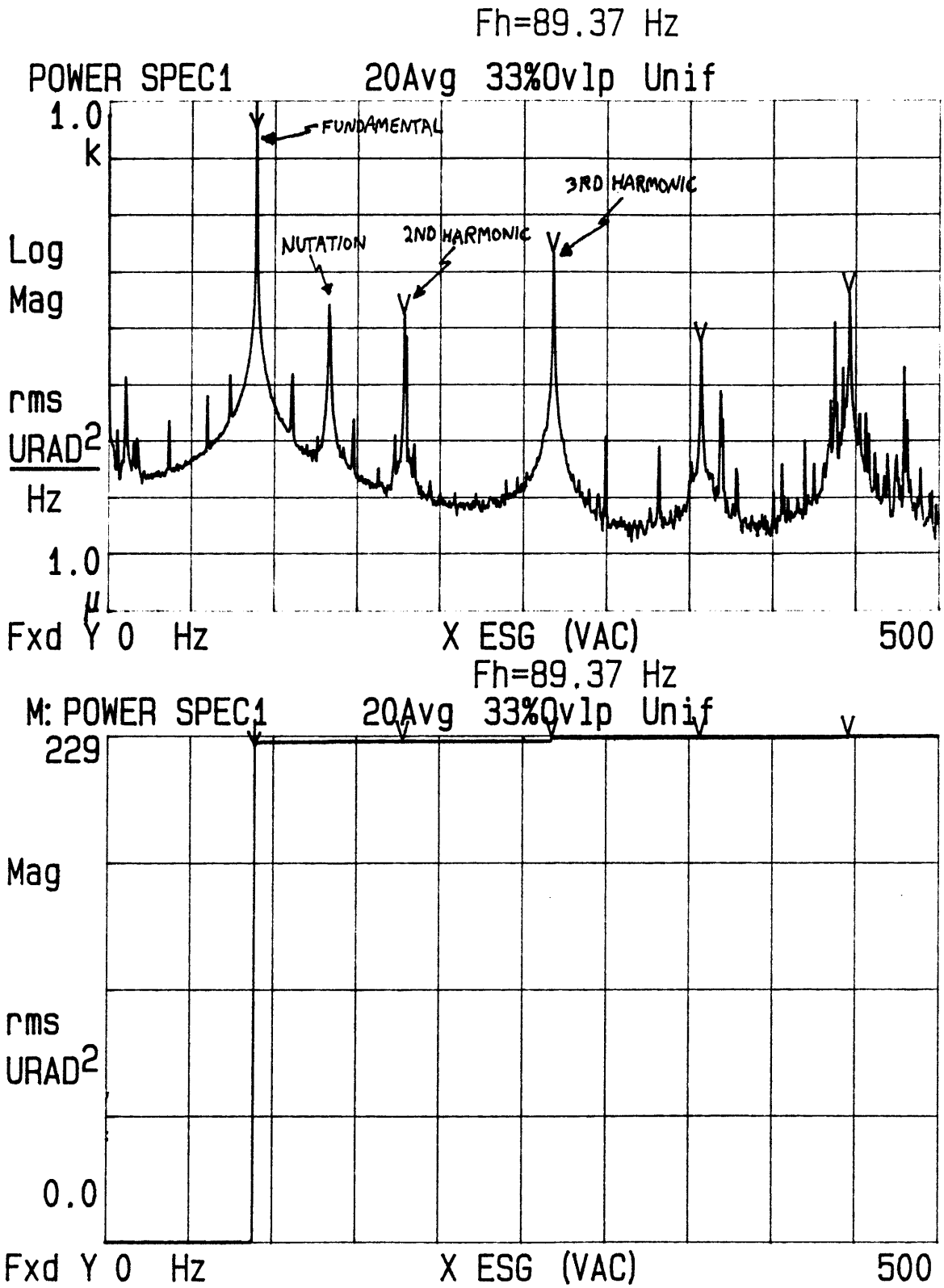

Figure 3.1-3. PSD of x ESG with linear frequency scale. ORG evacuated, low torque-rebalance loop.

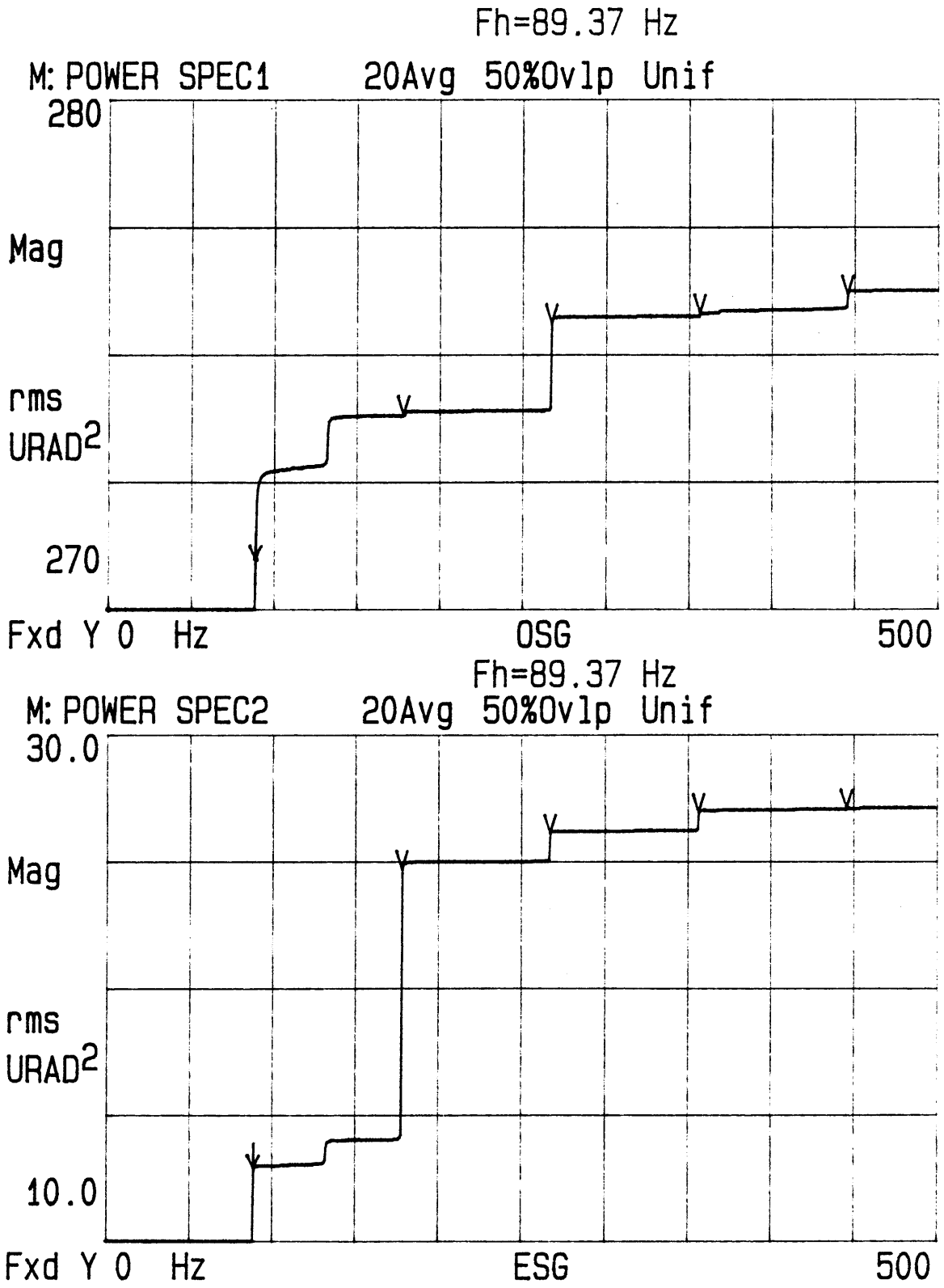

Figure 3.1-4. Integrals of ESG and OSG PSD's with the wheel motor on.

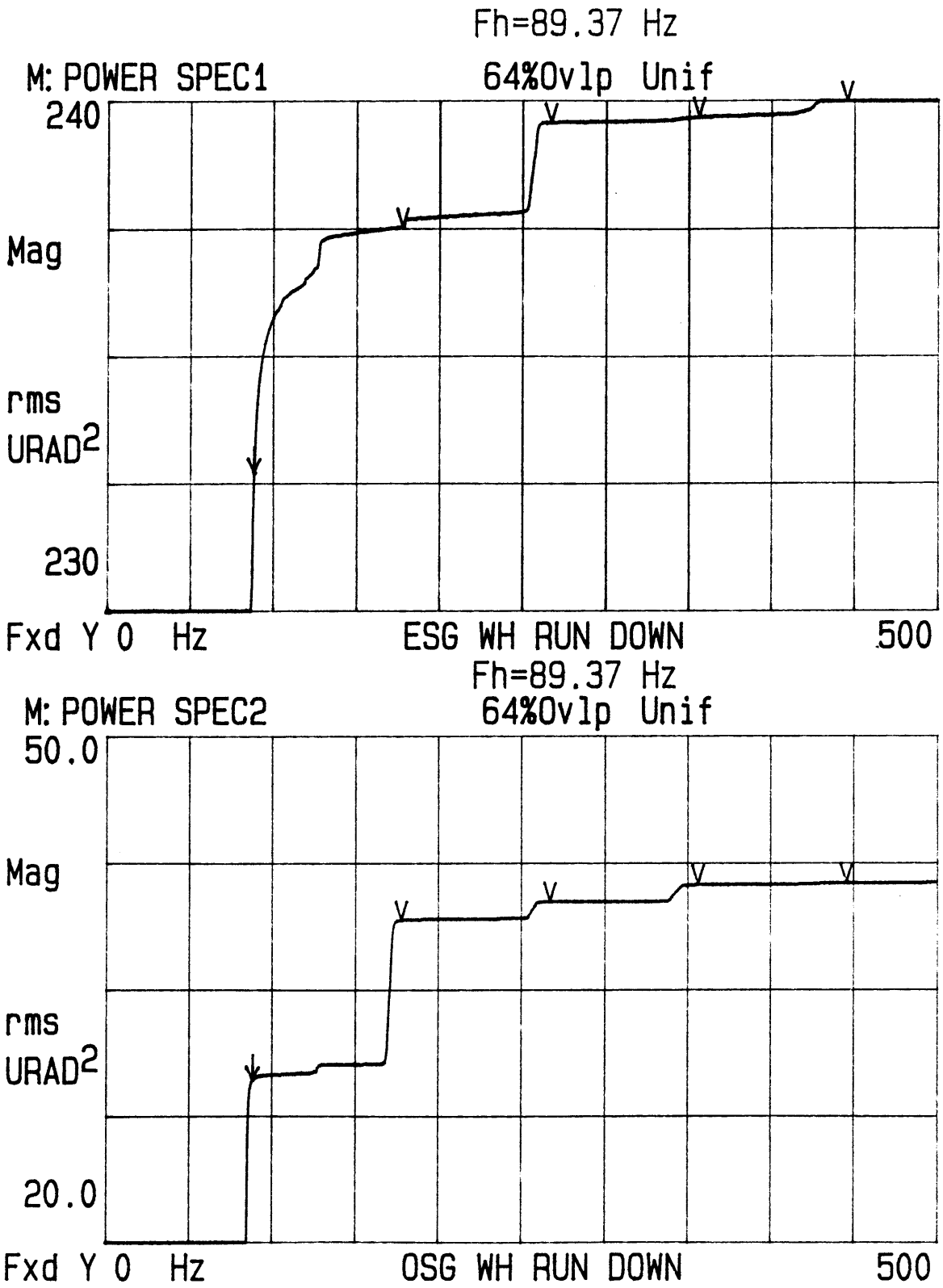

Figure 3.1-5. Integrals of ESG and OSG PSD's with the wheel motor off and wheel slowing down.

the rotor was spun so as to keep the x and y ESG signals at zero, the rotor would not be spinning about its center of gravity. This means the rotor is not perfectly symmetric about the rotor inertia z-axis. And if the rotor is not a perfect circle, harmonics will be generated. Thus the spin-frequency discrete and its harmonics are probably primarily due to asymmetries of the rotor.

In addition to the discrete-frequency noise, the ESG also has wide-band noise, called the noise floor. This noise floor appears to mainly be caused by three sources: the gas inside the ORG, the electronics, and the torque-rebalance loops.

Part of the noise floor is caused by gas inside the ORG. This is shown by comparing the noise floor levels of the PSD's in fig. 3.1-6. The ORG contained air at 1 atm in the top plot and a near vacuum (pressure: 6 μm of Hg) in the bottom plot. As one can see, the air adds a significant amount of wide-band noise. In fact the air appears to produce a white noise torque. For any linear system, if the input is white noise, then the power spectrum of the output will be the square of the linear system transfer function times the variance of the input. Ignoring the discrete-frequency noises, the shape of the PSD when the ORG is filled with air at 1 atm is similar to the shape of the ORG transfer functions $\theta(j\omega)/M(j\omega)$ in figs. 2.1-2 through 2.1-9.

The cause of the next noise floor after gas is removed appears to be electrical noise. The following ESG PSD (see fig 3.1-7) was taken with the rotor not spinning. The noise 30 Hz and below is platform movement, but above 30 Hz the noise is basically ORG noise, and when the wheel is stopped, this noise must be mostly electrical noise. The noise with the wheel off is at approximately the same level as with the wheel spinning in the 30 to 80 Hz region. Thus the noise floor, at least in the 30 to 80 Hz region, is most likely electrical noise.

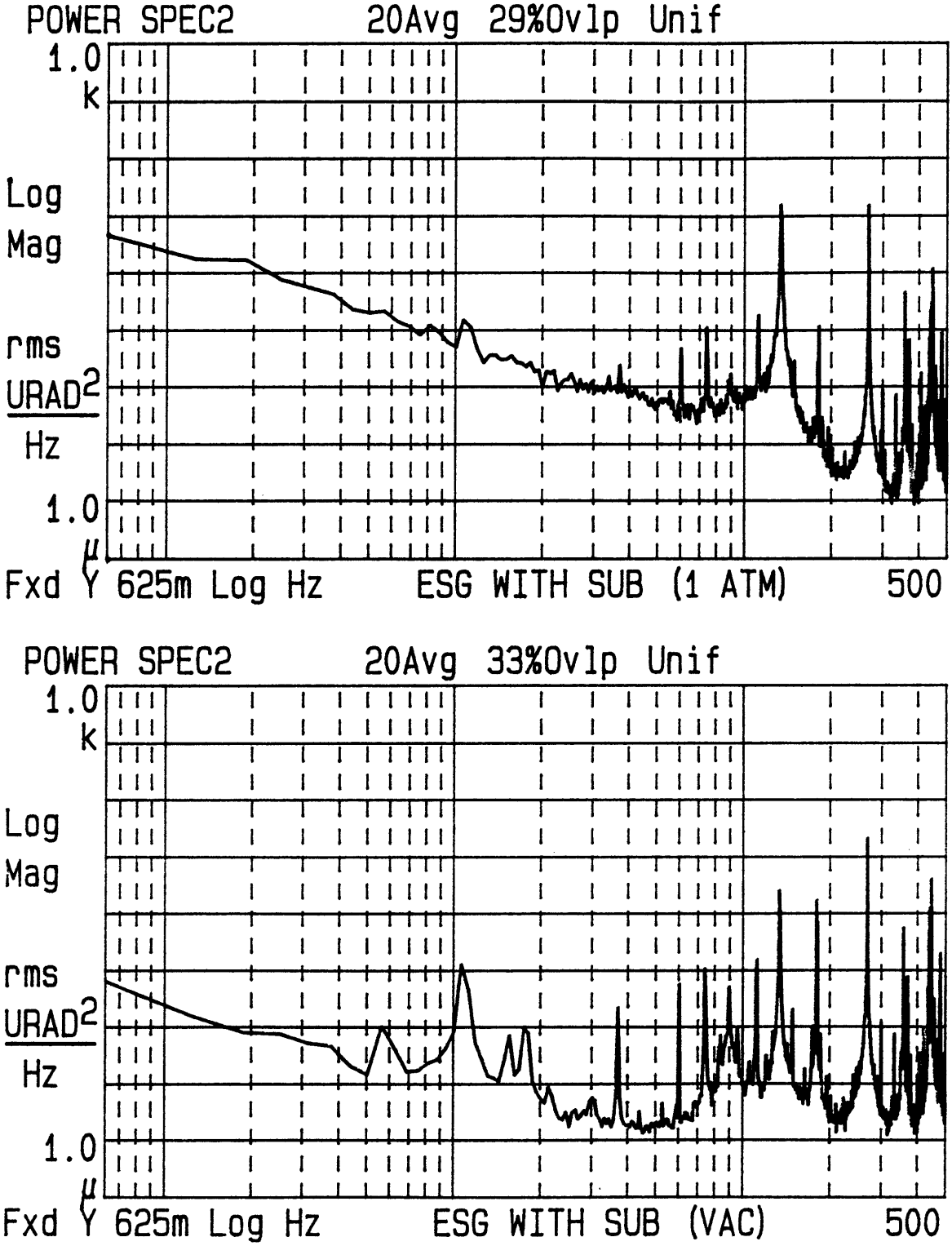

Figure 3.1-6. PSD's of x ESG with and without gas. Top plot is ORG filled with air at 1 atm. Bottom plot is ORG evacuated. Low torque-rebalance loop, Subtraction Eliminator on.

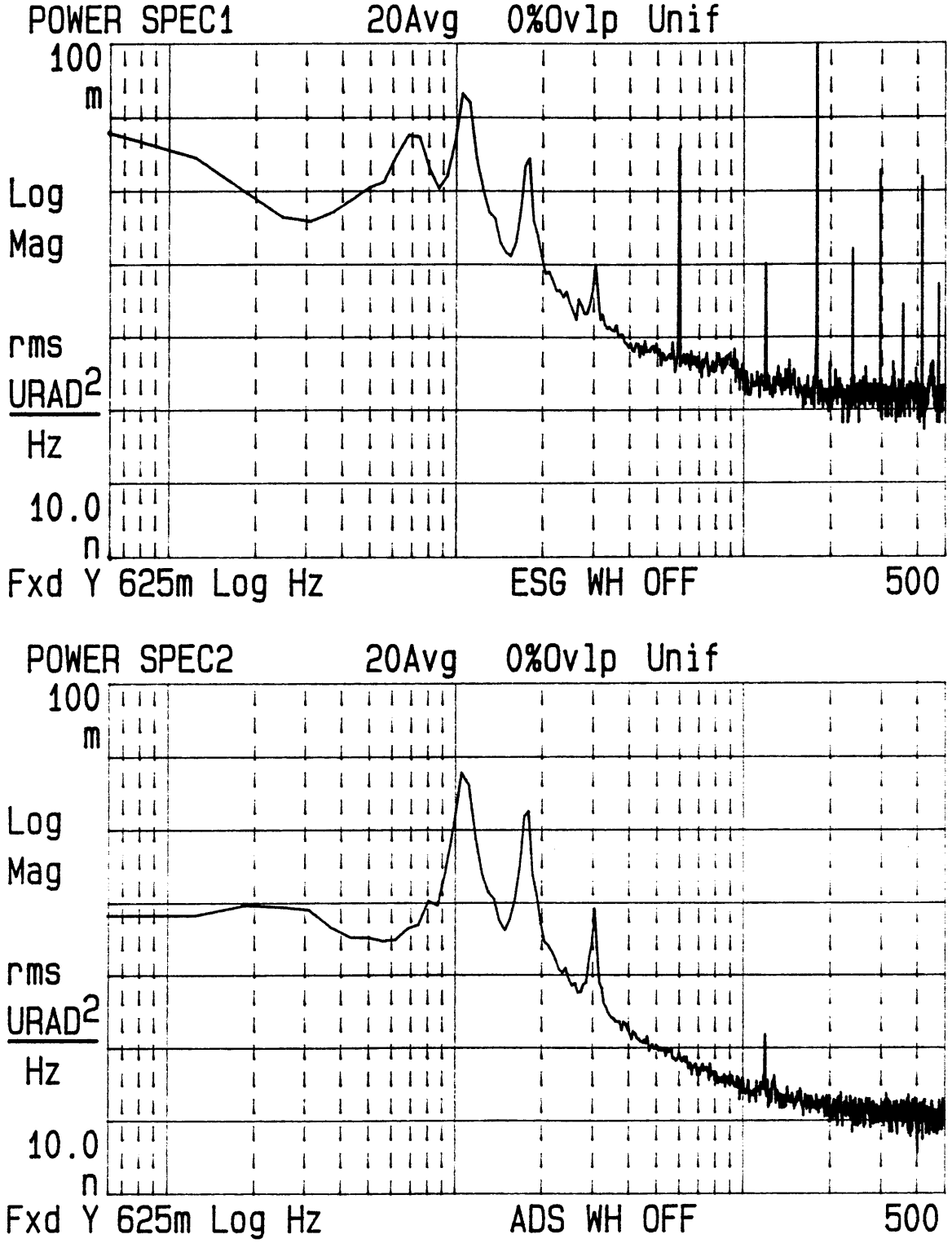

Figure 3.1-7. PSD of x ESG. Wheel off, low direct-axis torque-rebalance loop closed.

Another cause of wide-band noise is the torque-rebalance loops. The torque-rebalance loops lock the rotor to the case at low frequencies. When the torque-rebalance loops were closed, the noise in both the ESG and OSG increased, and the higher the torque-rebalance loop bandwidth, the higher the noise. The torque-rebalance loops added noise especially near the spin speed. That is why there is a small peak at the spin speed after the spin-frequency discrete has been compensated for. It is believed most of the noise is caused by a switched-capacitor notch filter in the torque-rebalance loop. The top PSD in fig. 3.1-8 shows the ESG with the torque-rebalance loops open, and the bottom with them closed. Note especially the drop in the resonant peak at the nutation frequency (133 Hz).

Thus the least noise in the ESG is obtained when the ORG has a near vacuum inside, the torque-rebalance loops are open, and the spin-frequency noise is removed by the eliminator (see fig. 3.1-9). Note that when the torque-rebalance loops were open, the rotor drifted off of null, and the ESG accrued a large D.C. offset. This D.C. offset hurt the Eliminator performance, and that is why the spin-frequency noise is still rather large in figs. 3.1-8 and 3.1-9.

3.1.2 Noise in Optical Signal Generator (OSG)

The optical signal generator (OSG) is basically the DYNAC that measures the ORG beam. Ideally, the OSG measures rotor-to-DYNAC motion.

Fig. 3.1-10 shows a PSD of the OSG and the corresponding integral. As with the ESG, it can be shown that these OSG measurements were measuring noise and not platform movement (at least above 10 Hz--see fig. 3.1-11).

Like the ESG, nearly all the noise is contained at the spin-frequency. Since the total power from 0.625 Hz to 500 Hz for the measurement in fig. 3.1-10 is 92 rms μrad^2, and most of that power is contained

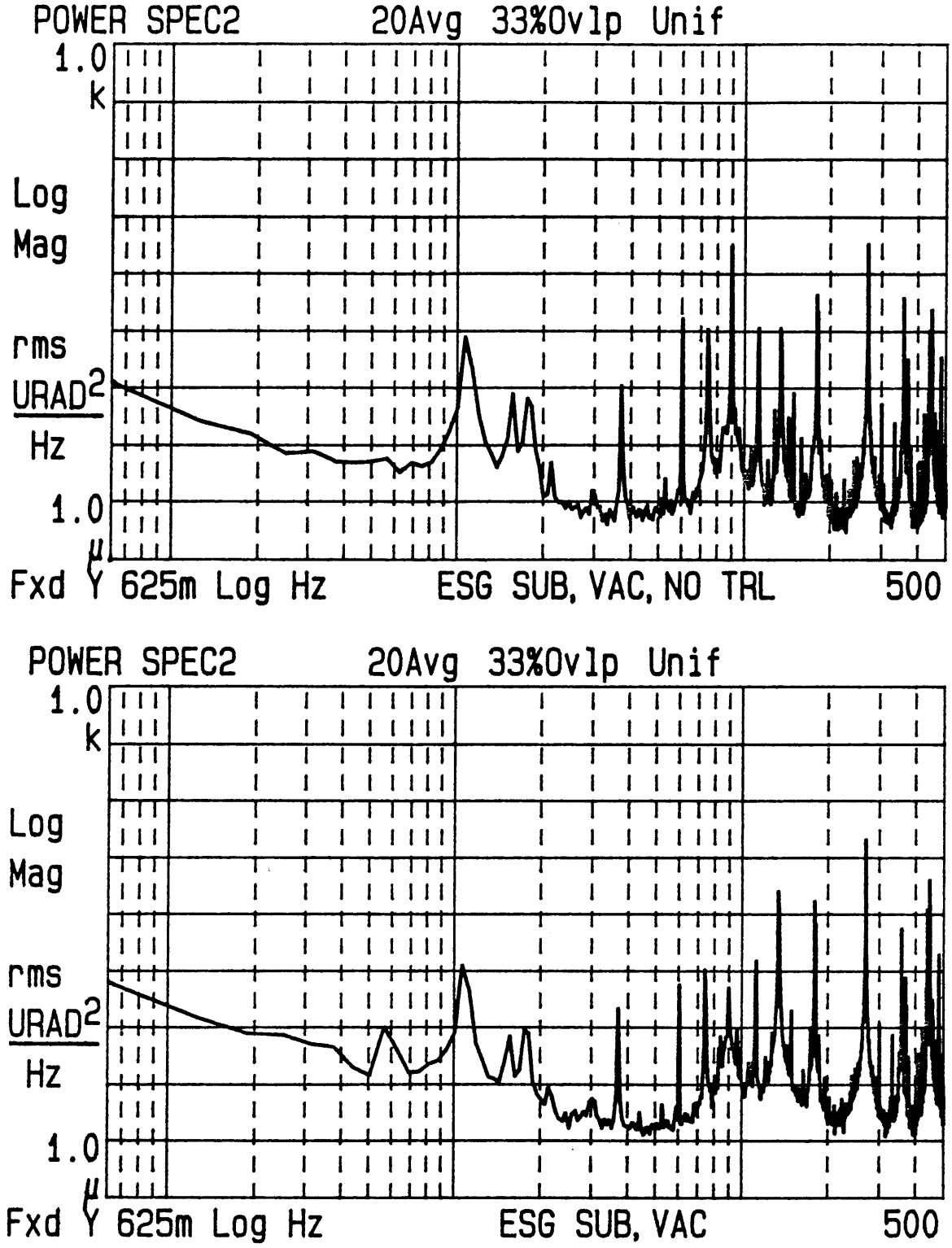

Figure 3.1-8. PSD's of x ESG with and without torque-rebalance loop. Top plot is ORG with torque-rebalance loops open. Bottom is with torque-rebalance loops closed. ORG evacuated, Subtraction Eliminator on.

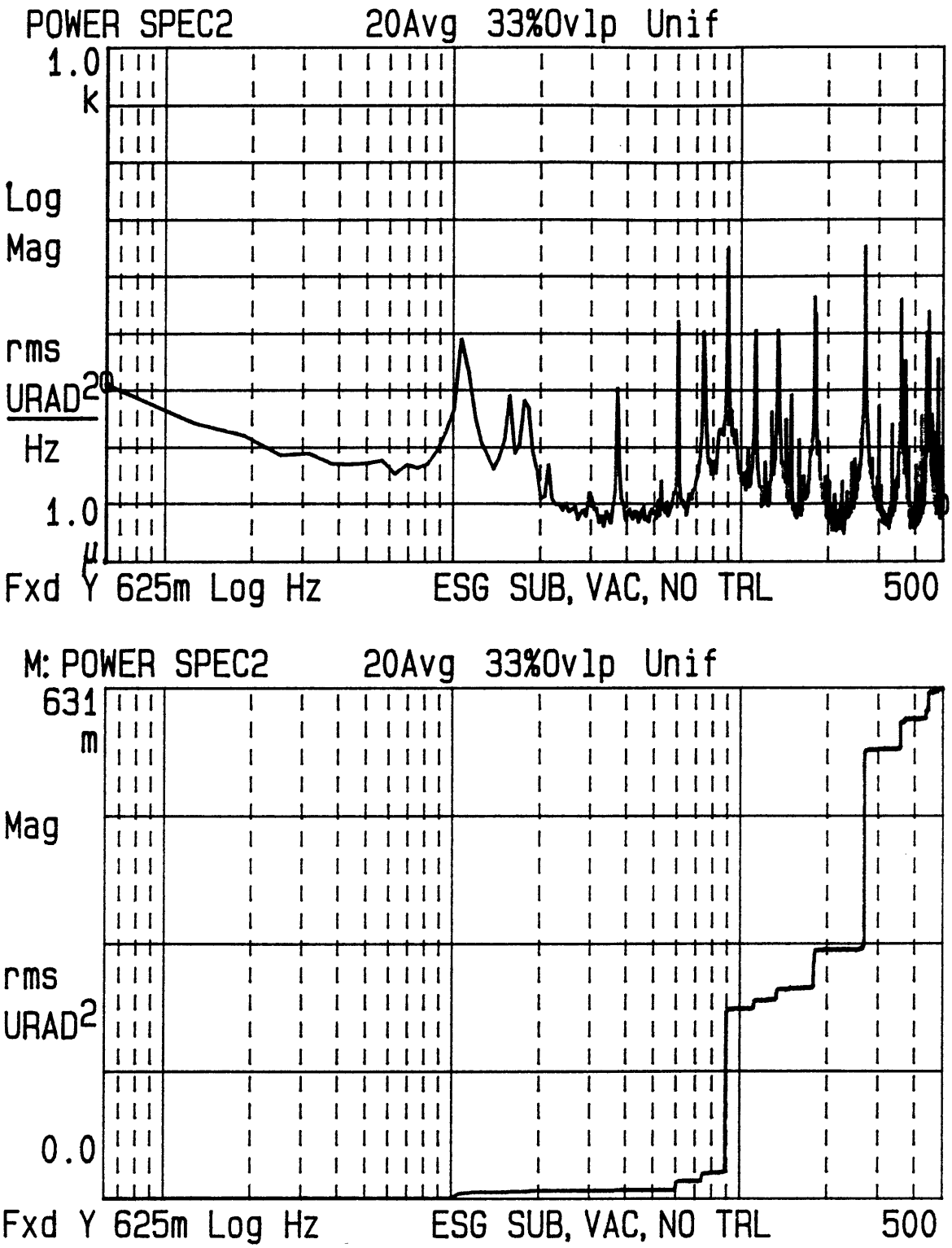

Figure 3.1-9. PSD of x ESG. ORG with near vacuum inside, torque-rebalance loops open, spin-frequency noise removed by Subtraction Eliminator.

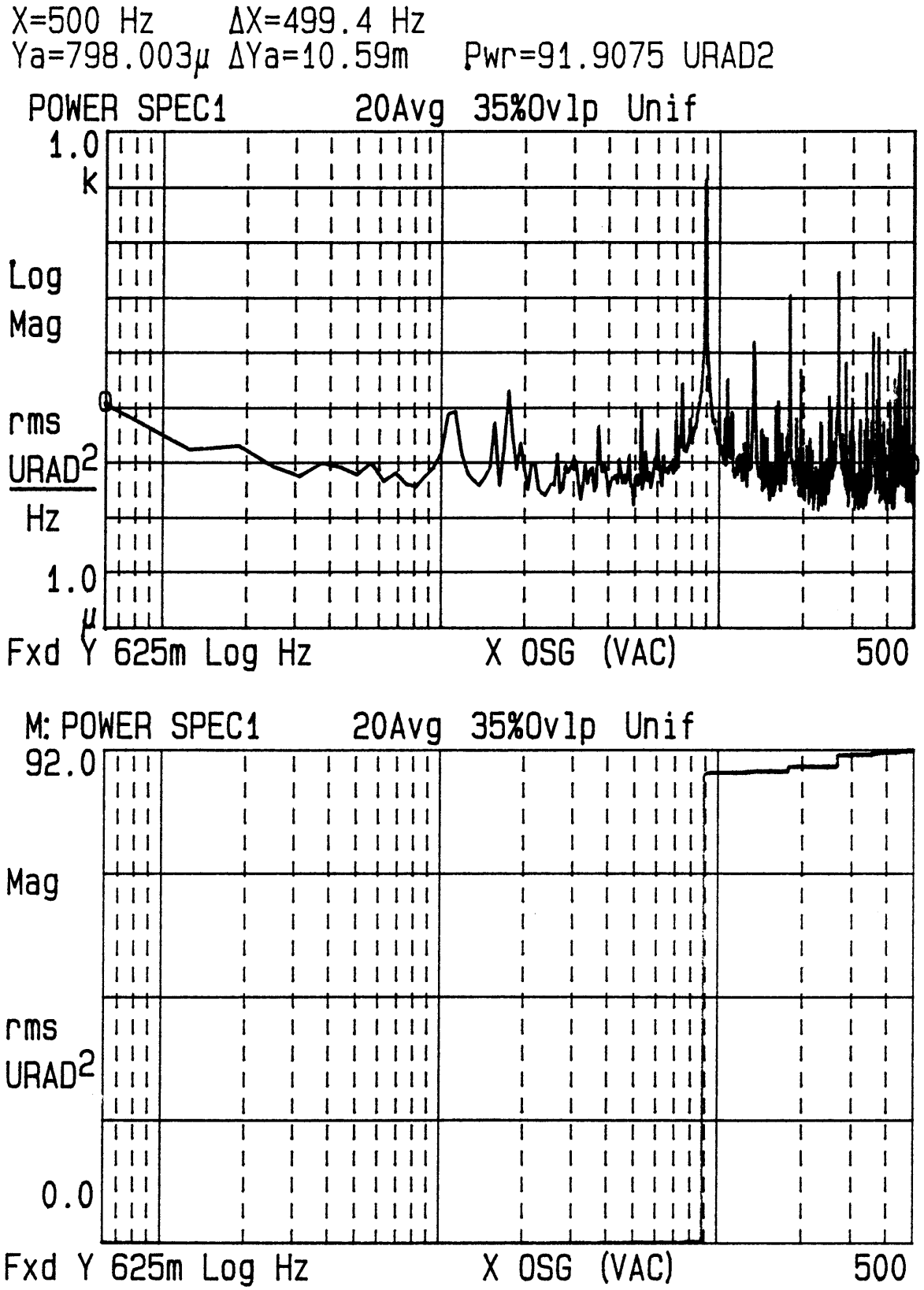

Figure 3.1-10. PSD of x OSG. ORG evacuated, low torque-rebalance loop.

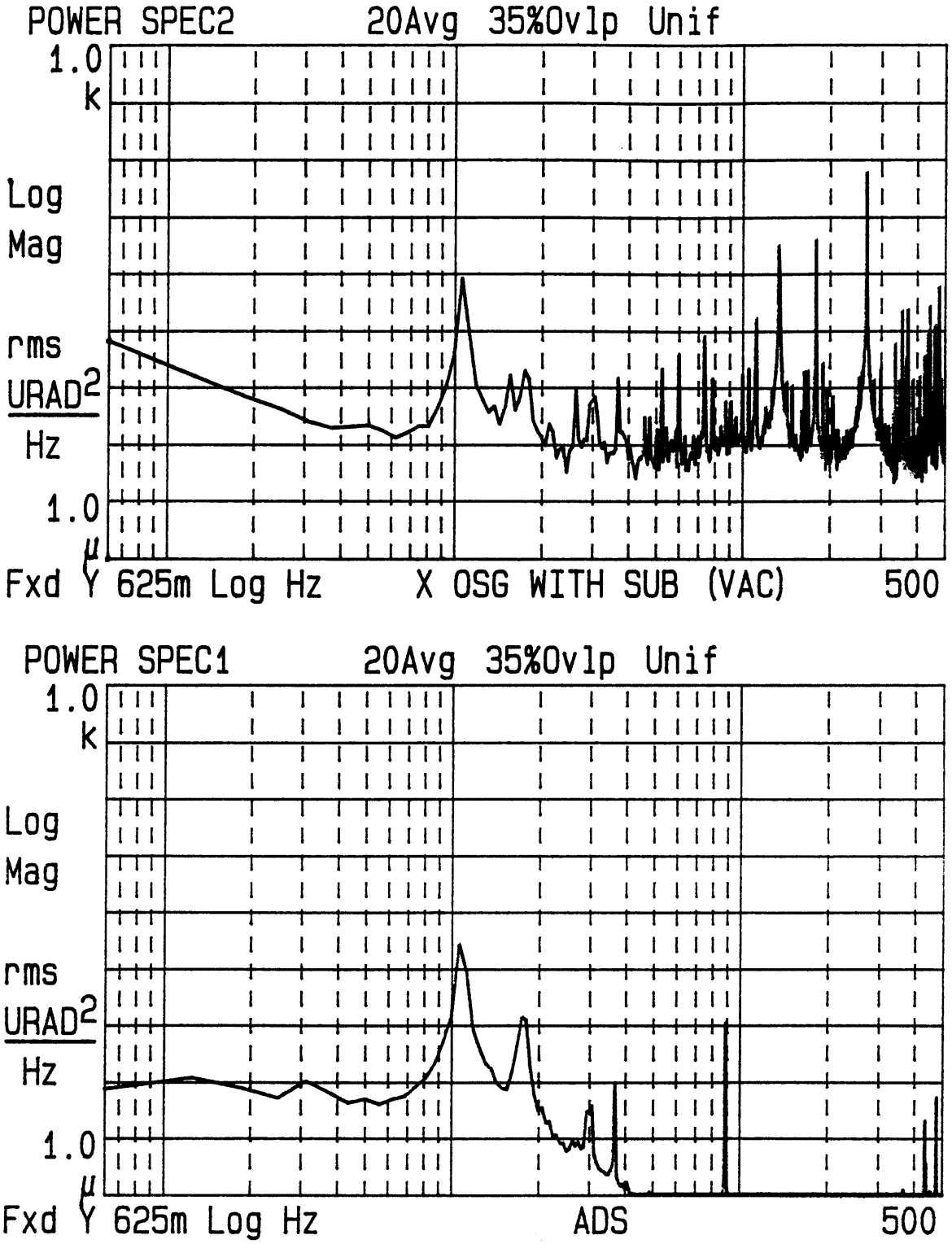

Figure 3.1-11. PSD's of x OSG and ADS. ORG evacuated, low torque-rebalance loop, Subtraction Eliminator on.

at the spin-speed, the amplitude of the spin-speed sinusoid must be approximately $(2x92\ \mu rad^2)^{0.5} = 13.6\ \mu rad$. Note this value goes down to around 12 μrad when the ORG is filled with air at 1 atm.

Before intensity normalization was used (see "Light Source Selection", section 2.2.1.2), ORG beam intensity variation had a dramatic effect on the magnitude of the spin-speed discrete. The slightest change in light source alignment would drastically change the magnitude of the spin-speed discrete and its harmonics. Once intensity normalization was used, however, much more consistent measurements were obtained.

Like the ESG, after the spin-speed the next largest discrete-frequency noises are the spin-speed harmonics (see fig. 3.1-12).

By comparing the spin-frequency discrete and its harmonics in the ESG and OSG, one can see no simple correlation. This suggests that the discrete-frequency noise in the ESG and OSG are caused by separate things. As mentioned in section 3.1.1, the ESG spin-frequency discrete and harmonics are most likely caused by rotor asymmetries. The OSG spin-frequency discrete and harmonics are probably mainly caused by three things: first, by ORG optics misalignment and asymmetries and second, by the diffraction process.

One cause of the spin-frequency discrete in the OSG is probably because the pinhole and lens center are not lined up parallel to the rotor spin axis (see "Pinhole Mechanization", section 2.2.1.1). When the ORG was rebuilt, small weights were added to the rotor to bring the spin axis closer to the OSG null axis, but it was difficult to do it precisely. Note this was at the expense of the ESG--i.e. the ESG spin-frequency discrete got worse.

The diffraction pattern can cause harmonics because the diffraction pattern through the pinhole is really infinitely wide, although the

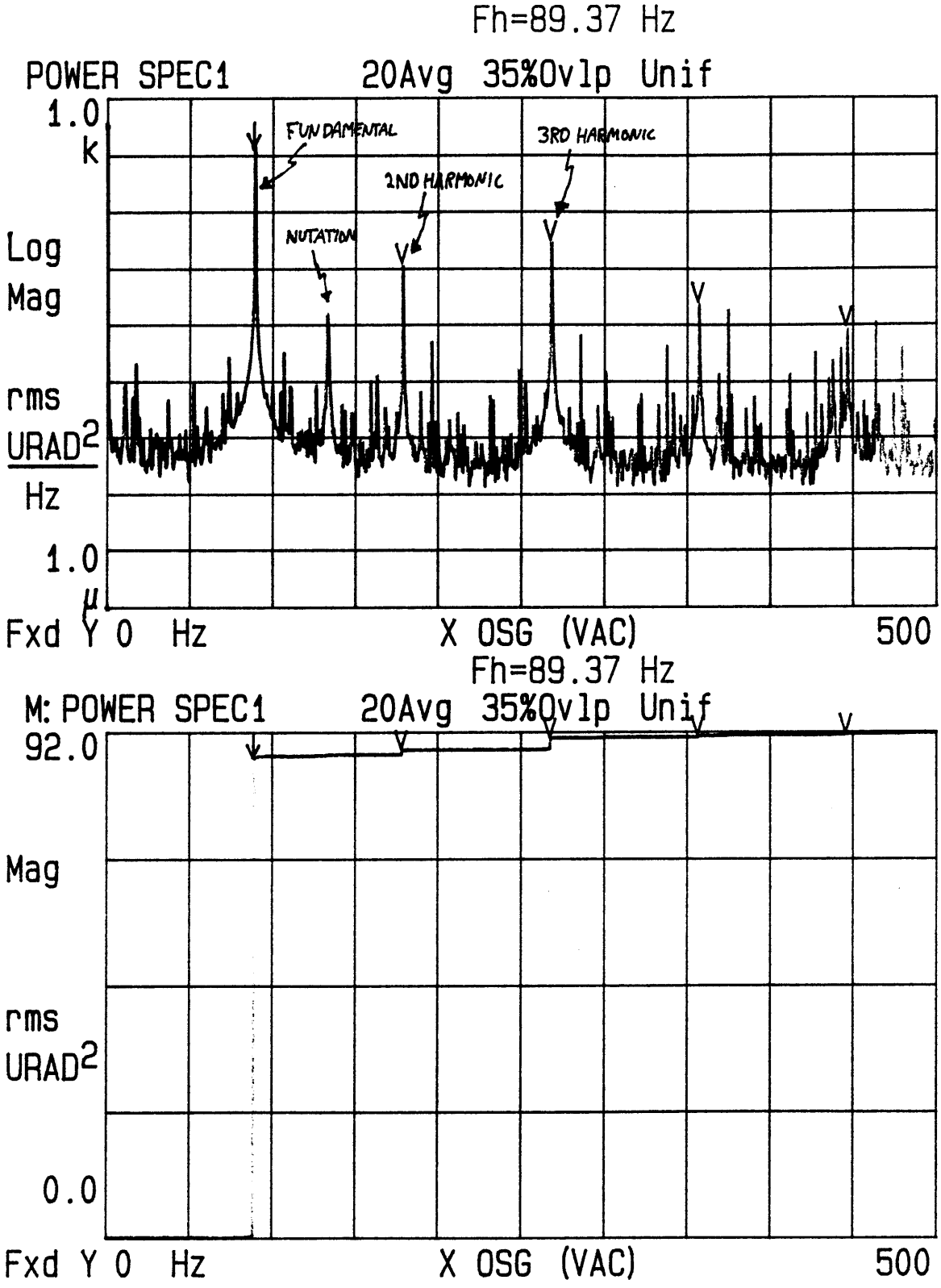

Figure 3.1-12. PSD of x OSG with linear scale. ORG evacuated, low torque-rebalance loop.

rings get dimmer and dimmer. All of the pattern gets cut off except for what gets through the lens (the center spot and two rings).

There are two places the diffraction pattern can be cut off. The first is inside the rotor. If the light source enters the pinhole at an angle, the pinhole is off center, the rotor opening is not a perfect circle, etc., the diffraction pattern that gets through the lens won't be rotationally symmetric. Since the DYNAC measures movement by measuring the ratio of light falling on two photo-cells, if the light beam is not rotationally symmetric, then as the beam spins, the DYNAC will sense spin-frequency movement even if the beam is sitting still (see fig. 3.1-13). And most likely the movement won't be a pure sinusoid, so harmonics will be generated.

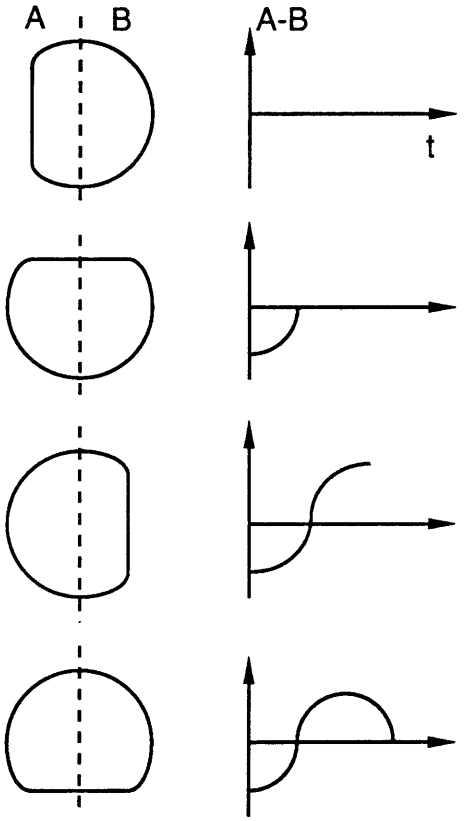

Figure 3.1-13. Drawing that shows the DYNAC will measure a false periodic movement if the beam is rotating and its cross-section is not rotationally symmetric. On the left is an exaggeration

of the ORG beam cut off by the rotor lens being shone on the DYNAC bi-lens, and on the left is the output of the DYNAC vs time.

The other place the diffraction pattern can be cut off is by a non-rotating obstruction. The collimating lens diameter is 0.70 in and the ORG output window is 0.75 in, so it is unlikely the beam is cut off in this manner. But if the beam is cut off by a non-rotating obstruction, false spin-frequency and its harmonics movement is detected by the DYNAC. It was found that when the ORG beam was sent through a piece of paper with a hole that obstructed part of the ORG beam, the harmonics would change dramatically.

With the above facts in mind, the ORG beam was sent through a hole a little larger than the inner circle of the diffraction pattern. This took the diffraction rings out of the picture and reduced some of the effect of the diffraction pattern cut-off. The second and third harmonics were reduced by about a factor of two, and the other harmonics were reduced also (see fig. 3.1-14). It is not currently known why better harmonics reduction was not achieved.

As with the ESG, in addition to the discrete-frequency noise, the OSG contains wide-band noise. This noise floor is mainly caused by four sources: gas inside the ORG, air outside the ORG that the beam travels through, the light source, and the torque-rebalance loops. Unlike the ESG, electrical noise in the OSG is negligible. This is because the only electronics for the OSG are those in the DYNAC, and the DYNAC is very quiet (see fig. 3.1-15).

As with the ESG, gas inside the ORG adds a lot of noise to the OSG. The top PSD in fig. 3.1-16 is the OSG when the ORG is filled with air at 1 atm, and the bottom is when the ORG has a near vacuum inside.

As mentioned in the "Light Source Selection" section (section 2.2.1.2), the laser is very sensitive to back reflections. The top plot in fig. 3.1-17 is the OSG PSD with more back reflections, and the top plot in fig. 3.1-18 is with less back reflections. Note: the wheel

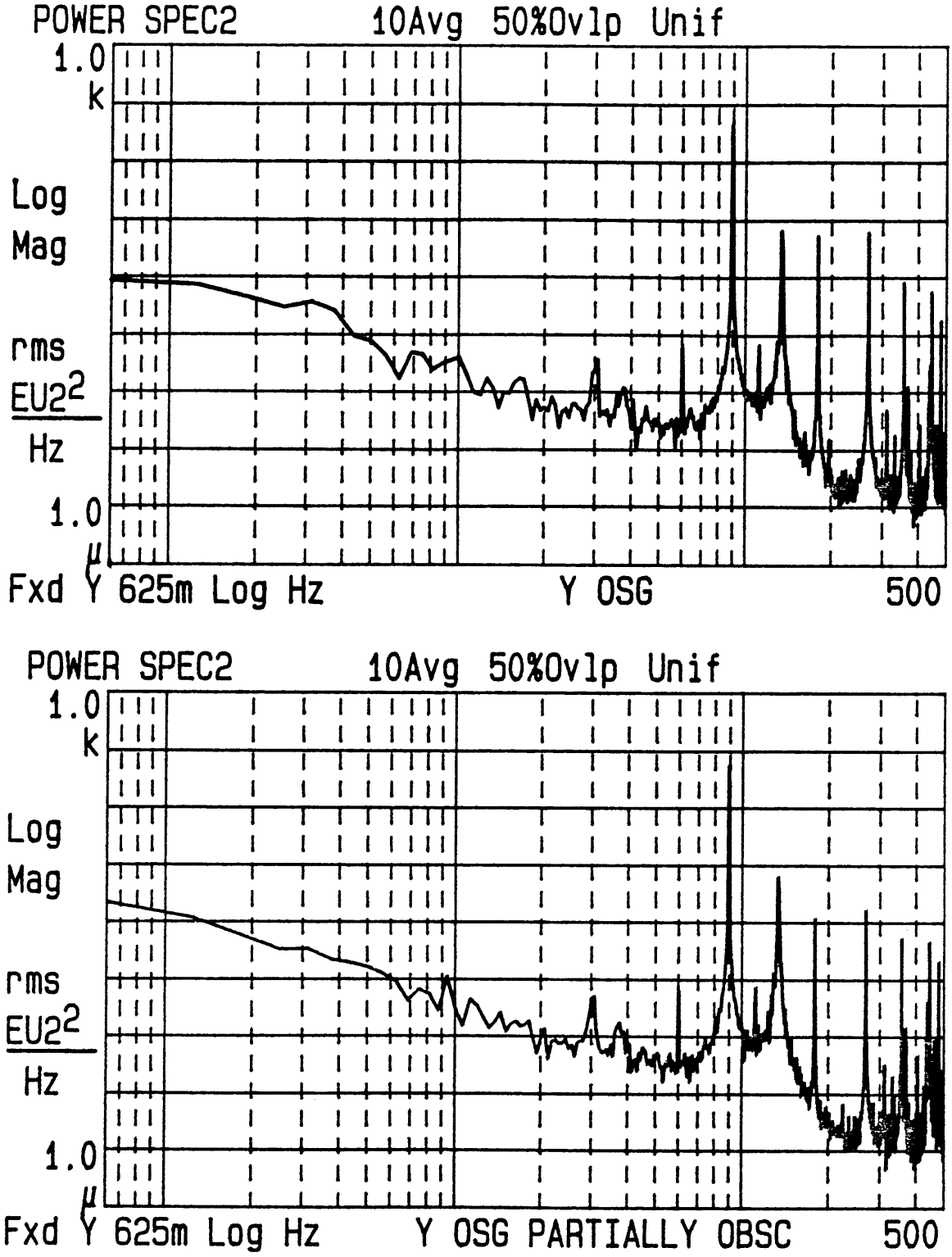

Figure 3.1-14. PSD's of x OSG with and without beam obstruction. The bottom plot is the OSG after the beam was sent through a hole that allowed only the inner circle of the diffraction pattern to pass. Note the decrease in the second and third spin-frequency harmonics.

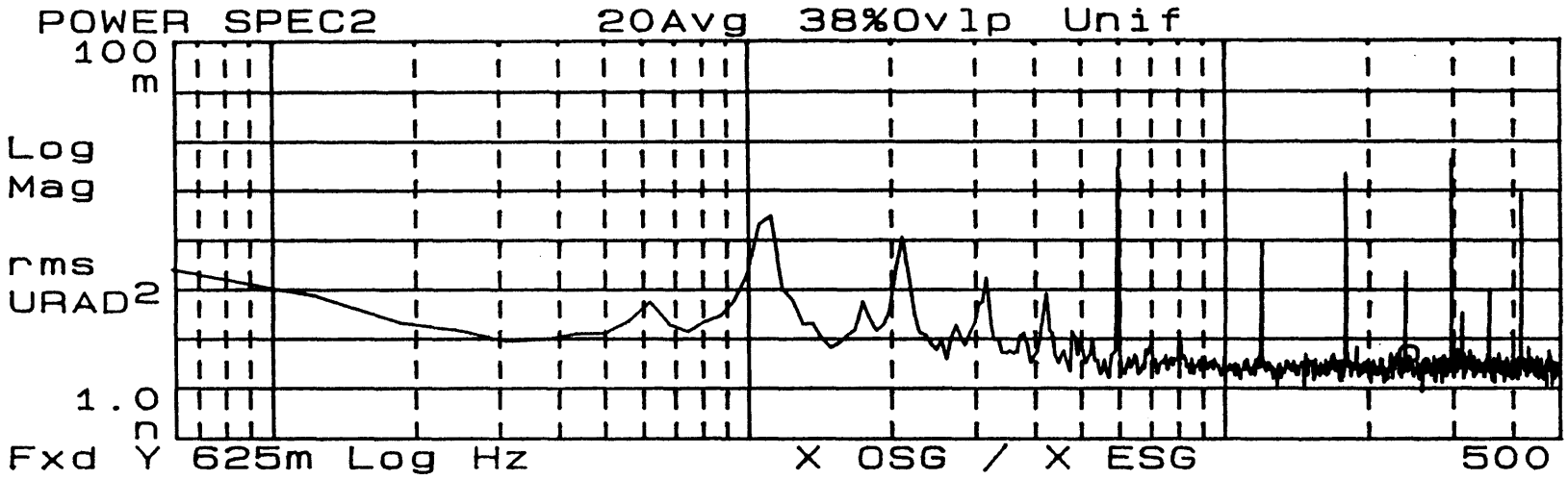

Figure 3.1-15. PSD of x OSG with light source off. Note: this measurement had to be taken *without* intensity normalization.

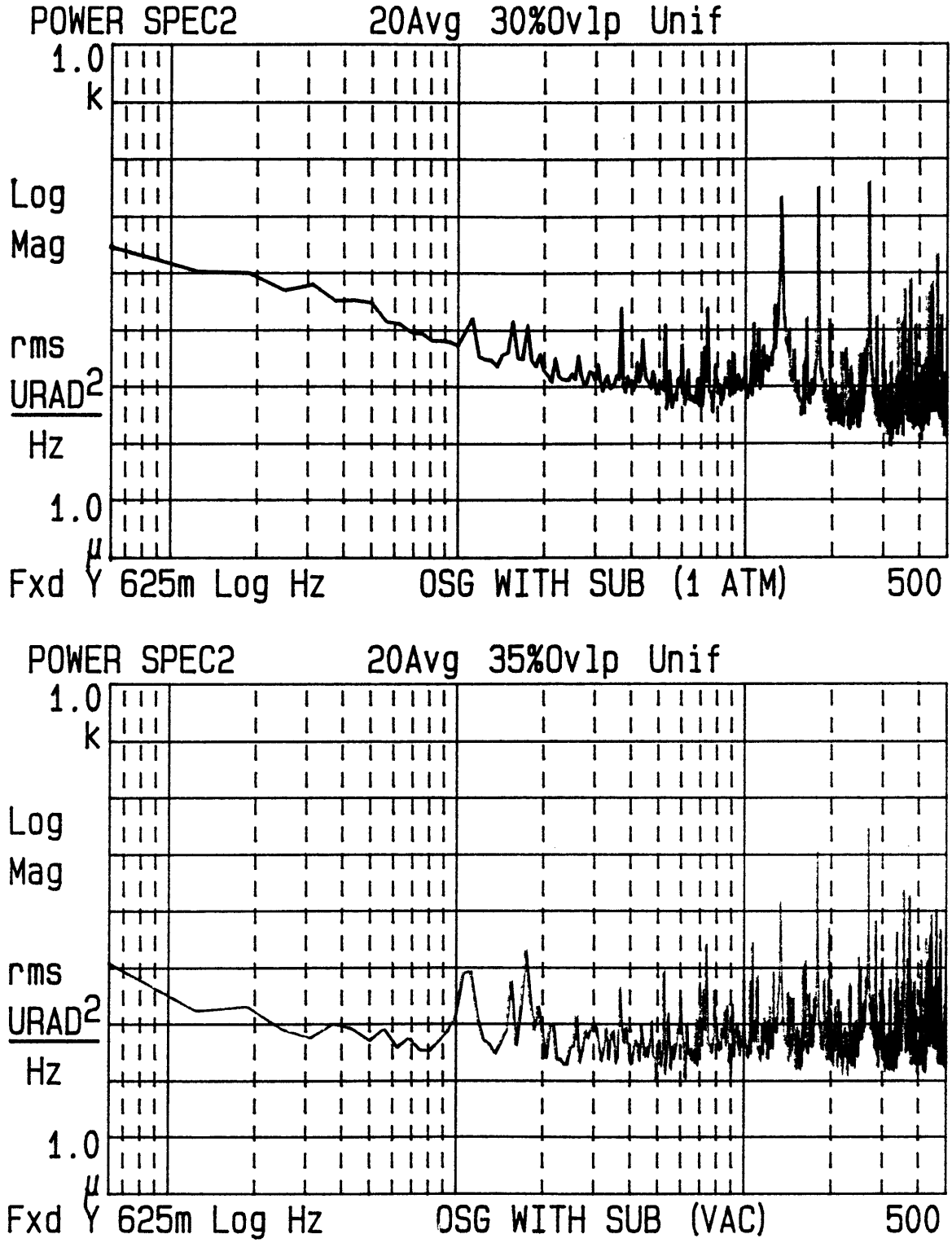

Figure 3.1-16. PSD's of x OSG with and without gas. Top plot is ORG filled with air at 1 atm. Bottom plot is ORG evacuated. Low torque-rebalance loop, Subtraction Eliminator on.

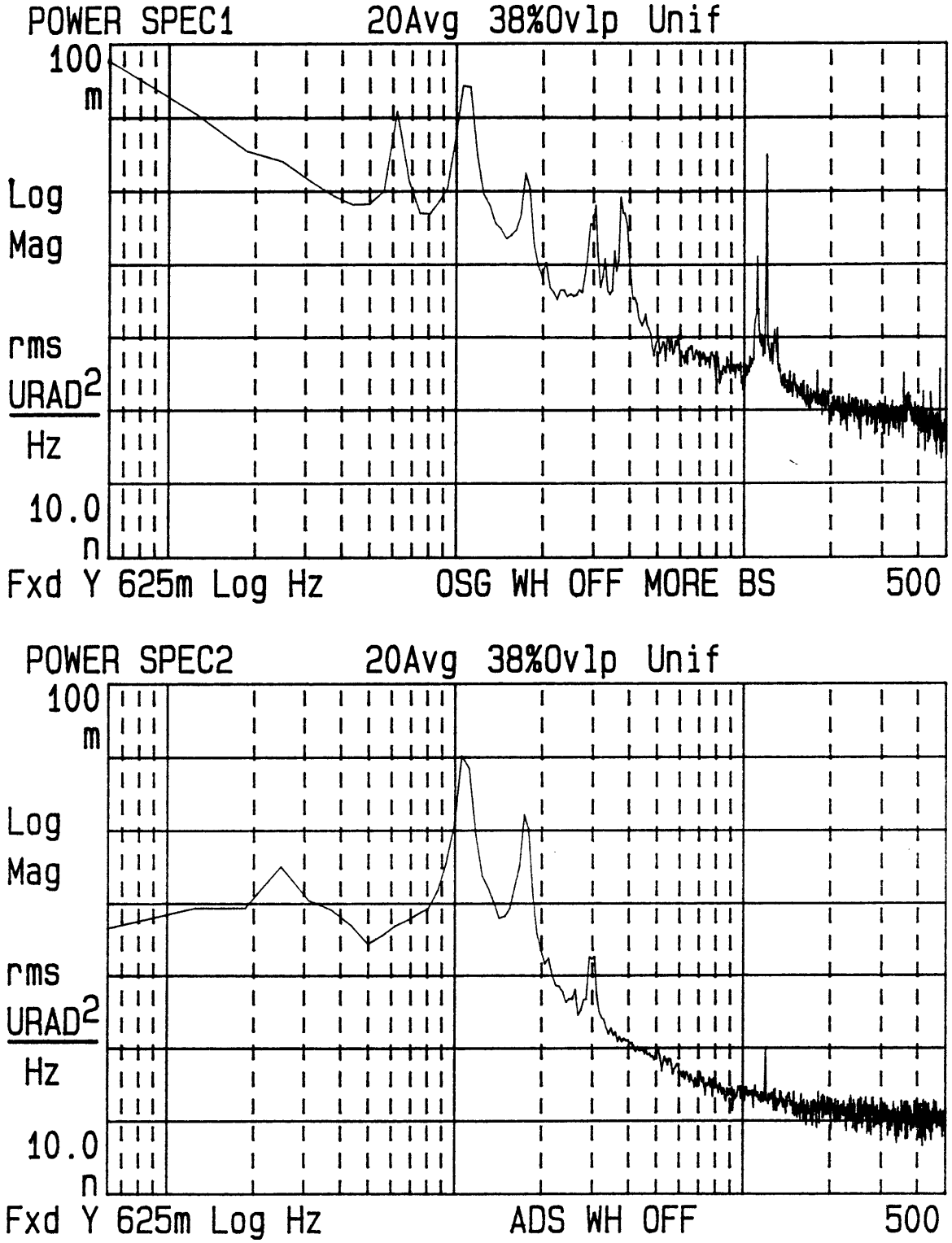

Figure 3.1-17. Top plot is OSG PSD with wheel off, more backscatter into laser. Bottom plot is ADS.

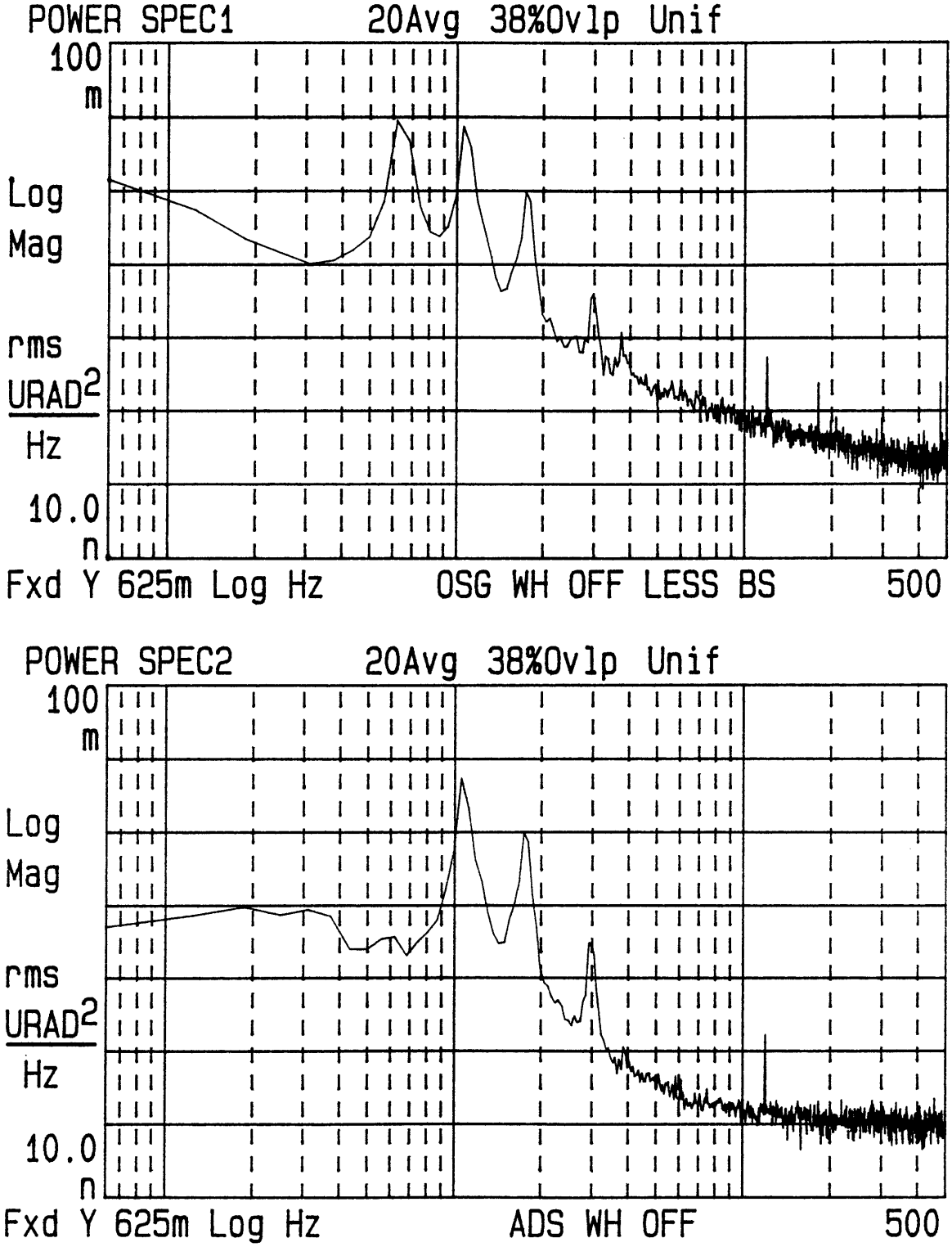

Figure 3.1-18. Top plot is OSG PSD with wheel off, less backscatter into laser. Bottom plot is ADS.

was not spinning for these measurements. Below about 30 Hz is actual movement, but above 30 Hz is light source noise. When there is a lot of back reflection, some of this noise is on the order of the noise seen when the wheel is spinning.

Another cause of wide-band noise is air outside the gyro. As the laser beam and ORG beam pass through air, they pick up much noise if the air isn't still. This noise is high at low frequencies and falls off quickly with increasing frequency. Air protection, such as surrounding the beams with cardboard tubes, greatly reduces the air noise.

The wide-band noise in the OSG is larger than in the ESG. This is most likely because of the high laser noise.

Thus the least noise in the OSG is obtained when the ORG has a near vacuum inside, the torque-rebalance loops are open, the spin-frequency noise is removed by the eliminator, and the least backscatter goes into the laser. Fig. 3.1-19 shows the total noise from 1 to 100 Hz for this case is 0.020 rms μrad^2, or 200 nrad. Note that about half of that noise isn't really noise but actual movement since the ADS sees 0.0091 rms μrad^2.

3.1.3 Summary of ORG Noise

There are two types of noise in the ESG and OSG--discrete-frequency noise and wide-band noise. The discrete-frequency noise in the ESG at the spin frequency and its harmonics is most likely caused by asymmetries in the rotor. The discrete-frequency noise in the OSG at the spin frequency and it harmonics is most likely caused by lens-pinhole misalignment and diffraction pattern obstruction.

The wide-band noise in the ESG is primarily caused by gas inside the ORG, the torque-rebalance loops, and the electrical pick-offs. When the gas is removed and the torque-rebalance loops openend, the

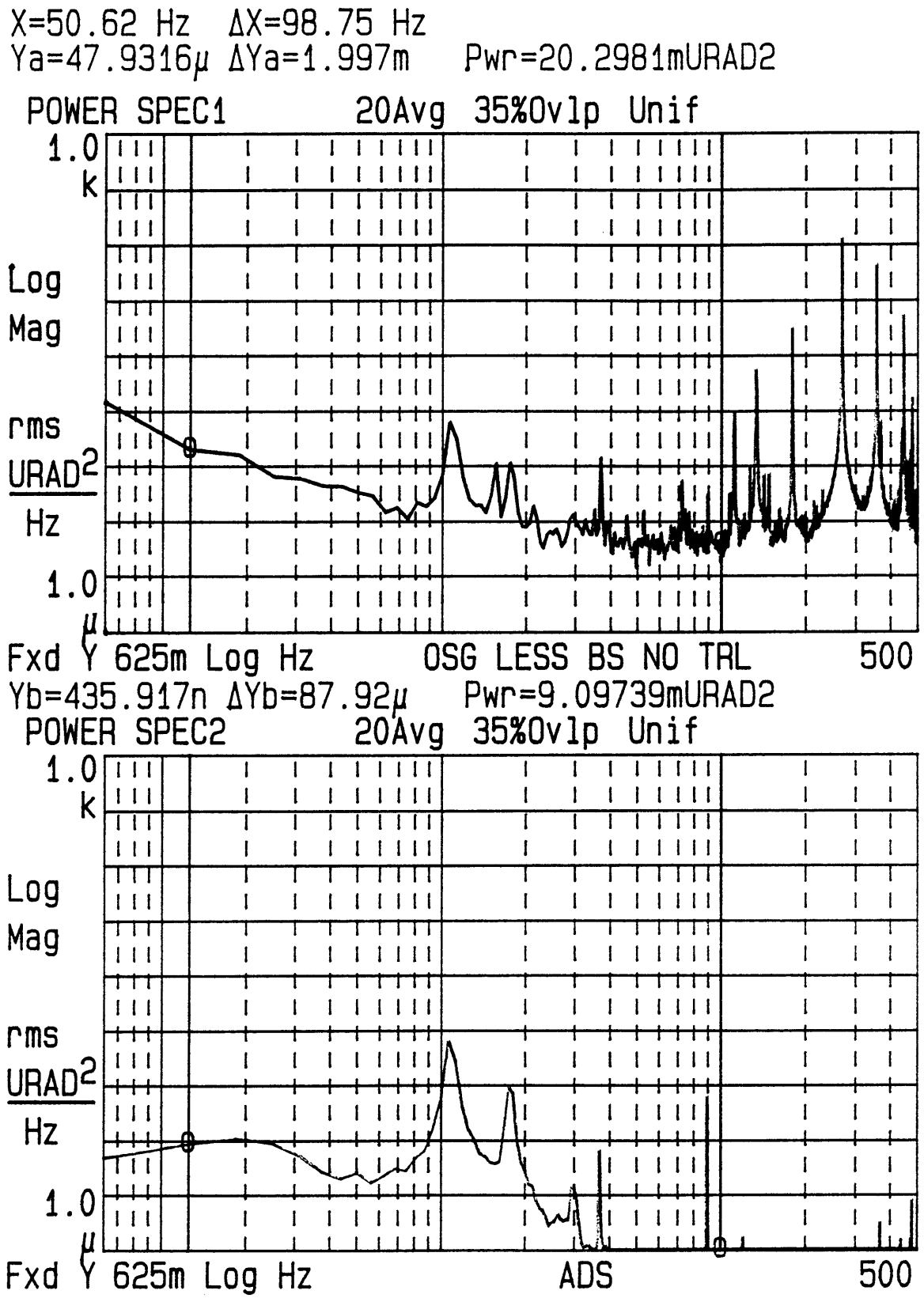

Figure 3.1-19. PSD of x OSG. ORG evacuated, torque-rebalance loops open, Subtraction Eliminator on, laser aligned for small backscatter, thorough beam air protection.

wide-band noise appears to consist primarily of the noise in the electrical pick-offs.

The wide-band noise in the OSG is primarily caused by gas inside the ORG, the torque-rebalance loops, air the ORG beam must pass through outside the instrument, and the light source. When the gas is removed, the torque-rebalance loops opened, and the beam protected from air currents, the wide-band noise appears to consist primarily of the light source noise. The light source noise can be reduced by reducing the backscatter into the laser, but the noise is still higher than the ESG electrical noise. It appears that if one could obtain a very quiet light source, the OSG noise could be lowered significantly.

3.2 Discrete-Frequency Noise Compensation #1--Subtraction Eliminator

This section describes a device created by the author that reduces the discrete-frequency noise in the ORG outputs.

3.2.1 Basic Principles

A phase-locked loop (PLL) can be combined with an amplitude-control loop (ACL--devised by the author) to create a sort of notch filter. This notch filter, called the Eliminator, seeks out the largest periodic signal in a certain frequency range in the input and subtracts out the fundamental component. The Eliminator can be used to remove the discrete-frequency noise in the OSG and ESG outputs.

This section describes phase-locked loops; then it describes amplitude-control loops; and finally it puts a phase-locked loop and an amplitude-control loop together and describes the Subtraction Eliminator.

3.2.1.1 Phase-Locked Loops

A phase-locked loop (PLL) is a control system that controls a variable-frequency oscillator (a voltage-controlled oscillator or VCO) (see refs. 4 and 5). If the input to the PLL contains a large periodic signal, the PLL will control the oscillator so as to produce a periodic signal of the same frequency. The block diagram of a PLL is shown in fig. 3.2-1.

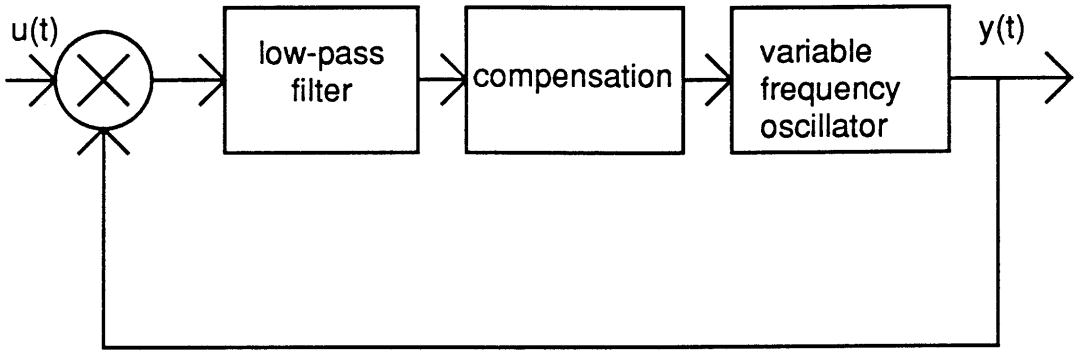

Figure 3.2-1. Basic block diagram of a phase-locked loop. Note: the "X" inside the circle implies multiplication.

Even though a PLL is a non-linear system, it can be approximated as a linear system when the oscillator is of the same frequency as the large periodic signal in the input and near 90° out of phase. This condition is considered the "in-lock" condition.

To analyze what a PLL actually does (see ref. 4), let the input be

$$u(t) = O(t) + A_n \sin(\omega t),$$

where $A_n \sin(\omega t)$ is the fundamental component of the large periodic signal in the input signal, and O(t) is the rest of the input signal. Let the output be

$$y(t) = A_p \cos(\omega t + \phi),$$

where $A_p \cos(\omega t + \phi)$ is the signal generated by the oscillator.

After the multiplication, the signal is

$$(O(t) + A_n\sin(\omega t))A_p\cos(\omega t + \phi),$$

which can be rewritten as

$$O(t)A_p\cos(\omega t+\phi) + 0.5A_pA_n\sin(2\omega t+\phi) + 0.5A_pA_n\sin(-\phi).$$

After the low pass filter, this signal can be approximated by taking only it's DC component:

$$-0.5A_pA_n\sin(\phi).$$

If ϕ is small, this can then be approximated by

$$-0.5A_pA_n\phi.$$

Thus the input to the variable-frequency oscillator is proportional to the phase difference between the periodic signal in the input and the output of the oscillator plus 90 degrees. In other words, the PLL tries to drive the oscillator to produce a signal of the same frequency as a large periodic signal in the input but exactly 90 degrees out of phase. Note this is only the case when the PLL is in an in-lock condition.

If the input and output signals are described in terms of phase (i.e. if $u(t)=\phi_i(t)$ and $y(t)=\phi_o(t)$) then the PLL can be approximated by a linear system (see ref. 4). In this case, the multiplier can be considered as a subtracter followed by a gain, since the low-frequency value of the output of the multiplier is proportional to the difference in phase. The gain is $0.5A_pA_n$ as shown earlier. The low-pass filter and compensation remain unchanged since they already operate on a signal which is proportional to phase. The VCO can be considered as an integrator with some gain. One way of showing the VCO can be considered as an integrator is imagining the input to the oscillator being a constant. The output of the oscillator then continually

ramps in phase, behaving like an integrator. The block diagram of this simplified PLL is shown in fig. 3.2-2.

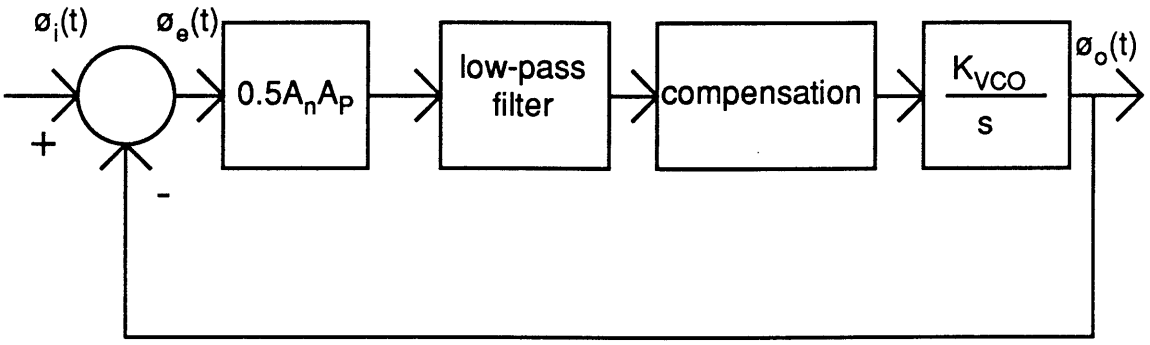

Figure 3.2-2. Phase-locked loop as a linear system. Note the units of the variables in the loop are radians.

There are a few important things to note about this PLL model.

- This loop is stable without the compensation block, but without compensation there will be a steady-state error in phase.
- The gain of the loop is dependent on the amplitude of the periodic signal which is being locked to.
- This model is only valid for low frequencies since the output of the multiplier contains high frequency terms that are neglected in this model.
- This model is also only valid if the PLL is in-lock.

See refs. 4 and 5 for more information on PLL's.

3.2.1.2 Amplitude-Control Loops

An amplitude control loop (ACL) is a control system devised by the author that subtracts out a single-frequency component of an input signal. In other words, if the input contains a sinusoid, the output will be the same as the input signal except there will no longer be a sinusoid in the signal. The block diagram of an ACL is shown in fig. 3.2-3.

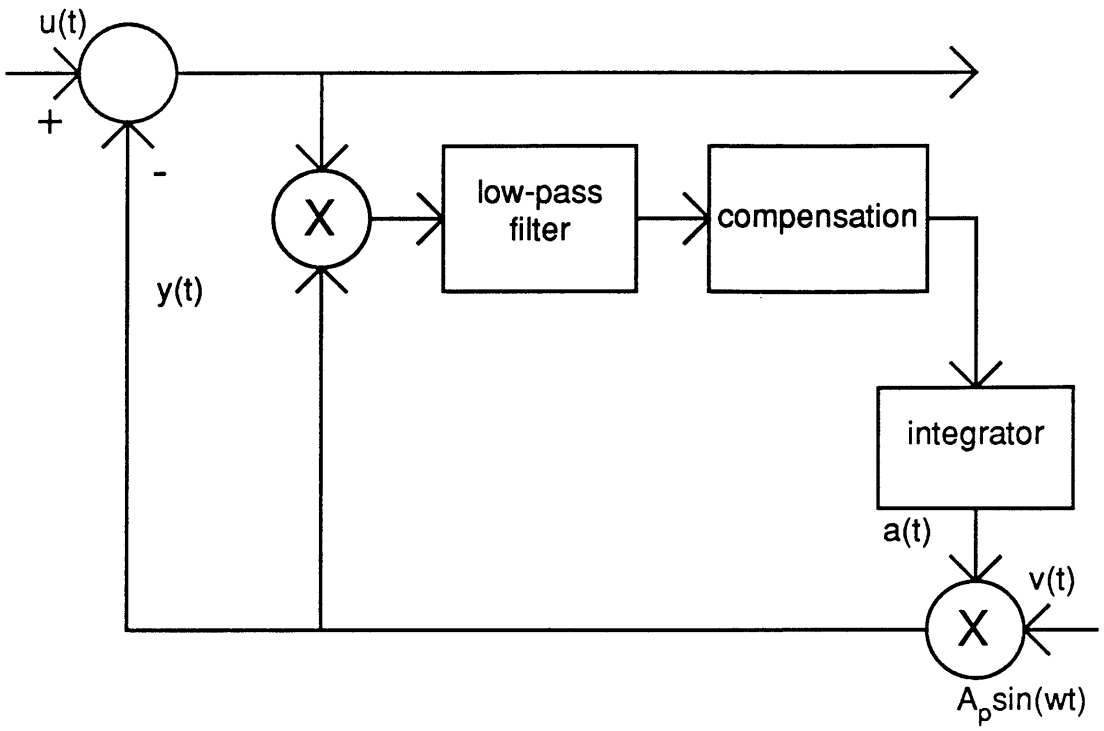

Figure 3.2-3. Basic block diagram of an amplitude control loop. Note: the 'X's inside the circles imply multiplication.

Basically what happens is a sinusoid is created somehow that is in phase with a sinusoid of the same frequency in the input. This sinusoid is then subtracted from the input. The ACL controls the amplitude of the subtracting sinusoid so it exactly cancels the sinusoid in the input.

Let the input be

$$u(t) = O(t) + A_n \sin(\omega t),$$

where $A_n \sin(\omega t)$ is a sinusoid in the input. Let the created sinusoid be

$$v(t) = A_p \sin(\omega t).$$

Let the output of the ACL integrator be

$$a(t) = A_a.$$

Thus the signal being subtracted from the input is

$$y(t) = a(t)v(t) = A_aA_p\sin(\omega t).$$

Thus the output of the subtracter is

$$u(t) - a(t)v(t) = O(t) + A_n\sin(\omega t) - A_aA_p\sin(\omega t),$$

and the input to the low-pass filter is

$$(u(t) - a(t)v(t))a(t)v(t)$$

or

$$(O(t) + A_n\sin(\omega t) - A_aA_p\sin(\omega t))A_aA_p\sin(\omega t).$$

This can be rewritten as

$$O(t)A_aA_p\sin(\omega t) + 0.5A_aA_nA_p - 0.5A_aA_nA_p\cos(2\omega t) - 0.5A_a^2A_p^2 + 0.5A_a^2A_p^2\cos(2\omega t).$$

After the low-pass filter, this can be approximated as

$$0.5A_aA_p(A_n - A_aA_p).$$

Thus, the output of the low-pass filter is a signal that is proportional to the difference in amplitude between the sinusoid in the input signal and the subtracting sinusoid. The output of the integrator will then adjust itself so as to make the sinusoid amplitude in the input equal to the sinusoid amplitude of the subtraction signal, i.e. $A_a=A_n/A_p$.

Similar to the phase-locked loop, the ACL can be approximated as a linear system, except in the ACL case, the variable is amplitude and

not phase (i.e. $u(t)=a_i(t)$, $y(t)=a_o(t)$). The first multiplier can be approximated as a gain of $0.5A_n^2$, and the second multiplier isn't included. The low-pass filter, compensation, and integrator remain the same. Fig. 3.2-4 shows the block diagram of the linearized ACL.

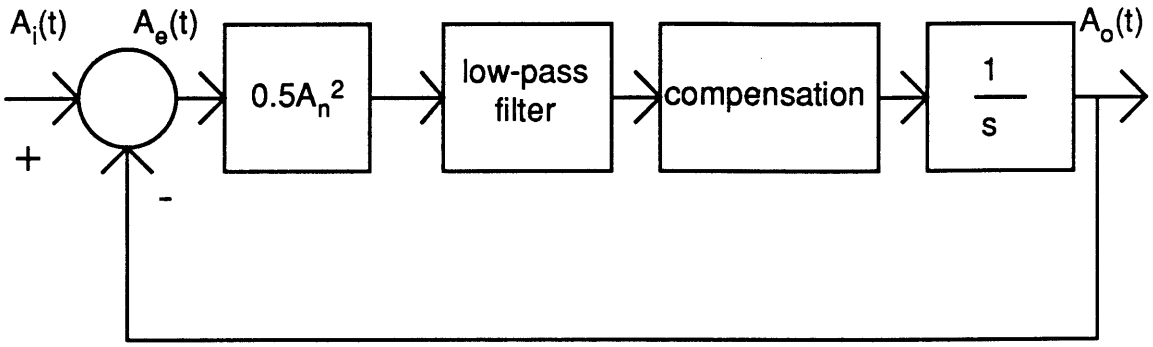

Figure 3.2-4. Amplitude control loop as a linear system.

As with the PLL model, there are a few important notes considering the ACL model.

- The ACL is stable without the compensation, but the compensation can be used to give the loop more desirable characteristics.
- The linear model is valid only if the output of the integrator (a(t)) is not zero, otherwise the ACL will sit there and do nothing.
- The linear model is only valid for low frequencies.
- The created sinusoid must be exactly in phase with the sinusoid in the input, or else the ACL will have a steady-state error.

The phase-locked loop and amplitude-control loop are merged together to create the Eliminator.

3.2.1.3 Subtraction Eliminator

The Subtraction Eliminator will filter out the fundamental component of the largest periodic signal (within a certain frequency range) in the input. It consists of a PLL that locks to a periodic

signal in the input and creates a sinusoid of the same frequency to subtract from it and an ACL that determines the amplitude of the PLL created sinusoid so as to exactly cancel the fundamental component of the periodic signal in the input. The block diagram is shown in fig. 3.2-5.

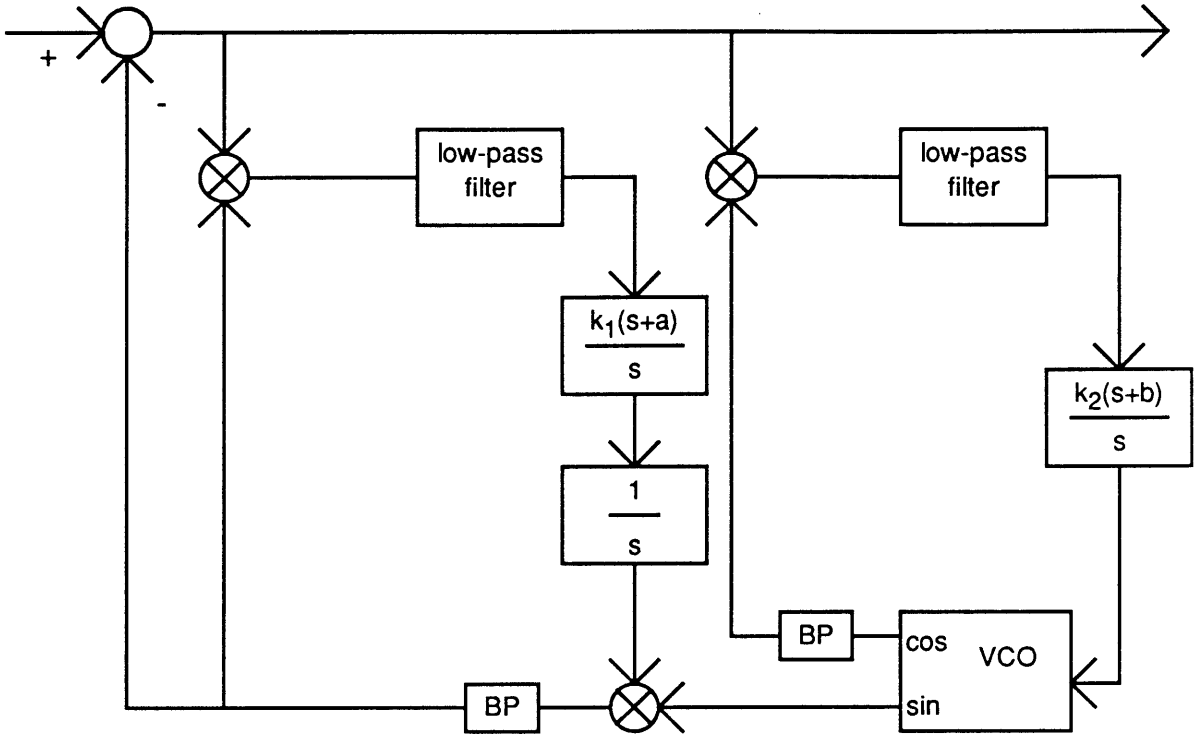

Figure 3.2-5. Block diagram of Subtraction Eliminator. Note: "BP" stands for band-pass filter.

The Eliminator consists of two parts--the PLL which is on the right side in fig. 3.2-5, and the ACL which is on the left side. The heart of the Eliminator is the voltage controlled oscillator, or VCO. The VCO produces two sinusoids 90° apart, whose frequency depends on the input voltage.

To see how the Eliminator works, note the labelled signals in fig. 3.2-6. Assume the PLL is already in-lock and $A_a \neq 0$. Let the input signal be

$$O(t) + A_n\sin(\omega t)$$

where O(t) is the desired signal and $A_n\sin(\omega t)$ is a large, unwanted, periodic signal. Assume the VCO is producing a signal of the correct frequency but a little off in phase, i.e. let the VCO signals be

$$A_p\sin(\omega t+\phi)$$

and

$$A_p\cos(\omega t+\phi).$$

Thus the Eliminator output is

$$O(t) + A_n\sin(\omega t) - A_aA_p\sin(\omega t+\phi).$$

It is desired to make $\phi=0$ and $A_a=A_n/A_p$. Then the output will just be O(t). The PLL takes care of ϕ, and the ACL takes care of A_a.

By looking at fig. 3.2-6, one can see the output of the PLL low-pass filter is

$$-0.5A_nA_p\sin\phi.$$

The PLL tries to drive this signal to zero. Thus ϕ will be driven to zero.

Also by looking at fig. 3.2-6, one can see the output of the ACL low-pass filter is

$$0.5A_aA_p(A_n\cos\phi - A_aA_p).$$

The ACL will drive this signal to zero. Thus A_a will be driven to $(A_n/A_p)\cos\phi$. If the PLL does its job, ϕ will be driven to zero, and so

A_a will become A_n/A_p. It is interesting to note the ACL depends upon the PLL, but the PLL doesn't depend upon the ACL.

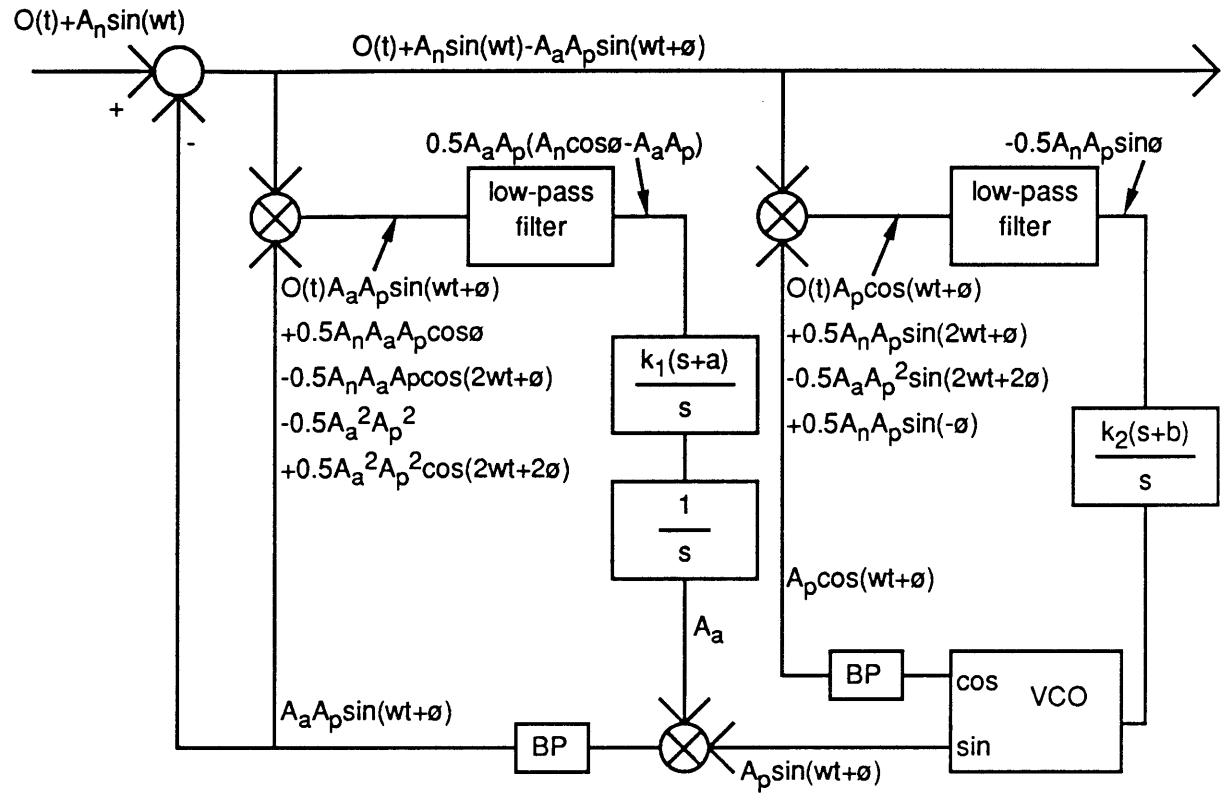

Figure 3.2-6. Block diagram of Subtraction Eliminator with labelled signals.

It may at first appear the Eliminator won't work. Once the sinusoid is exactly subtracted from the input, it may seem the PLL will have nothing to lock to. But the output of the PLL low-pass filter doesn't contain any information concerning the VCO created sinusoid subtracted from the input. In other words, the PLL sees the input as if nothing was subtracted from it!

To analyze the dynamics of the Eliminator, the PLL and ACL dynamics can be analyzed separately. This is because the PLL operation is completely independent of the ACL operation, and although the ACL operation does depend on ø, it really only depends on cos(ø). Since ø

is small, and cos(ø) doesn't change much when ø is small, the ACL operation can be considered independent of the PLL operation (once the PLL is in lock).

In the implemented Eliminator, the PLL low-pass filter is

$$\frac{d}{s+d},$$

and the PLL compensation is

$$\frac{k_2(s+b)}{s}.$$

Thus, the PLL open-loop transfer function (see fig. 3.2-2) is

$$\frac{\phi_o(s)}{\phi_e(s)} = 0.5A_nA_pk_2k_{VCO}d\frac{s+b}{s^2(s+d)}. \qquad (3\text{-}1)$$

The block diagram for the PLL control system is shown in fig. 3.2-7.

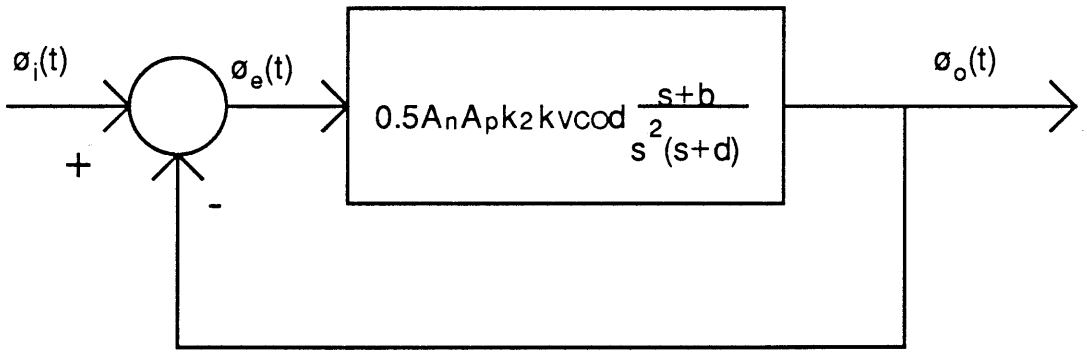

Figure 3.2-7. Block diagram of implemented PLL.

Likewise, the implemented ACL low-pass filter is

$$\frac{c}{s+c},$$

and the ACL compensation is

$$\frac{k_1(s+a)}{s}.$$

This makes the ACL open-loop transfer function (see fig. 3.2-4)

$$\frac{A_o(s)}{A_e(s)} = 0.5A_n^2 k_1 c \frac{s+a}{s^2(s+c)}. \qquad (3\text{-}2)$$

The block diagram for the ACL control system is shown in fig 3.2-8.

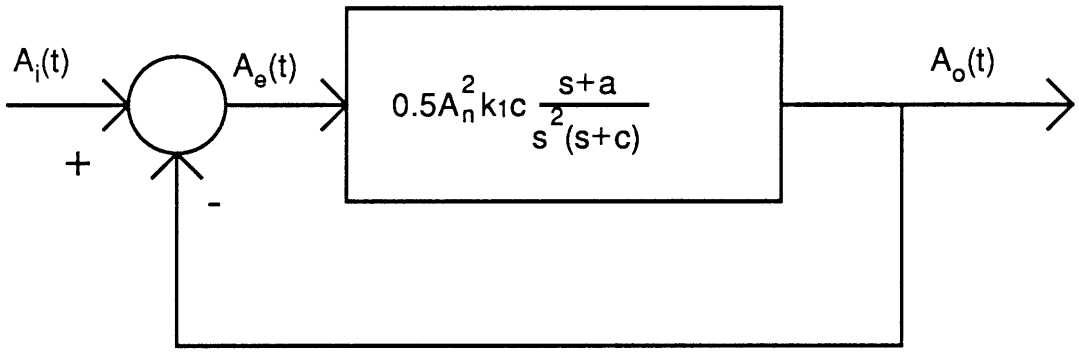

Figure 3.2-8. Block diagram of implemented ACL.

As one can see, the ACL and PLL transfer functions are the same, except the ACL gain depends on the square of the amplitude of the discrete-frequency noise, while the PLL gain varies linearly with the amplitude of the discrete-frequency noise.

Since the gains of the loops do vary with the discrete-frequency noise amplitude, the loops must be designed around some nominal point.

The above compensation was chosen to make both loops type II. This was done so the PLL would have zero steady-state error for a

constant frequency, and so the ACL would have zero steady-state error for a ramp in amplitude.

There is a trade-off in deciding the bandwidths of the PLL and ACL loops. There are reasons for making the bandwidths as small as possible.

- The smaller the bandwidths of the PLL and ACL low-pass filters, the less the amount of high frequency signal due to the multiplier will get through, and thus the more precisely the phase and amplitude can be tracked.
- The smaller the bandwidths the less the desired signal O(t) will be tracked and thus removed.

And there are reasons for making the bandwidths as large as possible.

- If the phase and amplitude of the discrete-frequency noise are moving around, the higher the bandwidths, the more closely the phase and amplitude can be tracked.

It turns out the closed-loop sensitivity functions of the PLL and ACL determine the shape of the "notch" created by the Eliminator. This is shown by giving several examples.

Several different sets of parameters were tried out in the PLL and ACL. First, the following open-loop transfer functions were tried:

$$\frac{\phi_o(s)}{\phi_e(s)} = 4722\frac{s+18}{s^2(s+20)} \qquad (3\text{-}3)$$

and

$$\frac{A_o(s)}{A_e(s)} = 2600\frac{s+18}{s^2(s+20)}. \qquad (3\text{-}4)$$

The magnitude of the closed-loop sensitivity transfer functions ($\phi_e(s)/\phi_i(s)$ and $A_e(s)/A_i(s)$) are plotted in fig. 3.2-9.

Fig. 3.2-10 shows the effect of the Eliminator with these PLL and ACL frequency responses. The top plot is the power spectral density (PSD) of the input to the Eliminator, and the bottom is the PSD of the output.

Notice how the Eliminator has taken out not only the discrete-frequency component, but also the signal surrounding the discrete-frequency component within the bandwidth of the PLL and ACL. Also notice the close correlation between the shape of the "notch" in the PSD and the ACL and PLL sensitivity transfer functions. One can see both the PLL and ACL overshoots in the PSD on either side of the notch.

To investigate the effects of the PLL and ACL independently, the next three sets of transfer functions were tried.

The open-loop transfer functions for case #2 were

$$\frac{\phi_o(s)}{\phi_e(s)} = 4722\frac{s+18}{s^2(s+20)} \qquad (3\text{-}5)$$

and

$$\frac{A_o(s)}{A_e(s)} = 2600\frac{s+9.1}{s^2(s+100)}. \qquad (3\text{-}6)$$

Figs. 3.2-11 and 3.2-12 show the results.

The open-loop transfer functions for case #3 were

$$\frac{\phi_o(s)}{\phi_e(s)} = 4722\frac{s+9.1}{s^2(s+100)} \qquad (3\text{-}7)$$

and

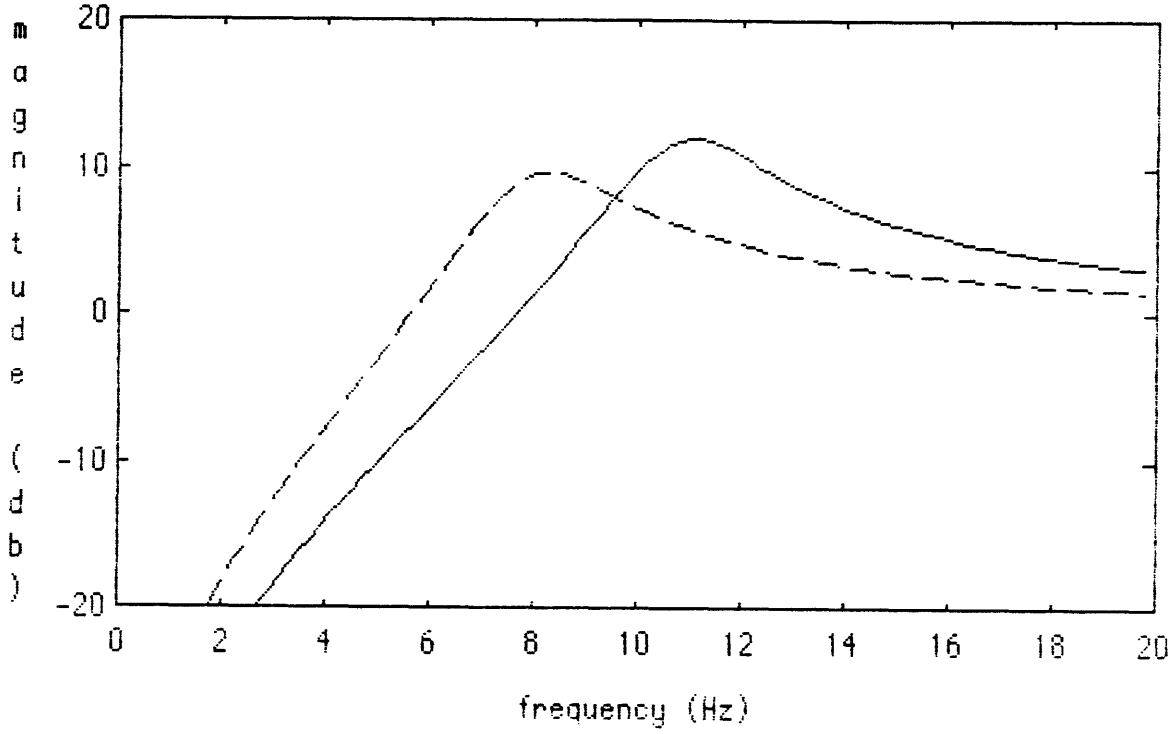

Figure 3.2-9. Closed-loop sensitivity transfer functions for case #1. The solid line is the PLL and the dashed line is the ACL. Note: the frequency is plotted on a linear scale.

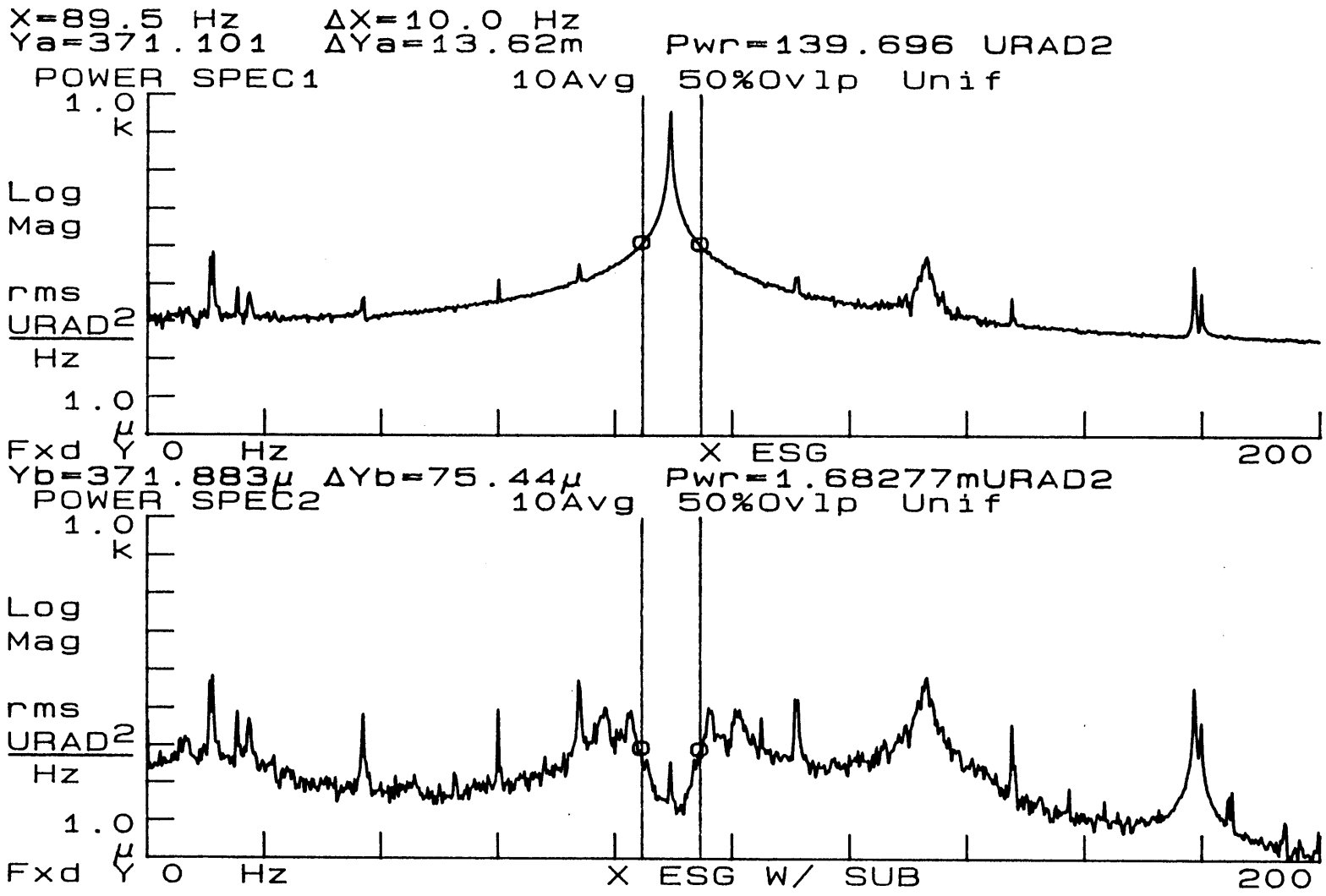

Figure 3.2-10. PSD's of input and output of the Subtraction Eliminator for case #1.

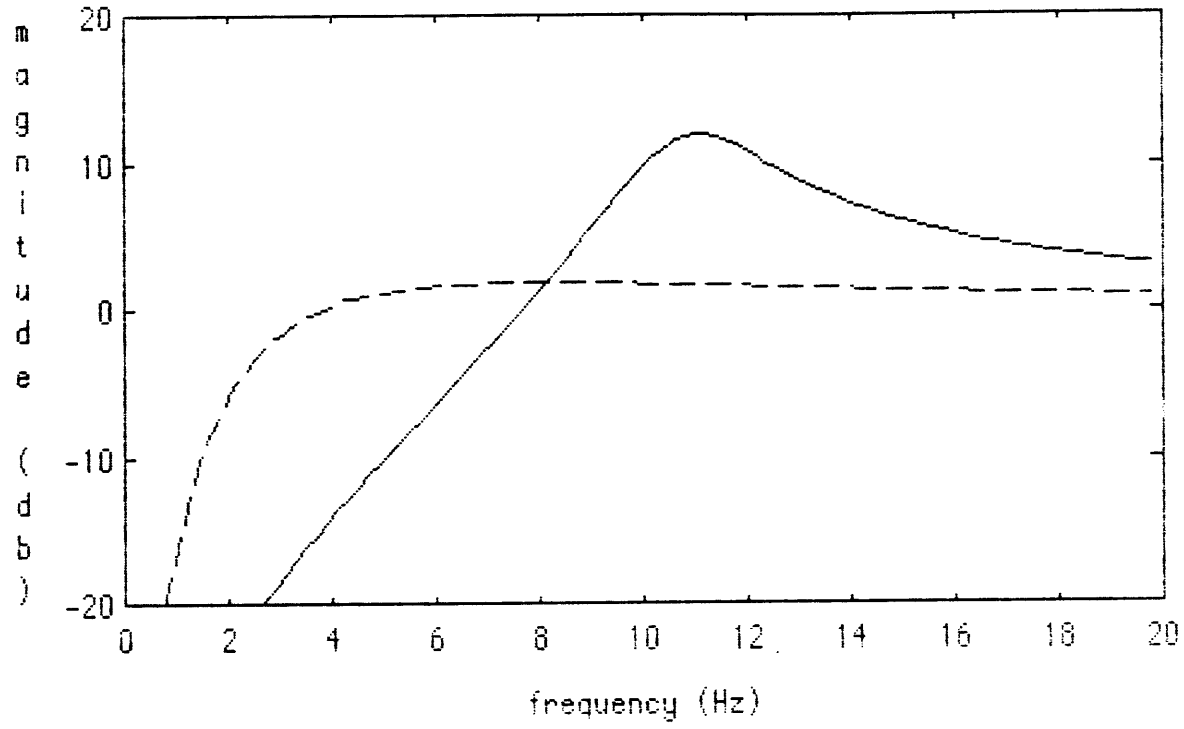

Figure 3.2-11. Closed-loop sensitivity transfer functions for case #2. The solid line is the PLL and the dashed line is the ACL.

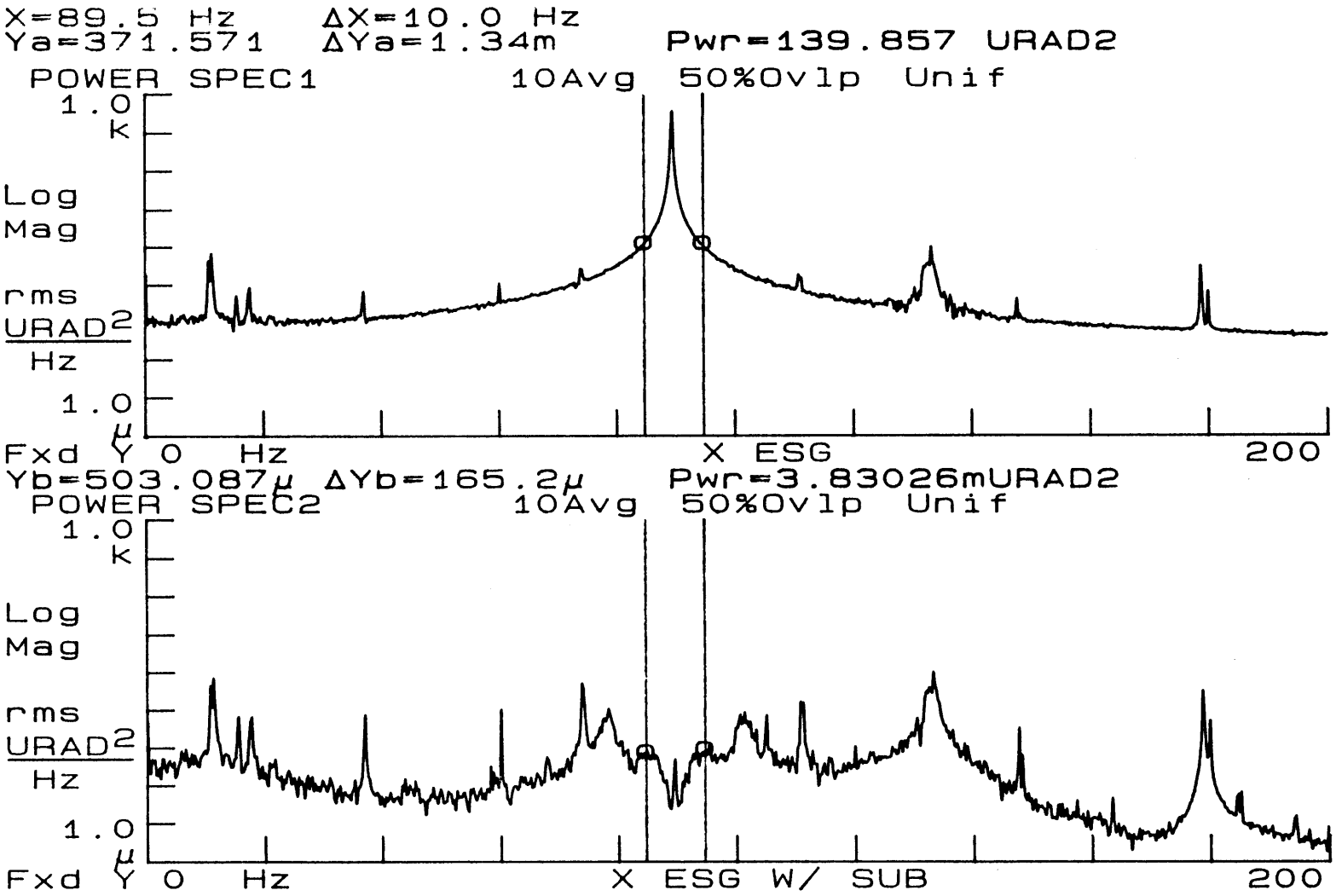

Figure 3.2-12. PSD's of input and output of the Subtraction Eliminator for case #2.

$$\frac{A_o(s)}{A_e(s)} = 2600\frac{s+18}{s^2(s+20)}. \qquad (3\text{-}8)$$

Figs. 3.2-13 and 3.2-14 show the results.

The open-loop transfer functions for case #4 were

$$\frac{\phi_o(s)}{\phi_e(s)} = 4722\frac{s+91}{s^2(s+100)} \qquad (3\text{-}9)$$

and

$$\frac{A_o(s)}{A_e(s)} = 2600\frac{s+91}{s^2(s+100)}. \qquad (3\text{-}10)$$

Figs. 3.2-15 and 3.2-16 show the results.

In case #2, only the PLL transfer function contains overshoot. The ACL contains no overshoot and has a smaller bandwidth. This situation can be seen in the PSD of the Eliminator output.

In case #3, only the ACL transfer function contains overshoot. Both the PLL and ACL have roughly the same bandwidth. This can also be seen in the corresponding PSD.

In case #4, neither the ACL nor the PLL have overshoot, and therefore there is no overshoot at all in the corresponding PSD.

It appears as if the width of the notch depends on the ACL or PLL bandwidth, whichever is smaller. With this in mind, a new set of open-loop transfer functions was tried:

$$\frac{\phi_o(s)}{\phi_e(s)} = 97.4\frac{s+19}{s^2(s+20)} \qquad (3\text{-}11)$$

and

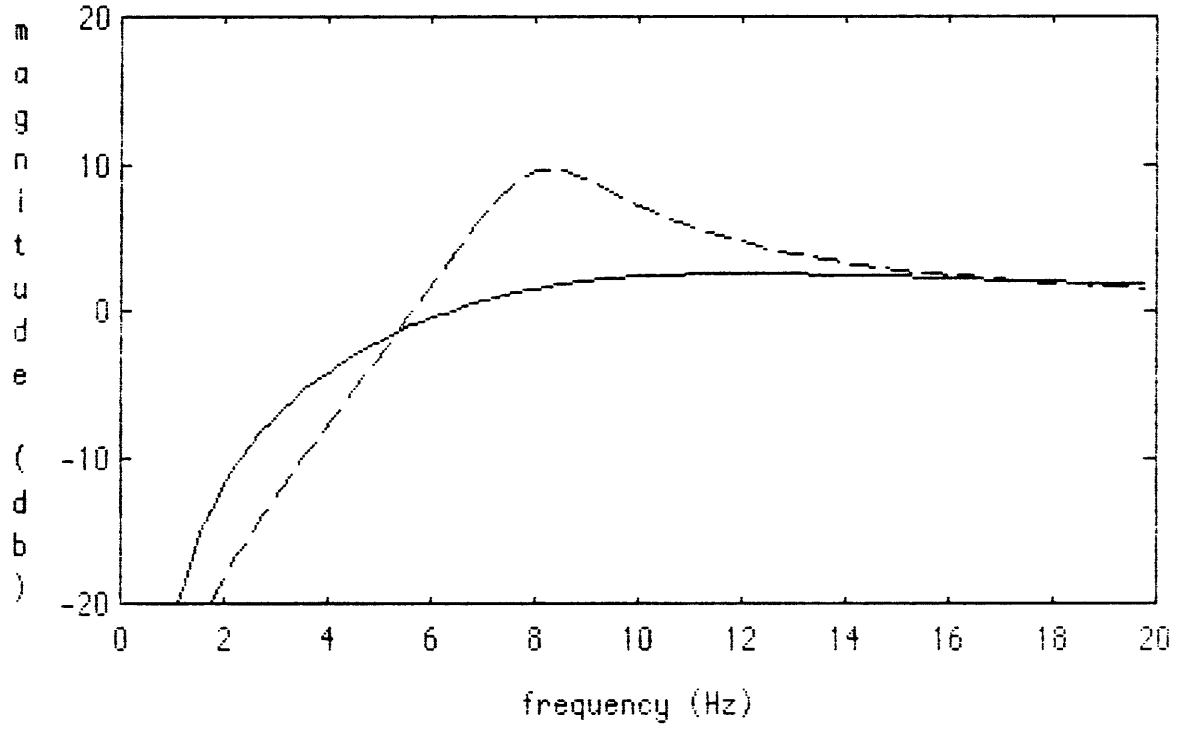

Figure 3.2-13. Closed-loop sensitivity transfer functions for case #3. The solid line is the PLL and the dashed line is the ACL.

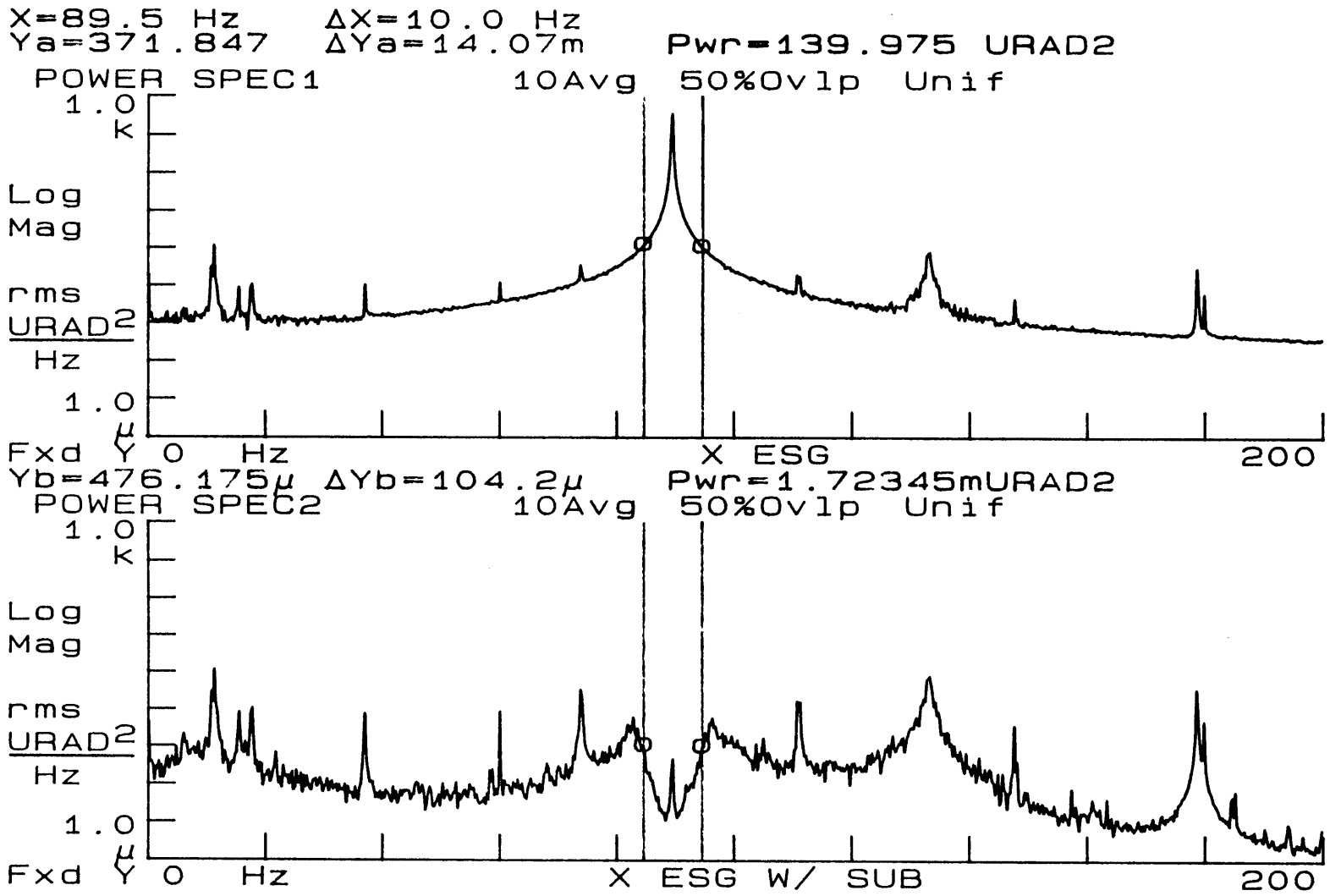

Figure 3.2-14. PSD's of input and output of the Subtraction Eliminator for case #3.

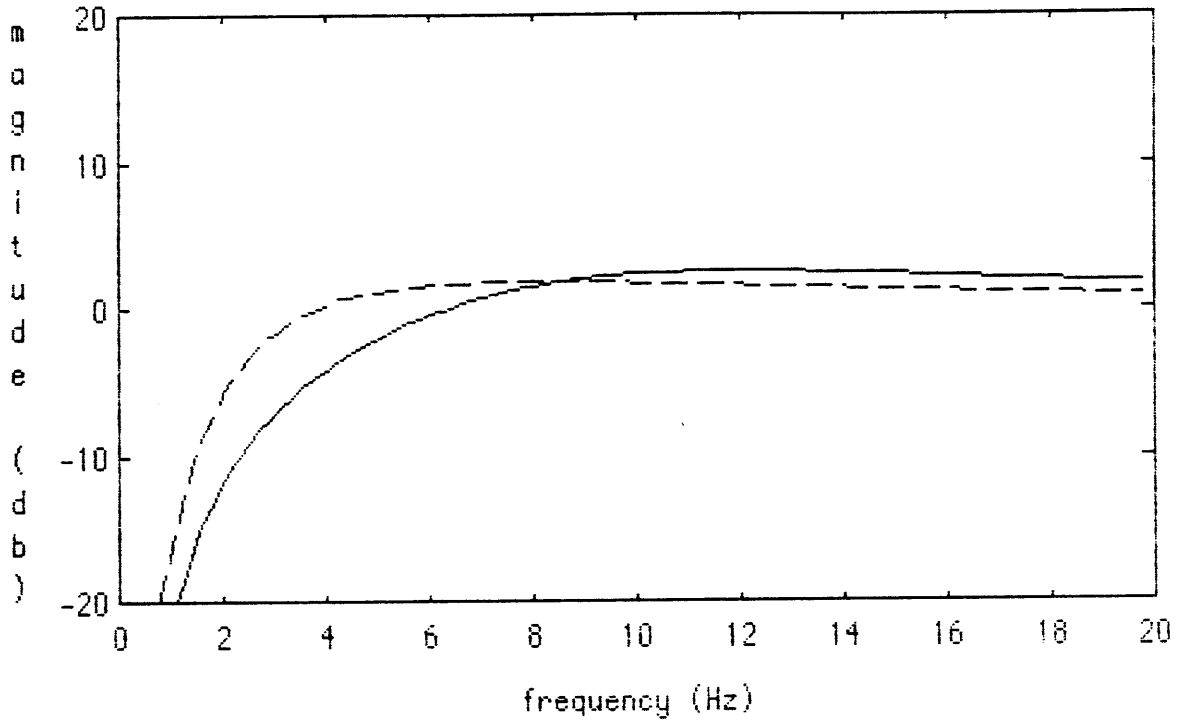

Figure 3.2-15. Closed-loop sensitivity transfer functions for case #4. The solid line is the PLL and the dashed line is the ACL.

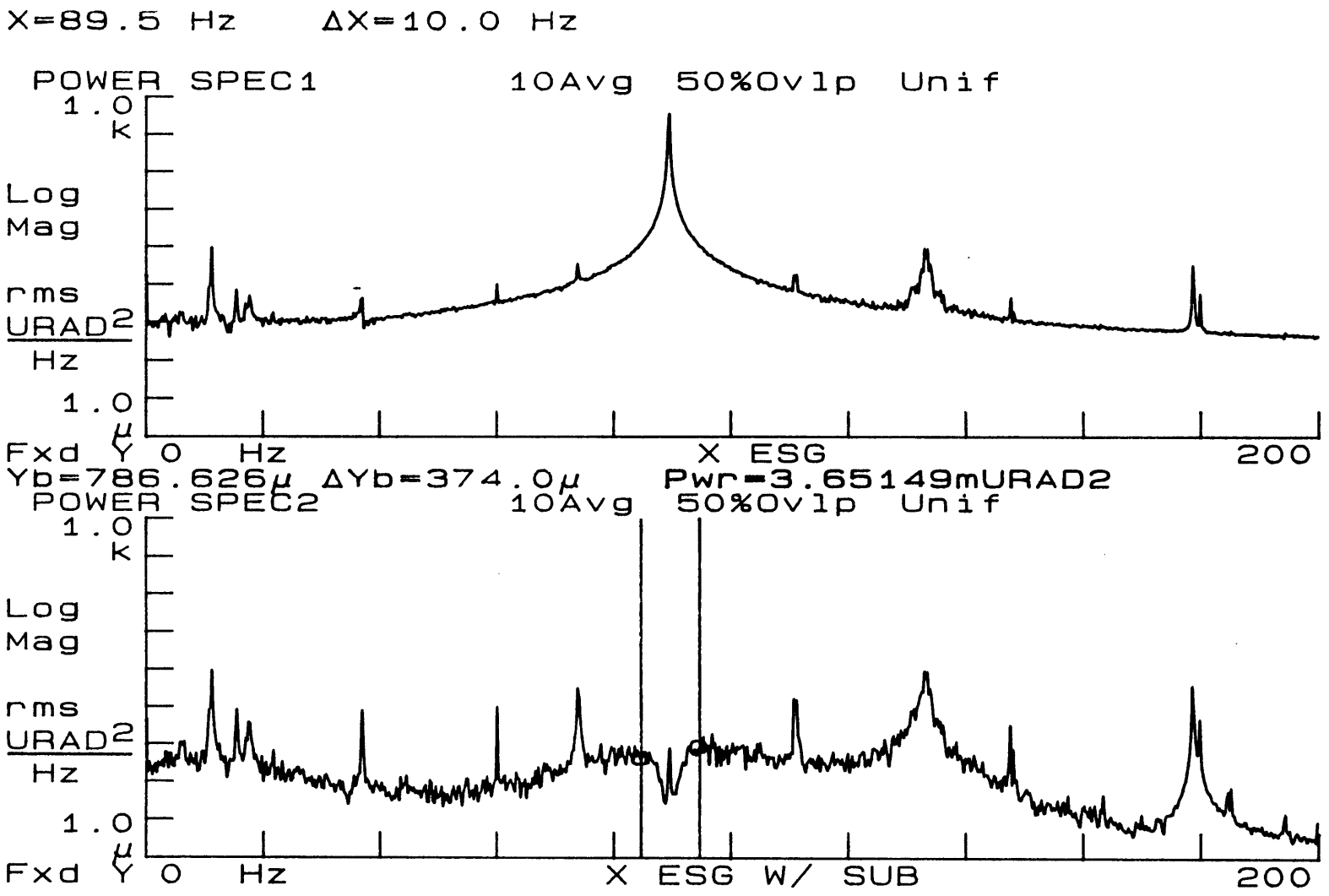

Figure 3.2-16. PSD's of input and output of the Subtraction Eliminator for case #4.

$$\frac{A_o(s)}{A_e(s)} = 48.5\frac{s+18}{s^2(s+20)}. \qquad (3\text{-}12)$$

Figs. 3.2-17 and 3.2-18 show the results.

As one can see, when the PLL and ACL bandwidths are made very small with little overshoot, the Eliminator really only affects the spin-frequency noise, and the rest of the signal is virtually untouched.

3.2.1.4 Summary of Basic Principles

The Subtraction Eliminator consists of a PLL and an ACL merged together. It locks onto the fundamental of the largest periodic signal in the input in a given frequency range and subtracts the fundamental out. The signal within ± the smaller of the PLL or ACL bandwidth is also subtracted out. The PLL is able to stay in-lock even if the fundamental is completely subtracted out because the PLL is blind to the signal it subtracts from the input.

3.2.2 Electronics Implementation

This section describes the physical implementation of the Eliminator designed and built by the author. First, the electronics are described, then the method of employment is described.

3.2.2.1 Circuit Components

3.2.2.1.1 Phase Detector

The phase detector is what compares the input phase to the VCO signal phase and produces the error signal in the PLL (see ref. 4). At first, a digital phase detector was tried. The input signals were put

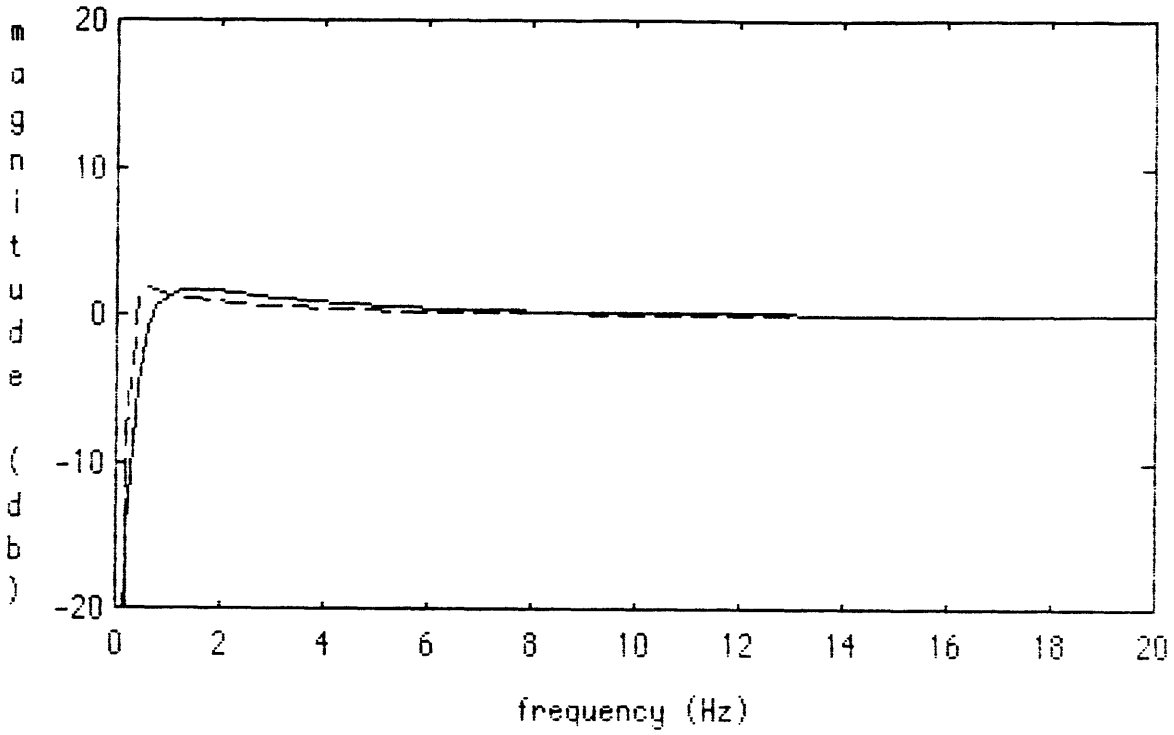

Figure 3.2-17. Closed-loop sensitivity transfer functions for case #5. The solid line is the PLL and the dashed line is the ACL.

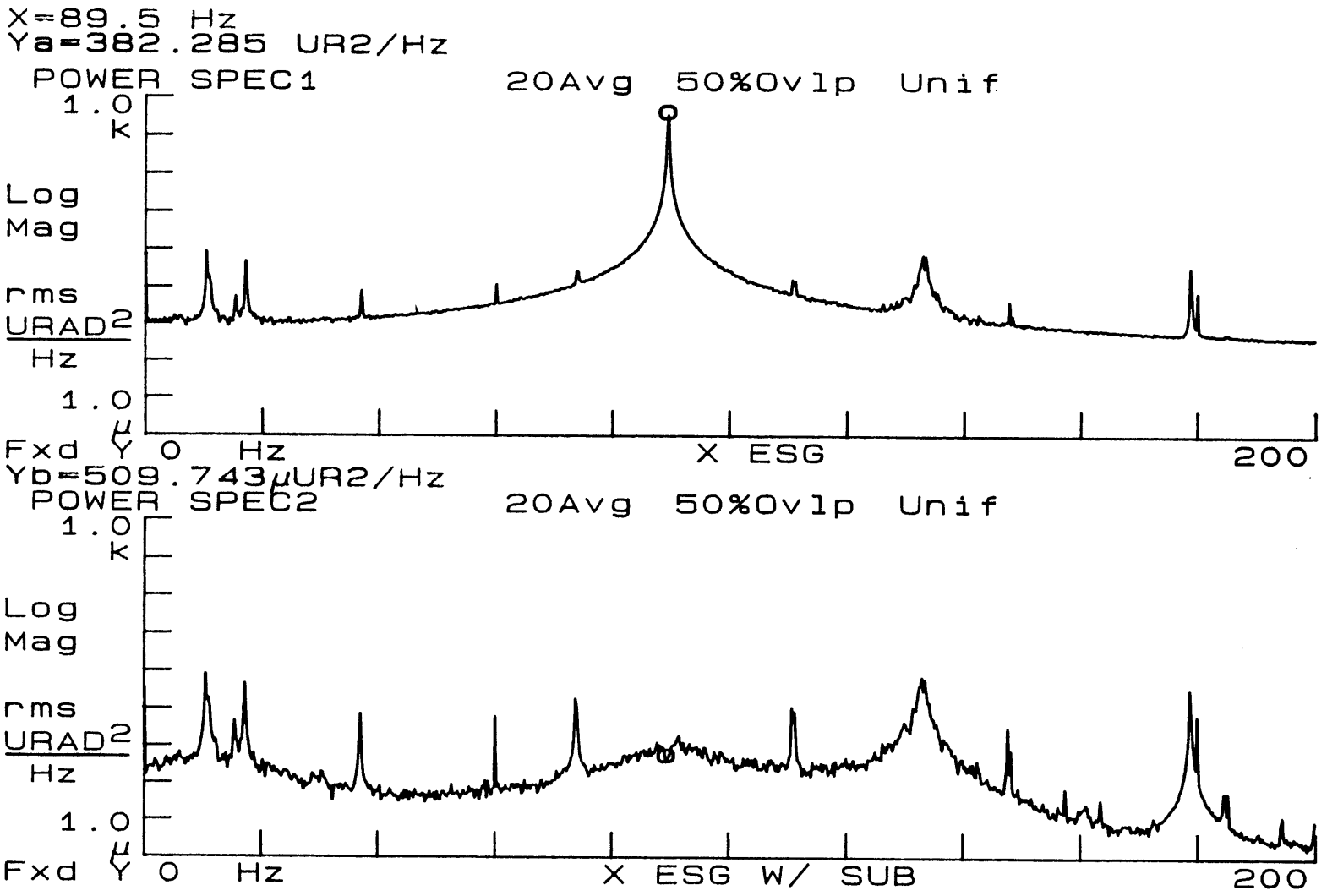

Figure 3.2-18. PSD's of input and output of the Subtraction Eliminator for case #5.

through comparators to turn them into square waves. This method was unsuitable for the Eliminator for two main reasons:

1. The digital detector contained a lot of noise because the comparators had a tough time deciding where the zero-crossings of the inputs were, and
2. the input signals must be allowed to have large low frequency content. This messed up the comparators since with enough DC offset there could be no zero-crossings at all.

An analog multiplier was finally chosen as the phase detector. The Analog Devices 534 chip was used. This chip was also used in the ACL.

3.2.2.1.2 Voltage Controlled Oscillator (VCO)

The VCO produces a periodic signal whose frequency is proportional to the input voltage. For the VCO in the Eliminator, a single period of a sinewave was programmed into a PROM (2716), and a single period of a cosinewave was programmed into another PROM. Each wave consisted of 256 steps and the amplitudes ran from 0 to 255. The output of each PROM was fed into an 8-bit digital-to-analog (D/A) converter (DAC08 chip). The addresses of both PROMs ran to two cascaded LS163 counters. The clock of these counters ran to the VCO output of a 4046 PLL chip. Since each of the PROMs contained 256 steps for one period of the sinewave, the 4046 VCO ran at 256 times the ORG spin speed (256 x 89.4 Hz $\approx$ 23 kHz). The VCO sinewave frequency vs the VCO input voltage for one of the Eliminators is shown in fig. 3.2-19.

The outputs of the D/A's ran to band-pass filters. The band-pass center frequency was set at the ORG spin speed. The band-pass filters served several purposes:

1. They filtered out the DC component of the sinewaves (the DAC08 can only produce voltages from 0 to 5V).

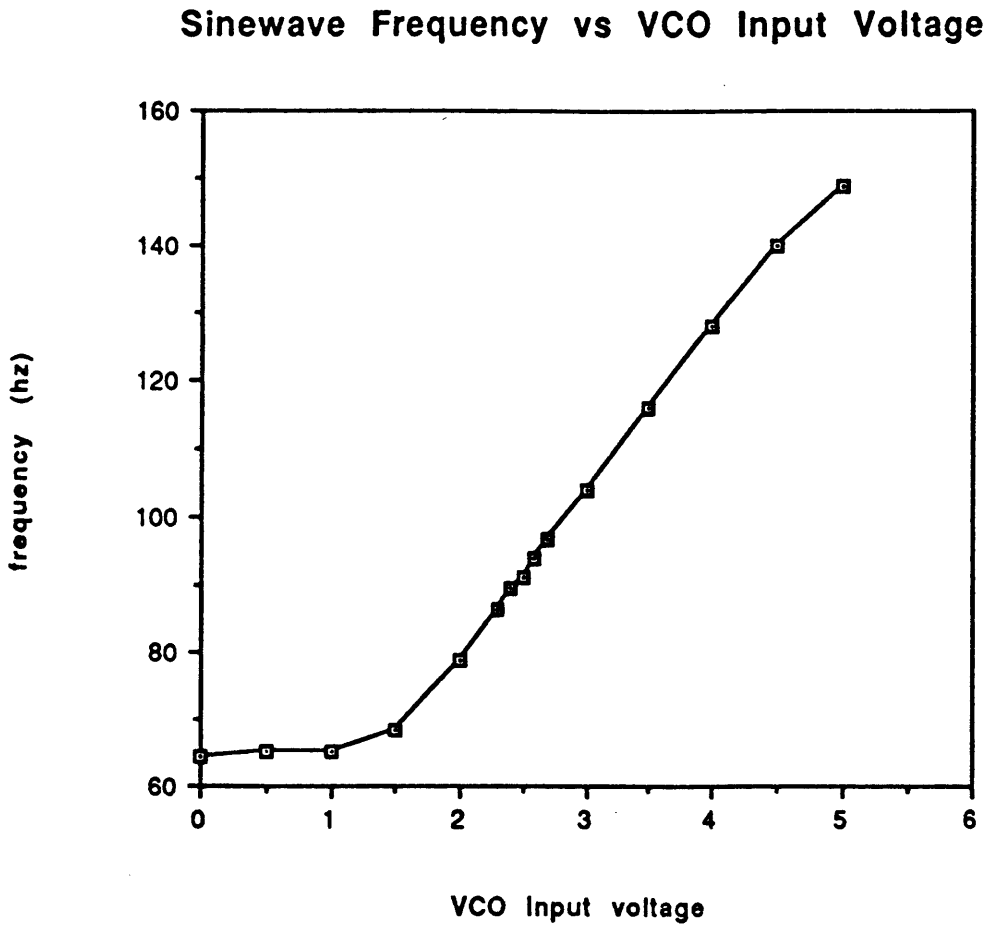

Figure 3.2-19. Plot of VCO frequency vs input voltage for one of the Eliminators.

2. Smoothed out the steps in the sinewaves caused by the PROMs.
3. Allowed fine phase adjustment between the sine and cosinewaves to ensure they were exactly 90° apart.

Also, one of the D/A's served as a multiplier by having the ACL control its reference voltage.

In the dual-axis Torquing Eliminator, described later, a third D/A was added. It took its inputs from the PLL PROM, but its reference voltage was controlled by the ACL.

3.2.2.1.4 Integrators

There are two pure integrators in the Eliminator--one in the PLL and one in the ACL. It was vital that these integrators worked well, since they play a large role in determining how low the amplitude of the discrete-frequency noise can be reduced in the steady-state.

The main difficulty with the integrators was offset voltage. OP77's were used as the op-amps since they have extremely low offset voltages and input bias currents. They are also very stable. But the multipliers (AD534's) that supplied the inputs to the integrators had up to 25 mV of offset voltage. If these offset voltages weren't compensated for, the Eliminator would think it had completely subtracted out the discrete-frequency noise when there would really be a lot left. To compensate for the offsets, a voltage reference was built using two zener diodes. Two potentiometers (pots) were placed across the voltage reference and ran to some voltage dividers which ran to the summing input of the multipliers. By tweaking the pots, one could null out the offset voltages.

3.2.2.2 Circuit Employment

Running the Eliminator consists of three main steps:

1. Locking the PLL
2. Closing the ACL
3. Tuning up the PLL and ACL gains.

Since a multiplier was used as the phase detector in the PLL, the PLL would not lock unless the VCO frequency was very close to the discrete-frequency noise frequency. This is because the multiplier phase detector is only phase sensitive and not frequency sensitive. In order to get the PLL to lock, the subtraction was turned off and the PLL open-loop gain turned up to infinity. Then the gain was turned down and the PLL would lock. The subtraction could then be turned back on. Once the PLL was in-lock, it would stay in-lock.

Once the PLL was in-lock, the ACL was closed. Since the integrators in the ACL were often saturated when the ACL was first closed, it would take a long time for the ACL to start working. To speed it up, the ACL gain was turned up and the ACL integrator offset voltage was increased temporarily until the ACL came out of saturation. Then the gains could be adjusted properly.

Since the D/A was used as the amplitude multiplier, and the D/A used (the DAC08) only works for positive reference voltages, if a negative reference voltage was put in, the D/A would output 0 V. This was a stable state for the ACL, and it would sit there forever. When this happened, a relatively large positive offset voltage was summed into the ACL integrator to bring it out of this state.

3.2.2.3 Summary of Electronics Implementation

An analog multiplier was chosen as the phase detector. PROM's programmed with sine and cosine waveforms together with two LS163 counters and a 4046 PLL chip was chosen as the VCO. Op 77's were chosen as the integrators. A voltage reference had to be created to allow compensation for voltage offsets. To use the Eliminator, the PLL must be closed first and then the ACL closed.

3.2.3 Subtraction Eliminator Performance

This section describes the performance of the Subtraction Eliminator in reducing the discrete-frequency noise in the ORG outputs.

Fig. 3.2-20 shows the PSD's of the x ESG before and after the Subtraction Eliminator. Fig. 3.2-21 show the PSD's of the x OSG before and after the Subtraction Eliminator.

As one can see, the spin frequency (89.4 Hz) noise was reduced by the Eliminator, but virtually none of the rest of the power spectrum was affected. The total power within ±10 Hz of the spin frequency was reduced from 226 to 0.0094 rms μrad^2 in the ESG and from 87.6 to 0.0085 rms μrad^2 in the OSG. This corresponds to a reduction factor of 24,000 in power or 155 in amplitude in the ESG, and 10,300 in power or 102 in amplitude in the OSG.

Actually, these factors of reduction are meaningless. The Eliminator will reduce any amplitude of the discrete-frequency noise (within the saturation limits of the circuit) to the same level. It appears the lowest the discrete-frequency noise can be lowered is the noise level surrounding the discretes (the "noise floor"). Note the discrete-frequency noise must be at least 1 volt peak-to-peak, though, or else the circuit noise will limit the reduction to something higher than the noise floor in the signal.

The Eliminator is remarkably robust. Using a spectrum analyzer, a sinewave was summed into the ESG output while the Eliminator was locked to the spin-speed discrete in the ESG. The added sinewave was then swept in frequency from 80 Hz to 100 Hz. The transfer function of the swept sinusoid to the Eliminator output is shown in fig. 3.2-22. The Eliminator didn't break lock unless the amplitude of the swept sinusoid was about equal to or greater than the amplitude of the spin-speed discrete and the frequency was near the spin

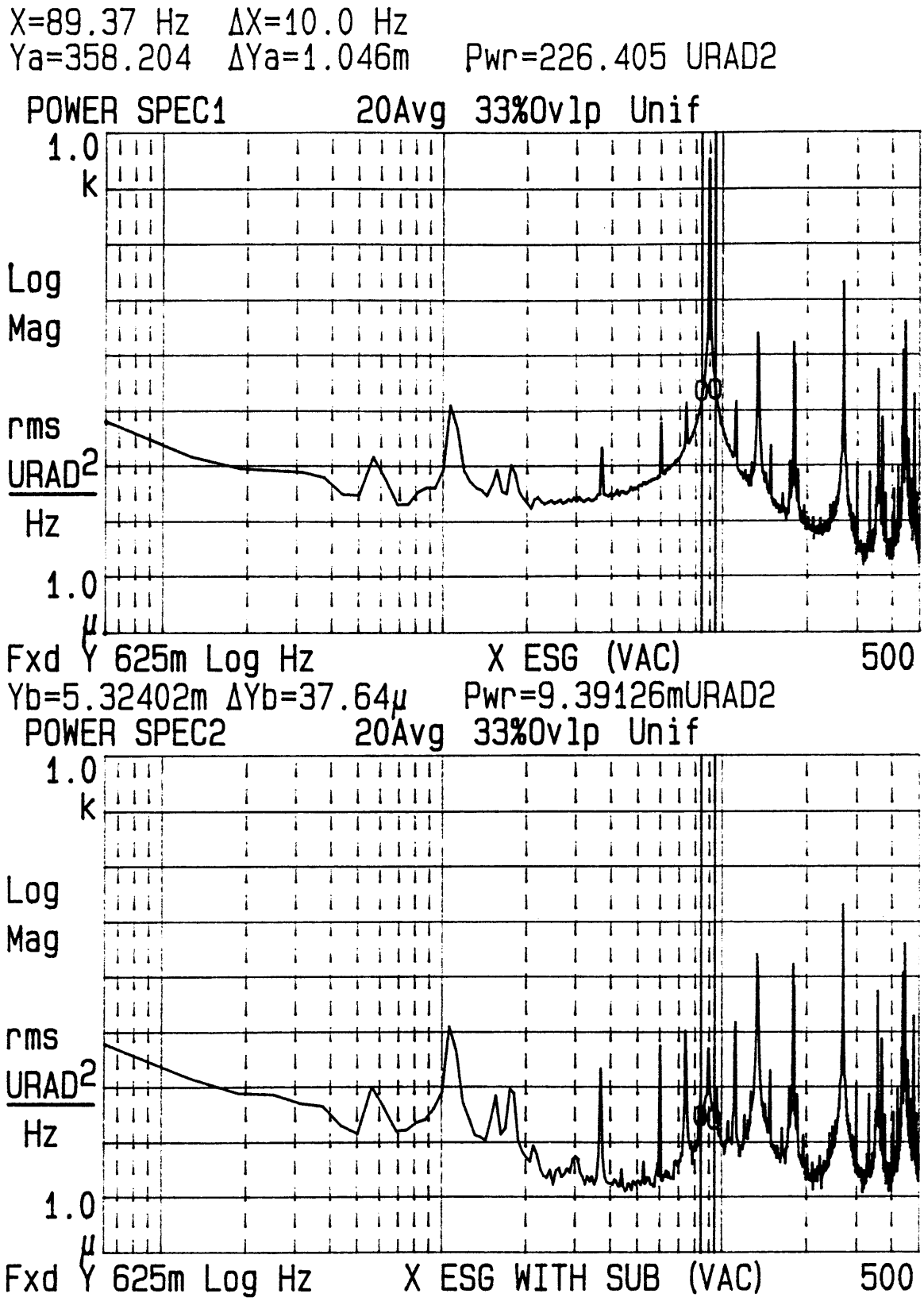

Figure 3.2-20. PSD's of x ESG. Top plot is x ESG output. Bottom plot is output of Subtraction Eliminator.

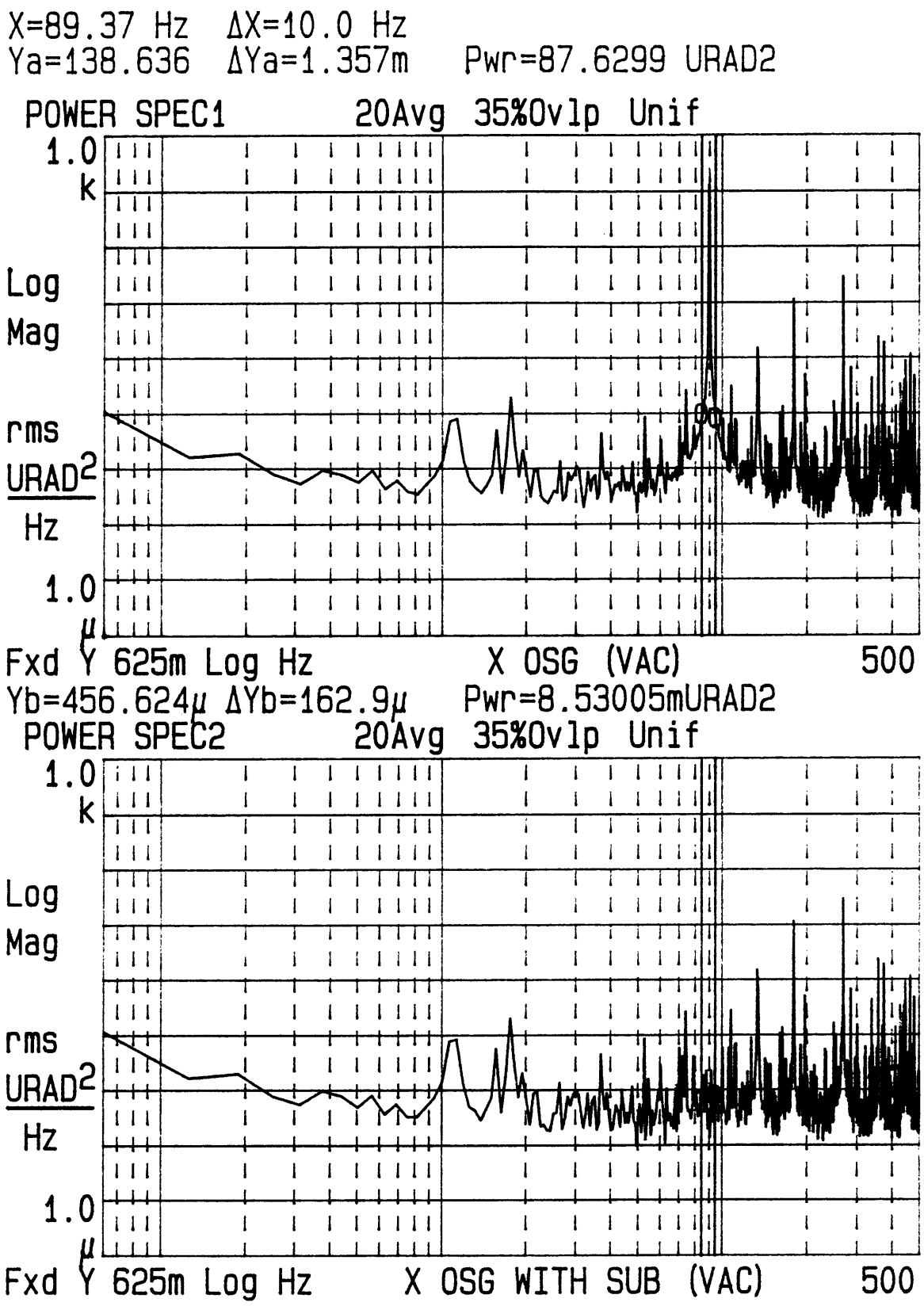

Figure 3.2-21. PSD's of x OSG. Top plot is x OSG output. Bottom plot is output of Subtraction Eliminator.

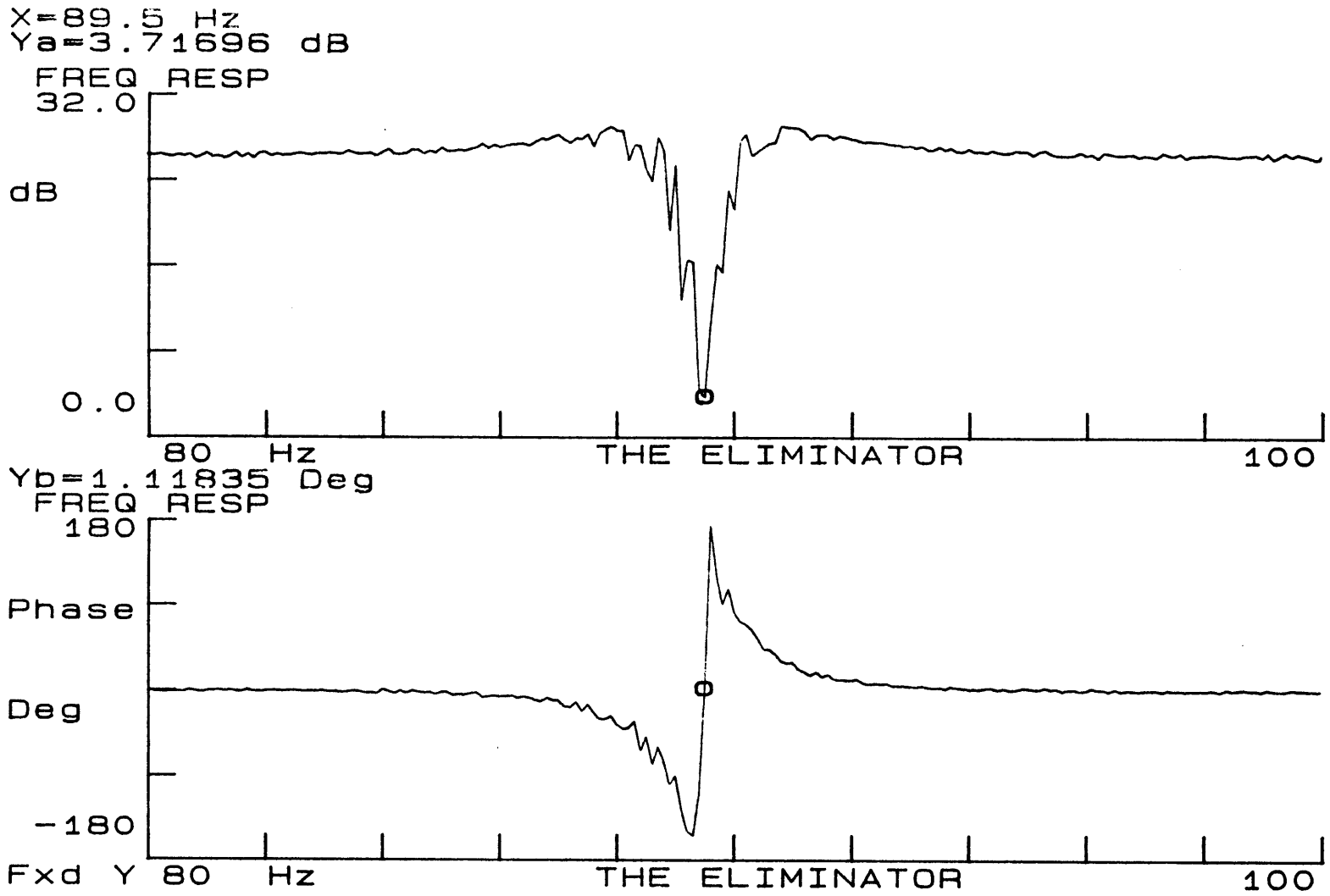

Figure 3.2-22. Transfer function of added signal to Eliminator output.

frequency. In that case, the PLL would start to track the other sinusoid and subsequently get lost.

As one can see, the Eliminator acts as a sort of notch filter. It will not only eliminate the spin-speed discrete noise, but also signal that occurs at the spin speed.

Another test was performed. The platform the ORG was on was dithered back and forth as in the isolation transfer function measurements (see section 4.1), and the transfer function of table movement to the x ESG while the Subtraction Eliminator was on was taken as the dither was swept in frequency (see fig. 3.2-23). The ESG saw the table motion at all frequencies except near the ORG spin-speed.

In summary, the Subtraction Eliminator can reduce the spin-frequency noise in both the ESG and OSG to the noise surrounding the spin-frequency noise. Also, the Subtraction Eliminator acts as a sort of notch filter and reduces signal as well as noise at the spin frequency.

3.3 Discrete-Frequency Noise Compensation #2--Torquing Eliminator

The Subtraction Eliminator electronically subtracted the spin-frequency discrete from the ORG output. This section describes a method that applies a physical torque to the rotor to remove the spin-frequency discrete in both the x- and y-axes simultaneously.

First, the basic principles of the Torquing Eliminator are described, and then the performance of the Torquing Eliminator is presented.

3.3.1 Basic Principles

The Torquing Eliminator moves the rotor in such a way so the x and y outputs no longer contain sinusoids at the spin frequency. Basically,

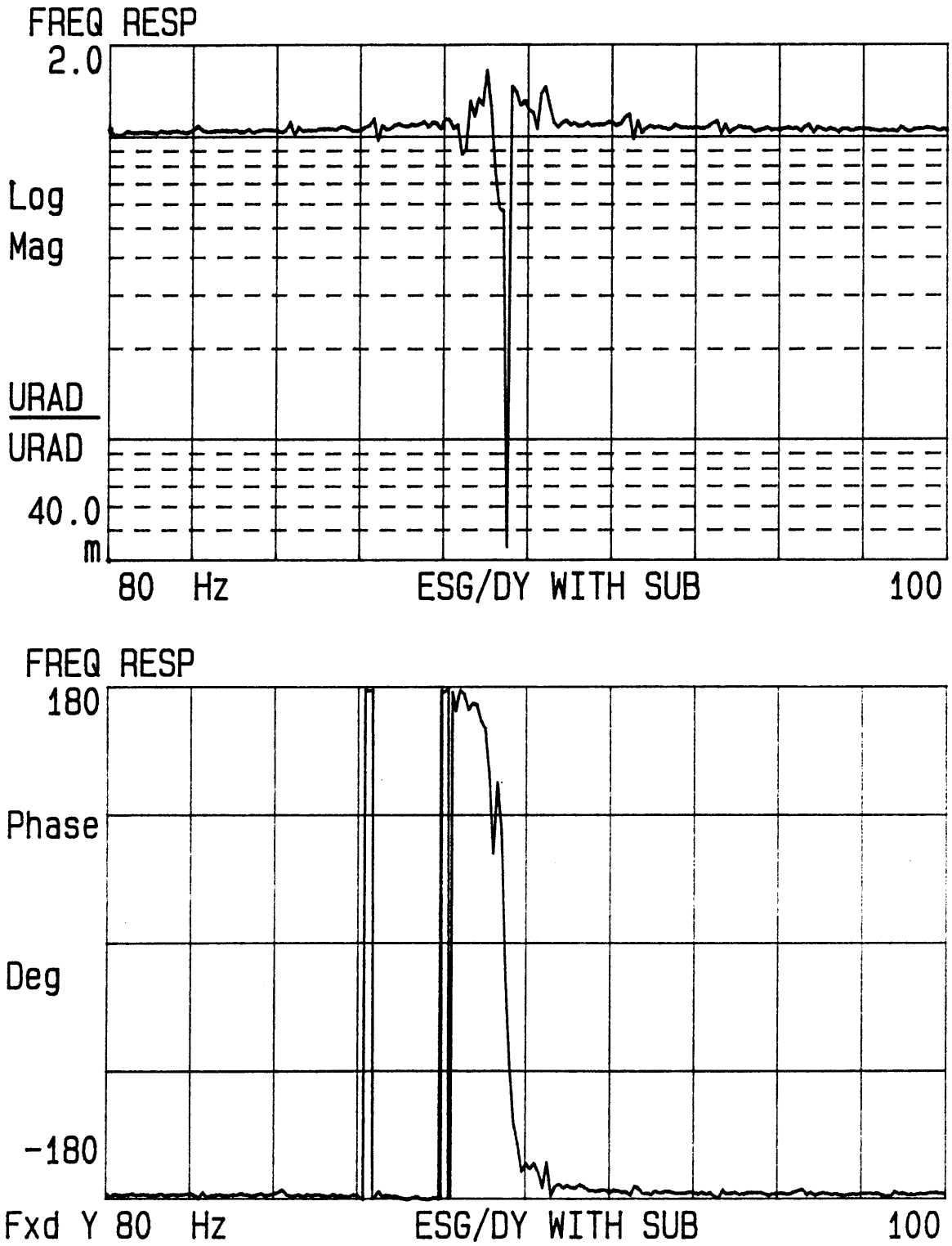

Figure 3.2-23. Transfer function of platform movement to ESG with the Subtraction Eliminator.

a phase-locked loop and amplitude-control loop are used similar to the subtraction case, except instead of electronically subtracting the sinusoid, the sinusoid is fed into the ORG torquer. This torquer has coils that can apply torques to the ORG rotor, and the torquer acts as the subtracter.

First, a Torquing Eliminator that removes the spin-frequency noise in one axis is described, and then a Torquing Eliminator that can remove the spin-frequency noise in both axes simultaneously is described.

3.3.1.1 Single-Axis Torquing Eliminator

In the Torquing Eliminator, the gyro acts as the subtracter. The Torquing Eliminator gets its input from either the ESG or OSG and sends its output to one of the ORG torquers, M_x or M_y (see fig. 3.3-1). If the input is θ_x, the output must be hooked up to M_x; and if the input is θ_y, the output must be hooked up to M_y.

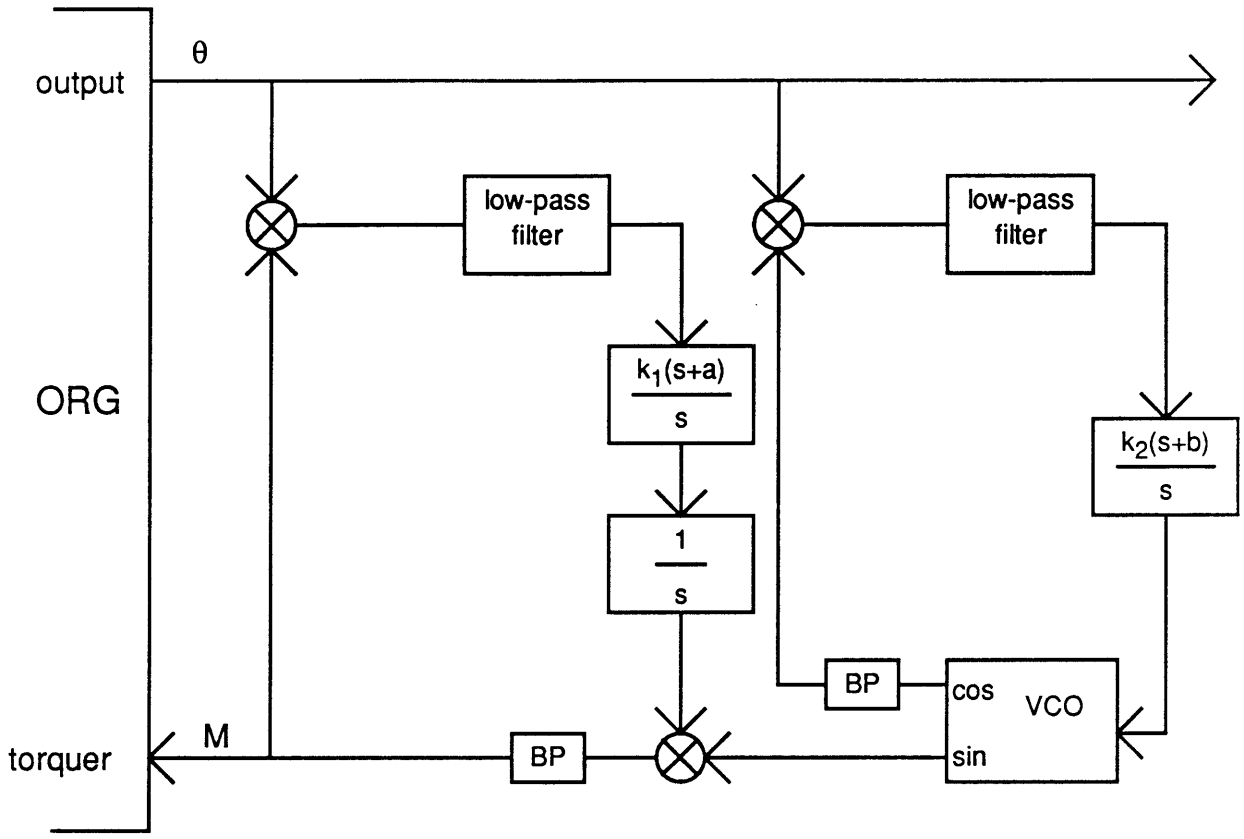

Figure 3.3-1. Block diagram of single-axis Torquing Eliminator. Note: "BP" stands for band-pass filter.

If there is no phase lag between the signal which goes into the torquer and the gyro output, the Torquing Eliminator behaves exactly like the Subtraction Eliminator. This is because the ORG acts as the subtracter. But if there is a phase lag, the Torquing Eliminator will still work properly. This is shown in the following analysis.

There are two places a phase lag can occur in the gyro. The first is a phase lag in the torquer-to-angle transfer function θ/M, i.e. the rotor does not follow the command instantaneously.

Let the output of the gyro be (see fig. 3.3-2)

$$O(t) + A_n \sin(\omega t),$$

where O(t) is the desired signal and $A_n\sin(\omega t)$ is the discrete-frequency noise.

Let the value of the transfer function of the gyro from the torquer to the output, at the frequency ω, be

$$\theta(j\omega)/M(j\omega) = Ge^{-j\phi_T}, \qquad (3\text{-}13)$$

i.e. the gyro has a gain of G and phase lag of ϕ_T at frequency ω. Thus if the signal fed to the torquer by the Eliminator is

$$A_aA_p\sin(\omega t+\phi)$$

the output of the gyro will be

$$O(t) + A_n\sin(\omega t) - A_aA_pG\sin(\omega t+\phi-\phi_T).$$

This means the input to the PLL low-pass filter is

$$[O(t) + A_n\sin(\omega t) - A_aA_pG\sin(\omega t+\phi-\phi_T)]A_p\cos(\omega t+\phi),$$

which can be rewritten as

$$O(t)A_p\cos(\omega t+\phi) + 0.5A_nA_p\sin(2\omega t+\phi) + 0.5A_nA_p\sin(-\phi) - 0.5A_aA_p^2G\sin(2\omega t+2\phi-\phi_T) - 0.5A_aA_p^2G\sin(-\phi_T).$$

After the low-pass filter, this signal can be approximated by taking only its DC component:

$$0.5A_p[-A_n\sin(\phi) + A_aA_pG\sin(\phi_T)].$$

Before taking this calculation any further, the ACL will be analyzed.

The input to the ACL low-pass filter is

$$[O(t) + A_n\sin(\omega t) - A_aA_pG\sin(\omega t+\phi-\phi_T)]A_aA_p\sin(\omega t+\phi),$$

which can be rewritten as

$$O(t)A_aA_p\sin(\omega t+\phi) + 0.5A_nA_aA_p\cos(\phi) -$$
$$0.5A_nA_aA_p\cos(2\omega t+\phi) - 0.5A_a^2A_p^2G\cos(\phi_T) +$$
$$0.5A_a^2A_p^2G\cos(2\omega t+2\phi-\phi_T).$$

After the low-pass filter, this signal can be approximated by taking only its DC component:

$$0.5A_aA_p[A_n\cos(\phi) - A_aA_pG\cos(\phi_T)].$$

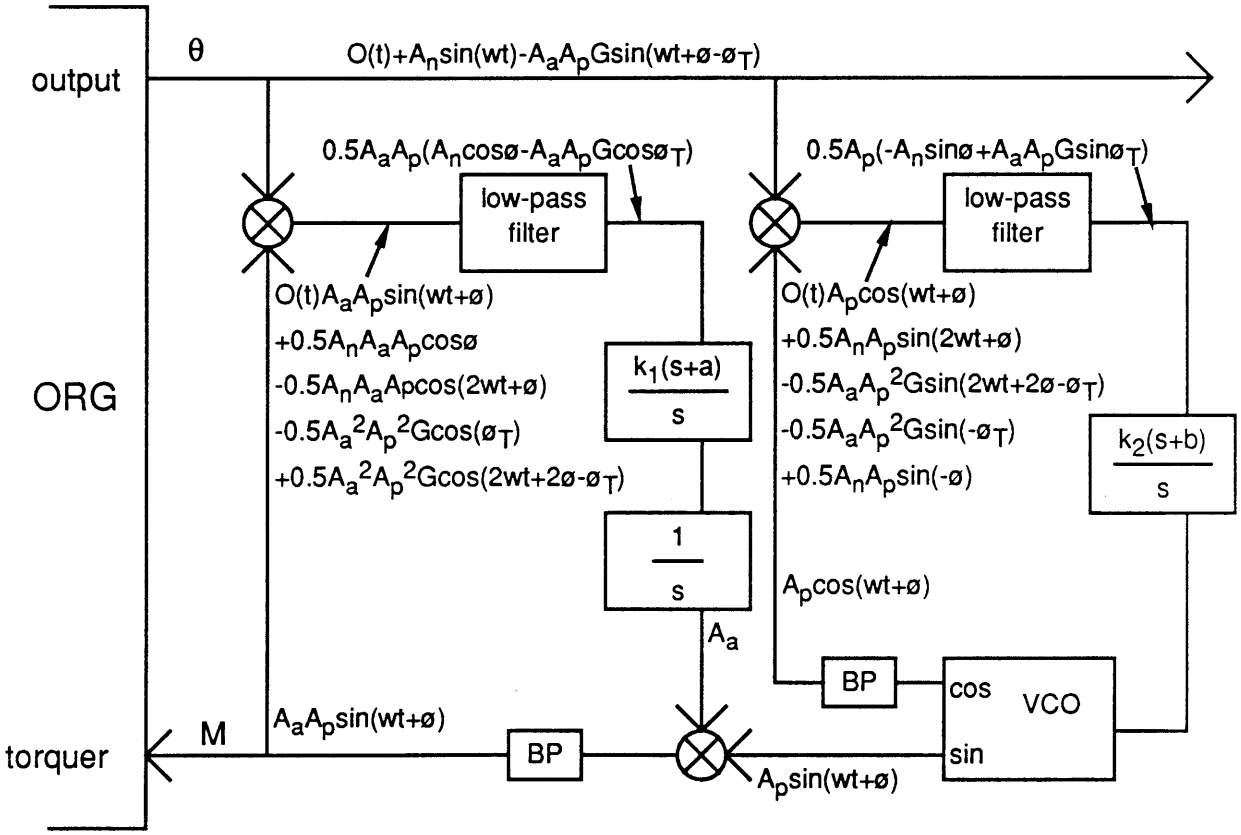

Figure 3.3-2. Single-axis Torquing Eliminator with labelled signals.

The PLL and ACL want to drive the outputs of their low-pass filters to zero. In order to make

$$0.5A_p[-A_n\sin(\phi) + A_aA_pG\sin(\phi_T)] = 0 \qquad (3\text{-}14)$$

and

$$0.5A_aA_p[A_n\cos(\phi) - A_aA_pG\cos(\phi_T)] = 0, \qquad (3\text{-}15)$$

the only non-trivial solution (the trivial solution is Aa = ø = 0) is

$$\phi = \phi_T \qquad (3\text{-}16)$$

and

$$A_a = A_n/(A_pG). \qquad (3\text{-}17)$$

This results in a gyro output signal

$$O(t) + A_n\sin(\omega t) - [A_n/(A_pG)]A_pG\sin(\omega t+\phi_T-\phi_T),$$

which equals

$$O(t),$$

which is the desired signal.

Thus the Torquing Eliminator can compensate for gain and phase in the gyro torque-to-angle transfer function θ/M.

The other type of phase lag is a phase lag in the measurement of the gyro output (a filter on the output, for example).

Let the phase lag in the measurement at the frequency ω be $-\phi_m$. Thus, the gyro output is

$$O(t) + A_n\sin(\omega t-\phi_m) - A_aA_p\sin(\omega t+\phi-\phi_m),$$

where O(t) is the desired signal (already filtered), $A_n\sin(\omega t)$ is the discrete-frequency noise, and $A_aA_p\sin(\omega t+\phi)$ is the signal fed into the torquer by the Eliminator.

The input to the PLL low-pass is

$$[O(t) + A_n\sin(\omega t-\phi_m) - A_aA_p\sin(\omega t+\phi-\phi_m)]A_p\cos(\omega t+\phi),$$

which can be rewritten as

$$O(t)A_p\cos(\omega t+\phi) + 0.5A_nA_p\sin(2\omega t+\phi-\phi_m) + 0.5A_nA_p\sin(-\phi_m-\phi) - 0.5A_aA_p^2\sin(2\omega t+2\phi-\phi_m) - 0.5A_aA_p^2\sin(-\phi_m).$$

After the low-pass, this becomes

$$0.5A_p[-A_n\sin(\phi+\phi_m) + A_aA_p\sin(\phi_m)].$$

The input to the ACL low-pass is

$$[O(t) + A_n\sin(\omega t-\phi_m) - A_aA_p\sin(\omega t+\phi-\phi_m)]A_aA_p\sin(\omega t+\phi),$$

which can be rewritten as

$$O(t)A_aA_p\sin(\omega t+\phi) + 0.5A_nA_aA_p\cos(-\phi_m-\phi) - 0.5A_nA_aA_p\cos(2\omega t-\phi_m+\phi) - 0.5A_a^2A_p^2\cos(-\phi_m) + 0.5A_a^2A_p^2\cos(2\omega t+2\phi-\phi_m).$$

After the low-pass this becomes

$$0.5A_aA_p[A_n\cos(\phi_m+\phi) - A_aA_p\cos(\phi_m)].$$

The PLL and ACL will try to drive the outputs of their low pass filters to zero. Thus,

$$0.5A_p[-A_n\sin(\phi+\phi_m) + A_aA_p\sin(\phi_m)] = 0 \qquad (3\text{-}18)$$

and

$$0.5A_aA_p[A_n\cos(\phi+\phi_m) - A_aA_p\cos(\phi_m)] = 0. \qquad (3\text{-}19)$$

If ϕ_m is small, the non-trivial solution is

$$\phi = 0 \qquad (3\text{-}20)$$

and

$$A_a=A_n/A_p. \qquad (3\text{-}21)$$

This will result in a gyro output of

$$O(t) + A_n\sin(\omega t-\phi_m) - (A_n/A_p)A_p\sin(\omega t+0-\phi_m)$$

which equals

$$O(t)$$

which is the desired result. If ϕ_m is not small, however, the discrete-frequency noise is not exactly subtracted out.

Thus the Torquing Eliminator will work properly if there is a phase lag in the measurement, provided the phase lag is small.

As stated earlier, if there is no phase lag through the torquer or phase lag in the measurement, the Torquing Eliminator dynamics are exactly the same as those of the Subtraction Eliminator. If there are phase lags, the dynamics become more complicated because of the new dependence of the PLL on the ACL. The dynamics of the Torquing Eliminator are not analyzed in this thesis, but it is probably safe to assume they are very similar to the dynamics of the Subtraction Eliminator, and the data obtained tends to confirm this.

3.3.1.2 Dual-Axis Torquing Eliminator

But the above scheme works only for a single axis. When a second Eliminator was hooked up to the other axis, neither Eliminator would work properly. When the PLL's of the two Eliminators were first closed, and before the signal to the torquers were hooked up and the ACL's closed, the Eliminator signals (the signals that would go into the torquers) were 90° apart. They were 90° apart because the discrete-frequency noise in the two axes were 90° apart. After the torquers were hooked up, the phase between the two Eliminator signals drifted until they were about 45° apart and stayed there.

The reason for this apparent change in behavior is the cross-coupling of the gyro axes. If torque is put into one axis of a gyro, the gyro rotor will move about both axes. As one Eliminator would try to reduce the discrete-frequency noise in its axis, it would cause sinusoids to appear in both axes. The second Eliminator would try to reduce the discrete-frequency noise in its axis as well the sinusoid added to its axis by the first Eliminator. If the PLL in one Eliminator were to drift a little in phase, the other would see the change in its axis and would shift a little in phase as it followed it. This in turn would cause the phase of the first PLL to drift even more. Eventually the PLL's find contentment at an undesirable equilibrium point.

To solve this problem, the plant dynamics were decoupled. In other words, the rotor was torqued in such a way so each Eliminator affected only the axis it was measuring.

In the dual-axis torquing configuration (see fig. 3.3-3), two Eliminators are used. The first Eliminator has θ_x as its input, and the second has θ_y. Each Eliminator has two outputs--a sinusoid in phase with the sinusoid locked onto by the PLL and a sinusoid 90° out of phase. These sinusoids are generated by the two VCO outputs. Both sinusoids are amplitude modulated by the ACL output. All four of the outputs from the two Eliminators are then combined and sent to the torquers M_x and M_y.

The torquers M_x and M_y have certain effects on θ_x and θ_y. At the spin frequency, the ORG has the following values of the transfer functions (neglecting small phase lags):

$$\theta_x/M_x(j\omega_s) = K_C e^{+j\pi/2} \qquad (3\text{-}22)$$

$$\theta_x/M_y(j\omega_s) = K_T \qquad (3\text{-}23)$$

$$\theta_y/M_x(j\omega_s) = K_C e^{-j\pi/2} \qquad (3\text{-}24)$$

$$\theta_y/M_y(j\omega_s) = K_T. \qquad (3\text{-}25)$$

To see how the dual-axis Torquing Eliminator works, first, let $A\sin\omega_s t$ and $B\cos\omega_s t$ represent the spin-frequency noise that is "added" to the ORG outputs θ_x and θ_y respectively. The spin-frequency noises in the x- and y-axes don't have to be 90° apart for this method to work, but this assumption simplifies the analysis.

Now assume the PLL's in the Eliminators are locked onto the spin-frequency noise. This means the Eliminator which measures θ_x is outputting $\alpha\cos\omega_s t$ and $\alpha\sin\omega_s t$, and the other Eliminator is outputting $\beta\cos\omega_s t$ and $-\beta\sin\omega_s t$. α and β are the amplitudes of the sinewaves as determined by the ACL's.

Two of the sinusoids are then multiplied by the ratio of the magnitude of the direct-axis and cross-axis θ/M transfer functions at the spin-frequency. The sinusoids are then combined as shown in fig. 3.3-3. Thus,

$$M_x = \alpha\cos\omega_s t + \beta K_T/K_C\cos\omega_s t, \qquad (3\text{-}26)$$

and

$$M_y = -\beta\sin\omega_s t + \alpha K_T/K_C\sin\omega_s t. \qquad (3\text{-}27)$$

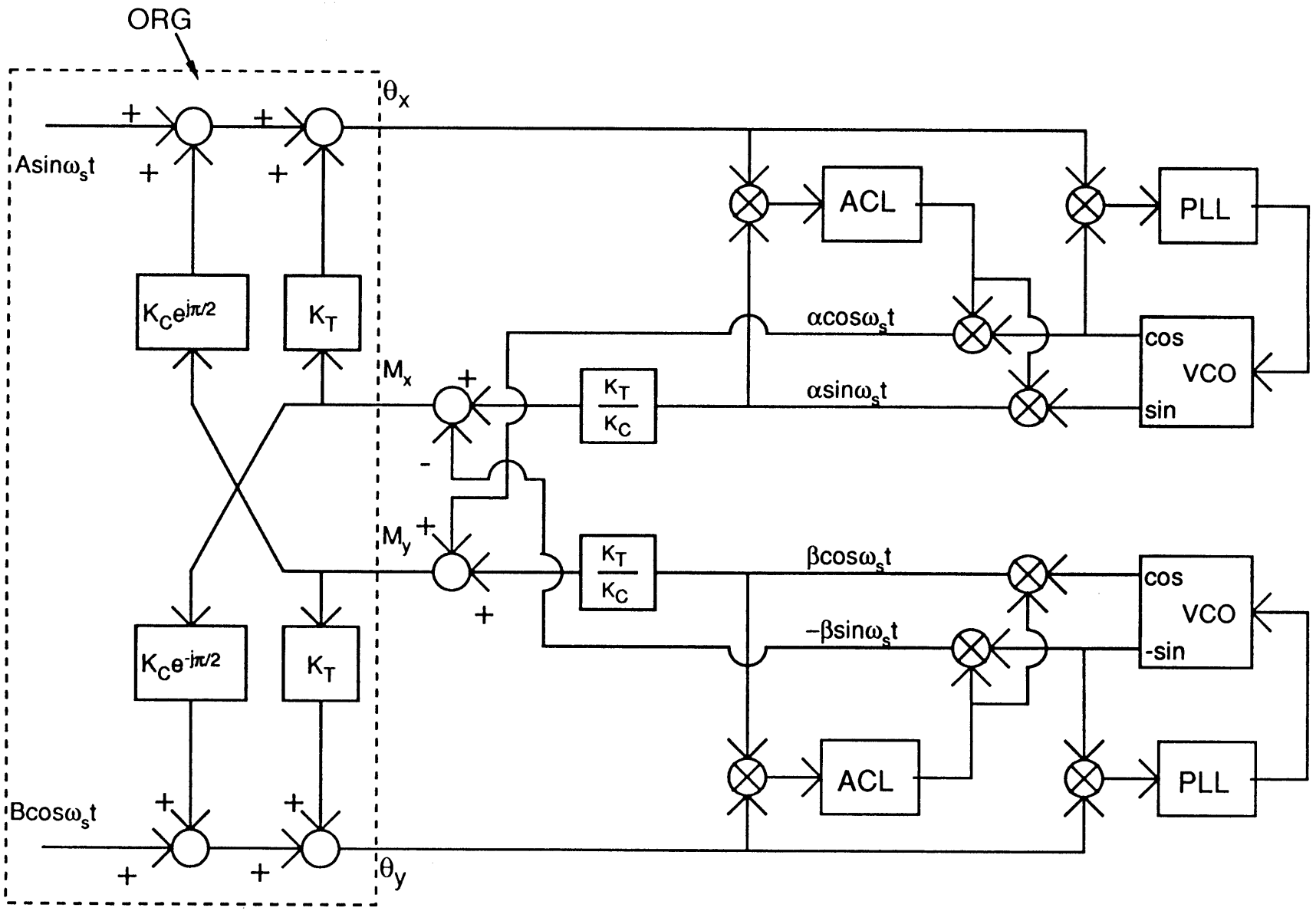

Figure 3.3-3. Block diagram of dual-axis Torquing Eliminator.

Using the θ/M transfer functions at the spin frequency shown earlier and using the expressions for M_x and M_y just obtained, one finds

$$\theta_x = A\sin\omega_s t - \alpha K_C \sin\omega_s t - \beta K_T \sin\omega_s t + \alpha K_T^2/K_C \sin\omega_s t + \beta K_T \sin\omega_s t, \quad (3\text{-}28)$$

and

$$\theta_y = B\cos\omega_s t - \beta K_C \cos\omega_s t - \alpha K_T \cos\omega_s t + \beta K_T^2/K_C \cos\omega_s t + \alpha K_T \cos\omega_s t. \quad (3\text{-}29)$$

These can be rewritten as

$$\theta_x = (A - \alpha K_C + \alpha K_T^2/K_C)\sin\omega_s t, \quad (3\text{-}30)$$

and

$$\theta_y = (B - \beta K_C + \beta K_T^2/K_C)\sin\omega_s t. \quad (3\text{-}31)$$

Thus each Eliminator affects only the axis it is measuring.

The ACL's will try to drive the spin-frequency component of θ to zero. This means

$$A - \alpha K_C + \alpha K_T^2/K_C = 0, \quad (3\text{-}32)$$

and

$$B - \beta K_C + \beta K_T^2/K_C = 0. \quad (3\text{-}33)$$

So α and β will be driven towards the following:

$$\alpha = AK_C/(K_C^2 - K_T^2) \quad (3\text{-}34)$$

and

$$\beta = BK_C/(K_C^2 - K_T^2). \quad (3\text{-}35)$$

For the ORG with gas at 6 μm of Hg (a near vacuum) inside,

$$K_T \approx 2.8\ \mu\text{rad/V},$$

and

$$K_C \approx 4.9\ \mu rad/V$$

(see figs. 2.1-6 through 2.1-9).

Therefore,

$$\alpha \approx (0.3\ V/\mu rad)A,$$

and

$$\beta \approx (0.3\ V/\mu rad)B.$$

There are a few remarks to be made about the dual-axis Torquing Eliminator:

- By having each Eliminator feed torque into M_x and M_y in a certain way, the gyro dynamics can be decoupled, and each Eliminator will affect only one axis.
- The above scheme was derived using the idea that in torquing both M_x and M_y in opposite directions, on one axis the movements could exactly cancel, and on the other there could be some residual movement. In this way, only one axis would be affected.
- Once the gyro dynamics have been decoupled, each Eliminator acts as a single-axis Torquing Eliminator. Except in this case, instead of G being K_T or K_C, G is now $K_C/(K_C^2-K_T^2)$. This implies that any phase lag through the torquer or measuring system will still automatically be compensated for by the Eliminator.
- Even though the analysis was done for the spin-frequency noises in θ_x and θ_y 90° out of phase, the dual-axis Torquing Eliminator will work for any phase relation between the discrete-frequency noises.
- The above scheme will work for discrete-frequency noises at other frequencies than the spin frequency as long as the direct-axis and cross-axis θ/M transfer functions at the particular frequency have different magnitudes and a 90° phase difference. This criterion is met for all frequencies except those within about ±30 Hz of the nutation frequency (133 Hz). The large resonance at 133 Hz distorts the amplitude and phase near it.

• It is very interesting to note the tuning of the KT/KC gains in the Eliminator did not have to be very precise. The KT/KC gains could be changed significantly, and the change in performance was unnoticeable. It is currently unknown why this is so.

3.3.1.3 Summary of Torquing Eliminator Basic Principles

There are two types of Torquing Eliminator--the single-axis and dual-axis. The dual-axis Torquing Eliminator contains cross-axis coupling compensation. The Torquing Eliminator can compensate for phase lag and gain change in the ORG torquer and/or the signal generator. The Torquing Eliminator behaves nearly exactly like the Subtraction Eliminator.

3.3.2 Torquing Eliminator Performance

Fig. 3.3-4 shows the ESG outputs with no Eliminator. Fig. 3.3-5 shows the ESG outputs after the two-axis Torquing Eliminator has been hooked up to the ESG outputs.

Fig. 3.3-6 shows the OSG outputs with no Eliminator. Fig. 3.3-7 shows the OSG outputs after the two-axis Torquing Eliminator has been hooked up to the OSG outputs.

For the ESG, the reduction of power ±10 Hz around the spin frequency is from 217 to 0.0077 rms μrad^2 for the x-axis and from 323 to 0.013 rms μrad^2 for the y-axis. This corresponds to reduction factors of 28,200 and 24,800 in power or 168 and 158 in amplitude.

For the OSG, the reduction of power ±10 Hz around the spin frequency is from 15 to 0.0099 rms μrad^2 for the x-axis and from 3.3 to 0.0085 rms μrad^2 for the y-axis. This corresponds to reduction factors of 1,500 and 388 in power or 39 and 20 in amplitude.

Similar to the subtraction Eliminator, these reduction factors actually are meaningless, since the Eliminator will reduce the

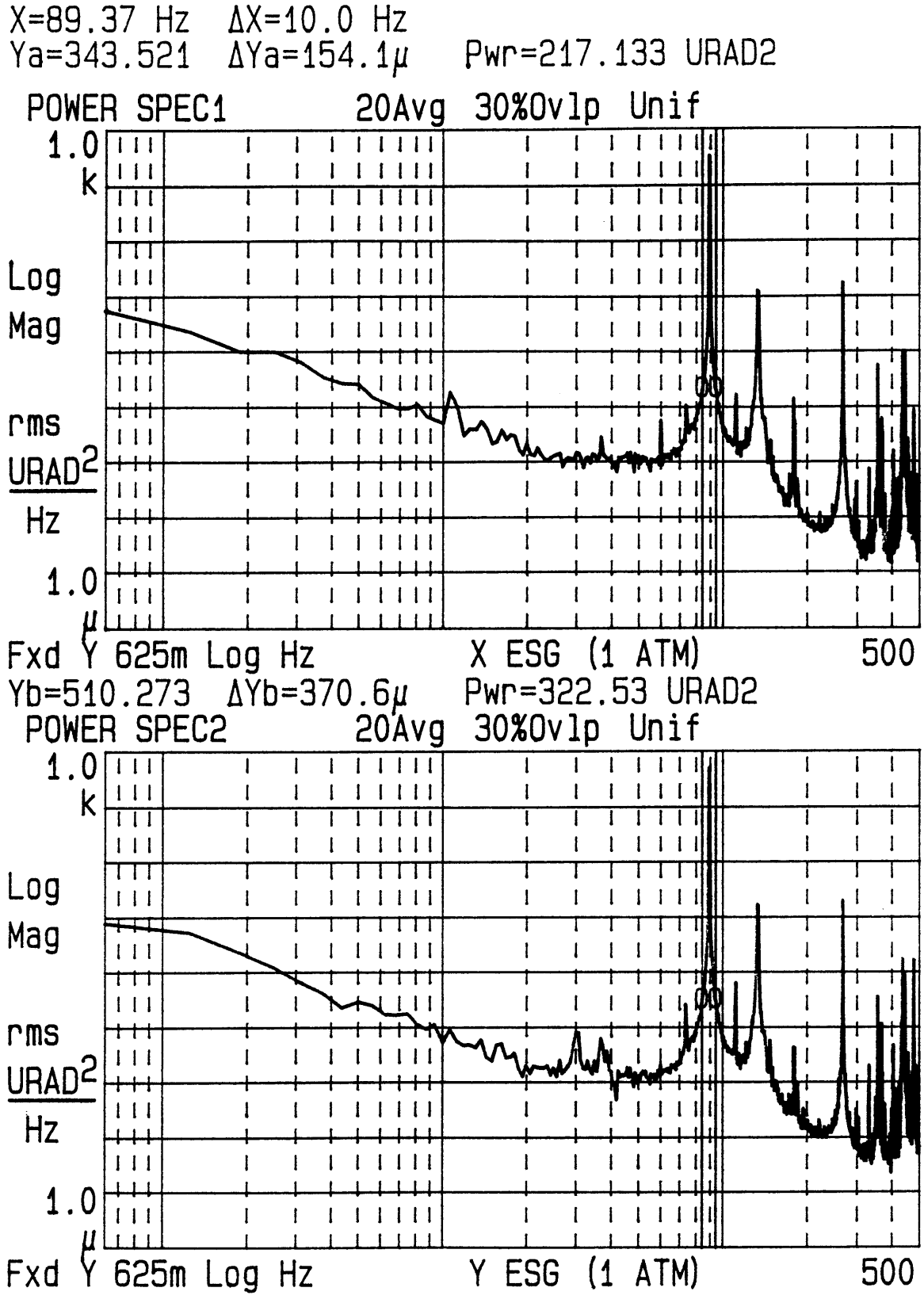

Figure 3.3-4. PSD's of x ESG and y ESG with no Eliminator.

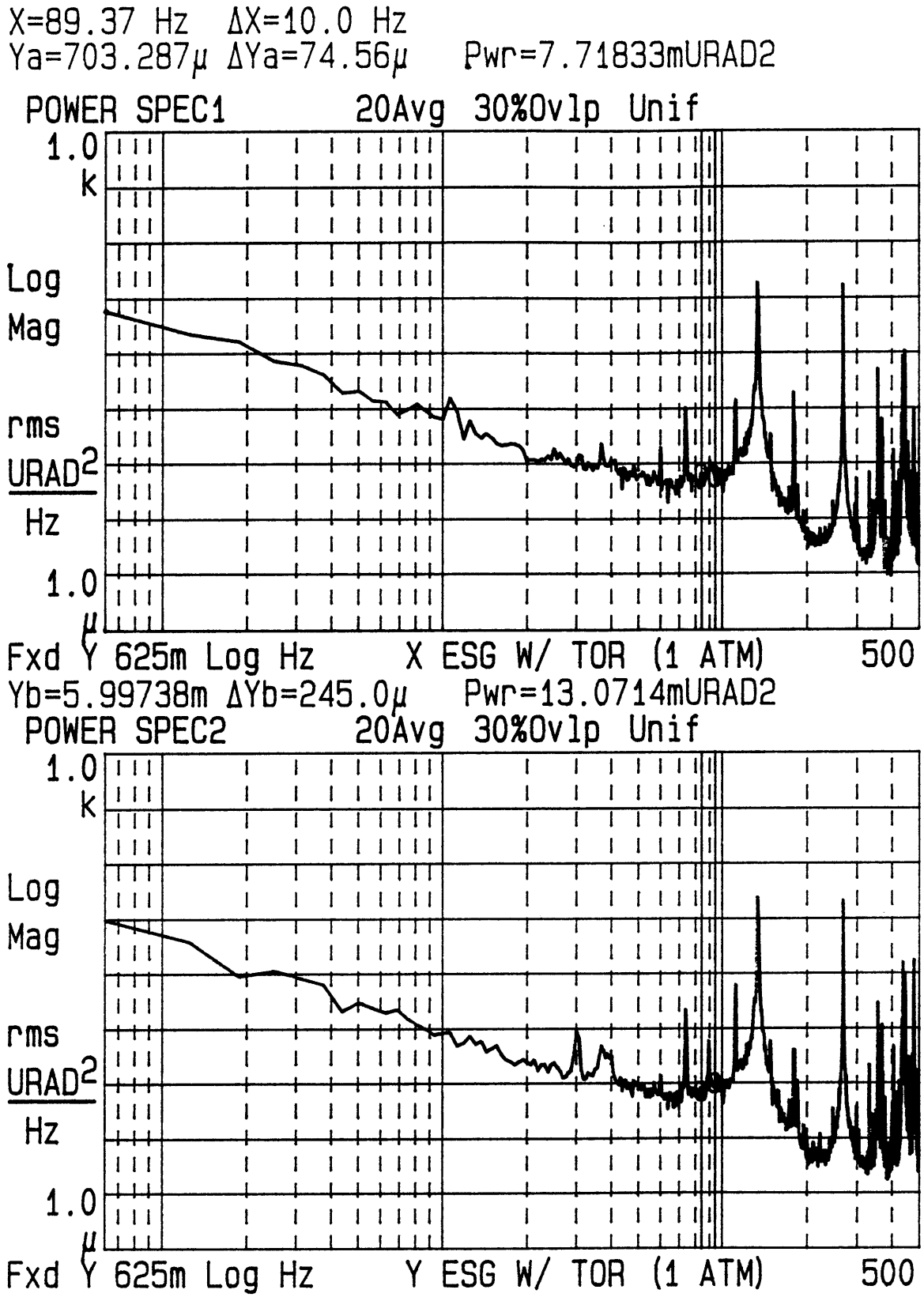

Figure 3.3-5. PSD's of x ESG and y ESG with two-axis Torquing Eliminator hooked up to ESG.

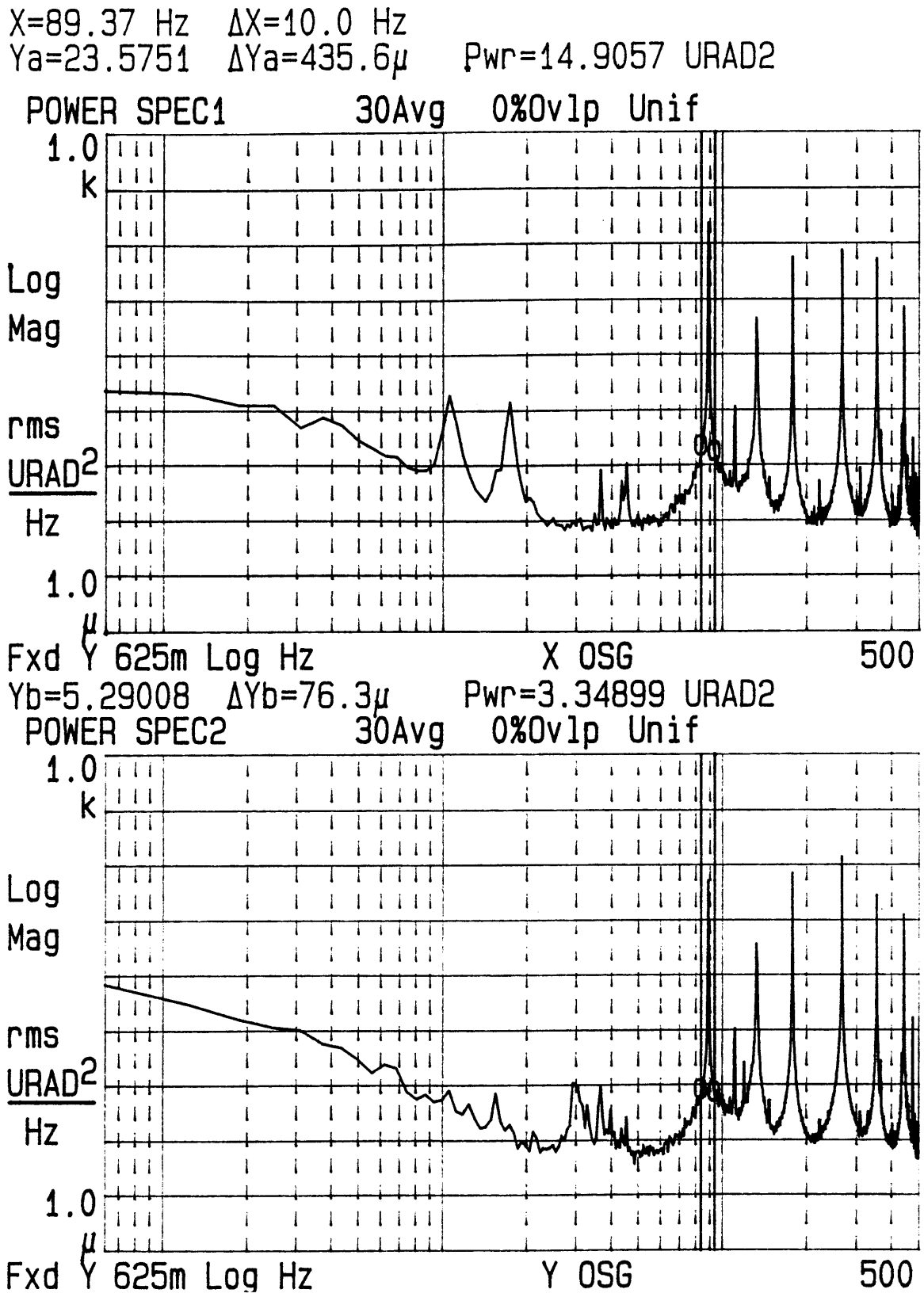

Figure 3.3-6. PSD's of x OSG and y OSG with no Eliminator.

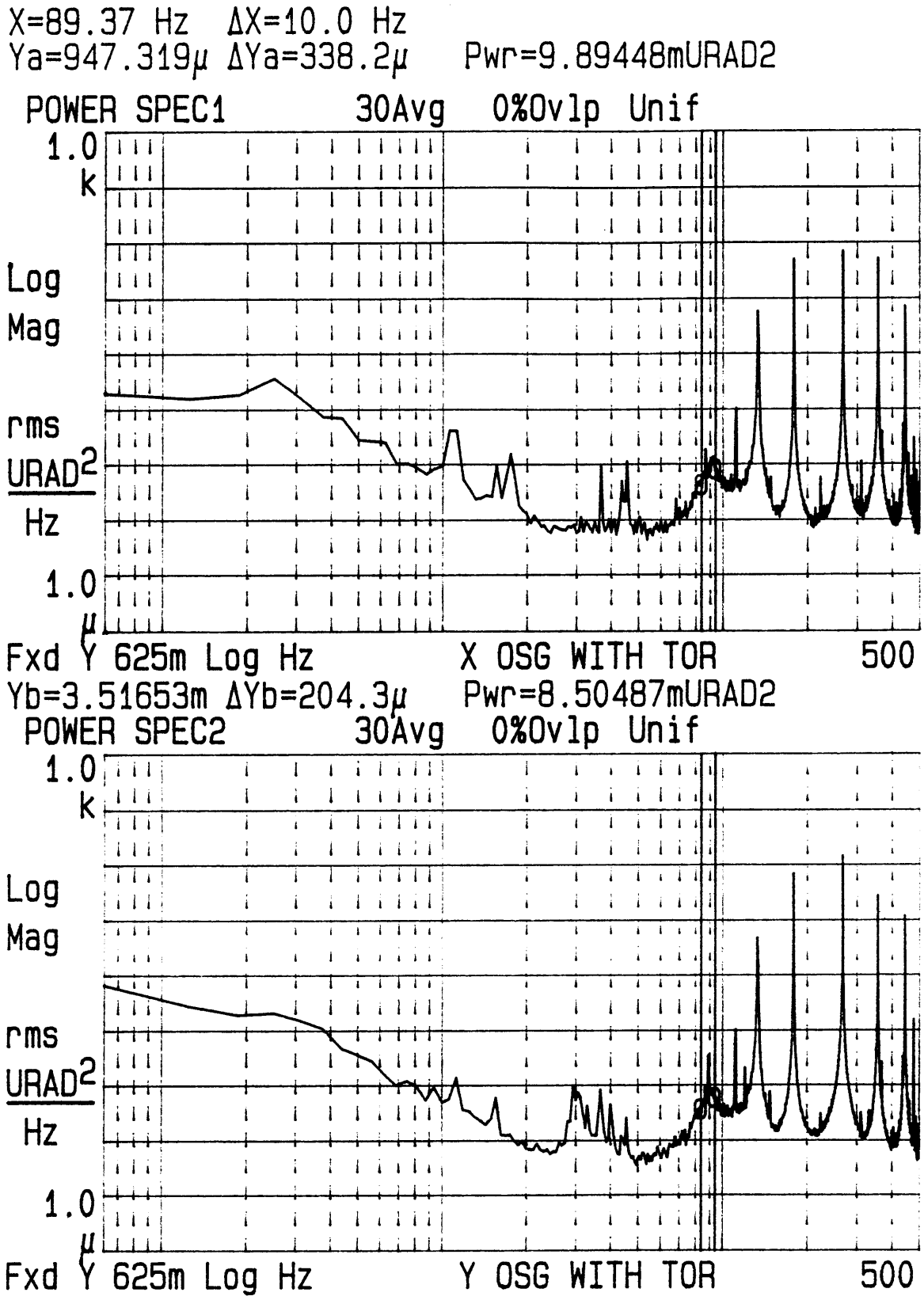

Figure 3.3-7. PSD's of x OSG and y OSG with two-axis Torquing Eliminator hooked up to OSG.

discrete-frequency noise to the level of the noise surrounding the discrete, regardless of the discrete-frequency noise amplitude. Once again, though, the discrete-frequency noise must be at least 1 V peak-to-peak, or else circuit noise will be a factor.

Unfortunately, torquing out the fundamental hardly reduced the harmonics. At most, some of the harmonics were reduced by about 15%. The harmonics were not expected to be reduced anyway, since the rotor is torqued with pure sinusoids.

The Torquing Eliminator seemed just as robust as the Subtraction Eliminator. As with the Subtraction Eliminator, the platform the ORG was on was dithered and the transfer function of platform movement to ESG with the two-axis Torquing Eliminator was measured. Figs. 3.3-8 and 3.3-9 show the transfer function.

Note that when the Torquing Eliminator brought the spin-frequency discrete to zero in the OSG, the spin-frequency discrete got worse in the ESG, and vice-versa. This is because the OSG and ESG null axes are not the same and the natural spin axis lies relatively close to the OSG and ESG null axes. In other words, by just moving the rotor, it is impossible to have the ESG and OSG spin-frequency discretes reduced to zero at the same time.

Also note that torquing the rotor does not affect the platform vibration noticeably. An angular displacement sensor (ADS) measuring the platform movement could detect no change in gyro-emitted vibration with and without two-axis Eliminator torquing.

In summary, the Torquing Eliminator can reduce the spin-frequency noise to the level of the surrounding noise without affecting the rest of the signal.

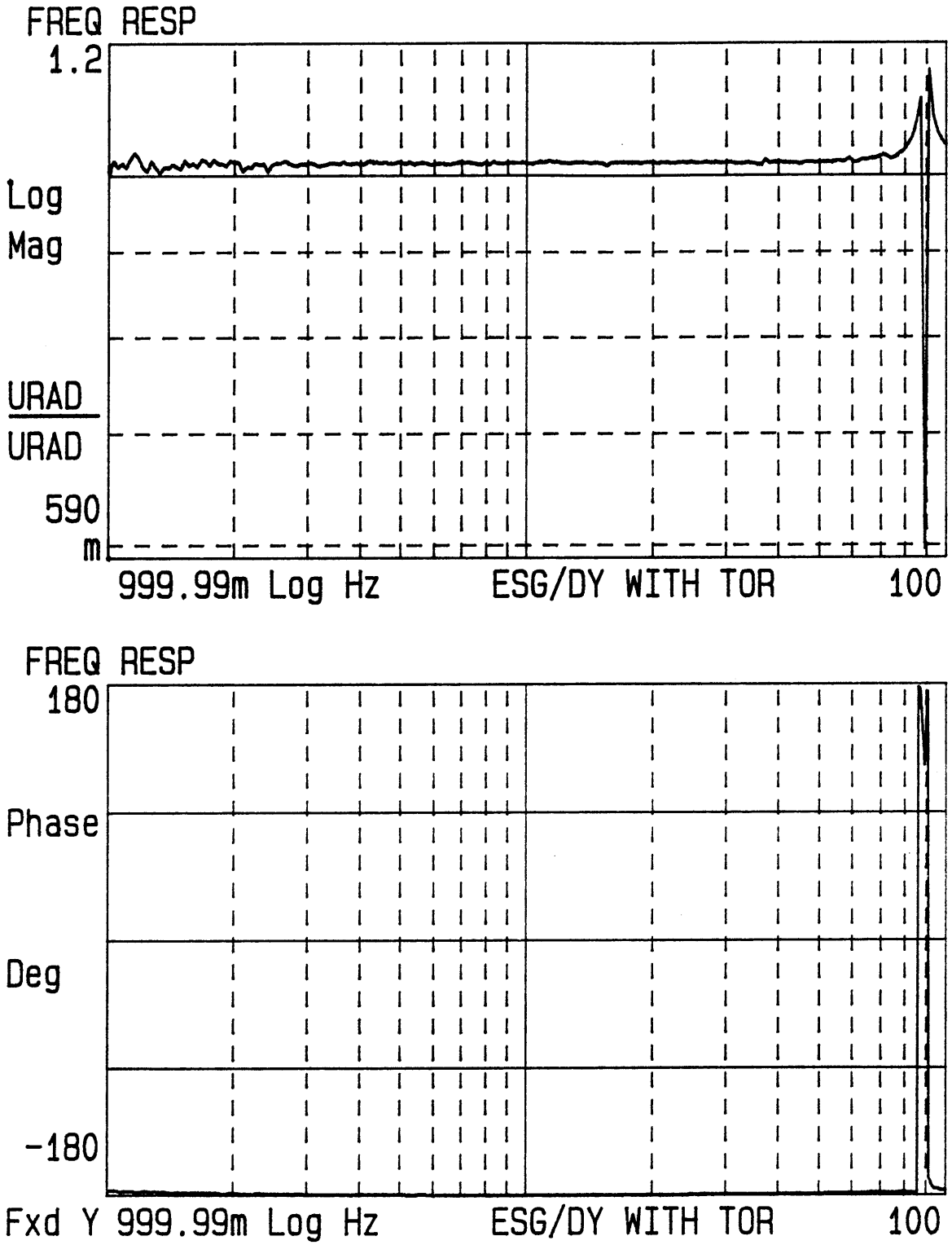

Figure 3.3-8. Transfer function of ESG to platform movement with two-axis Torquing Eliminator hooked up. 1-100 Hz.

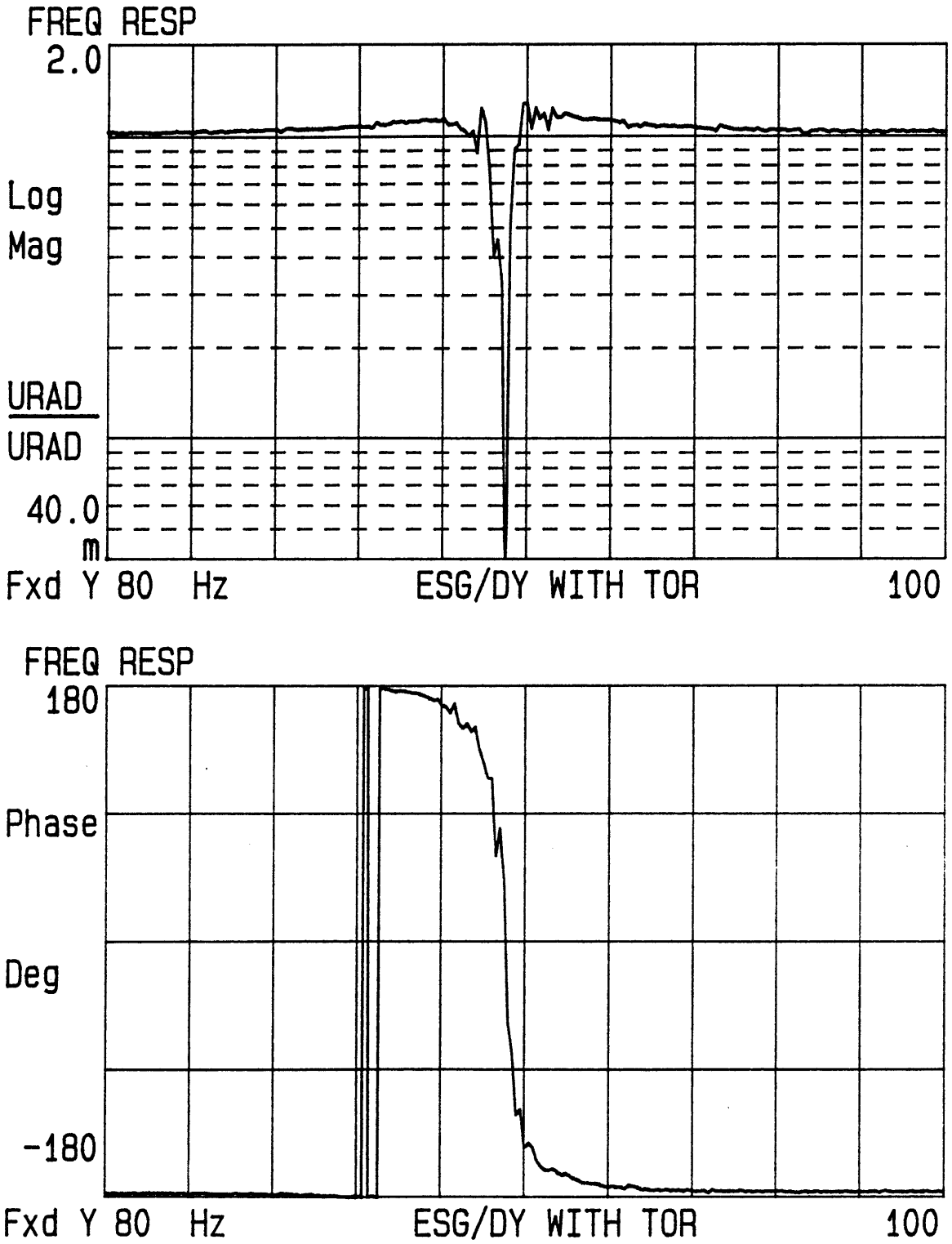

Figure 3.3-9. Transfer function of ESG to platform movement with two-axis Torquing Eliminator hooked up. 80-100 Hz.

3.4 Summary of Discrete-Frequency Noise Compensation

The discrete-frequency noise compensation, the Eliminator, is basically a notch filter. It will attenuate signals near the spin frequency as well as the noise. The Eliminator can be made into a very narrow notch so that the signal is virtually unaffected outside ~±1 Hz of the spin frequency. And this notch filter, unlike conventional notch filters, will move to follow the spin frequency.

The Eliminator was able to reduce the spin-frequency noise to the basic noise floor of the instrument. It was able to do this by either electronically subtracting the noise from the output or torquing the rotor so as to exactly cancel the noise. It could remove the noise from either the ESG or the OSG, although it could not remove the noise from the ESG and OSG simultaneously by torquing the rotor. The performances of the Subtraction Eliminator and the Torquing Eliminator were nearly exactly the same.

4 ORG Performance Study

This section investigates the performance of the ORG beam as a pseudo-star. First, an experiment is described in which the coupling of the ORG case to the ORG rotor was measured. In this experiment, the ORG was placed on a turnable platform. The platform was rotated back and forth a small amount (about 50 μrad), and the inertial stability of the ORG beam was measured. Then the results are presented and compared with model simulations, and the sources of the rotor-to-case coupling are investigated.

4.1 Experiment Setup

For the performance study, the ORG was placed on a turnable platform (see figs. 4.1-1 and 4.1-2). The platform was a Goertz test table, model 500 (M-52). The ORG was placed with its pinhole as close to the center of the table as possible. The ORG rotor spin axis was placed along a north-south line to minimize the earth rate the

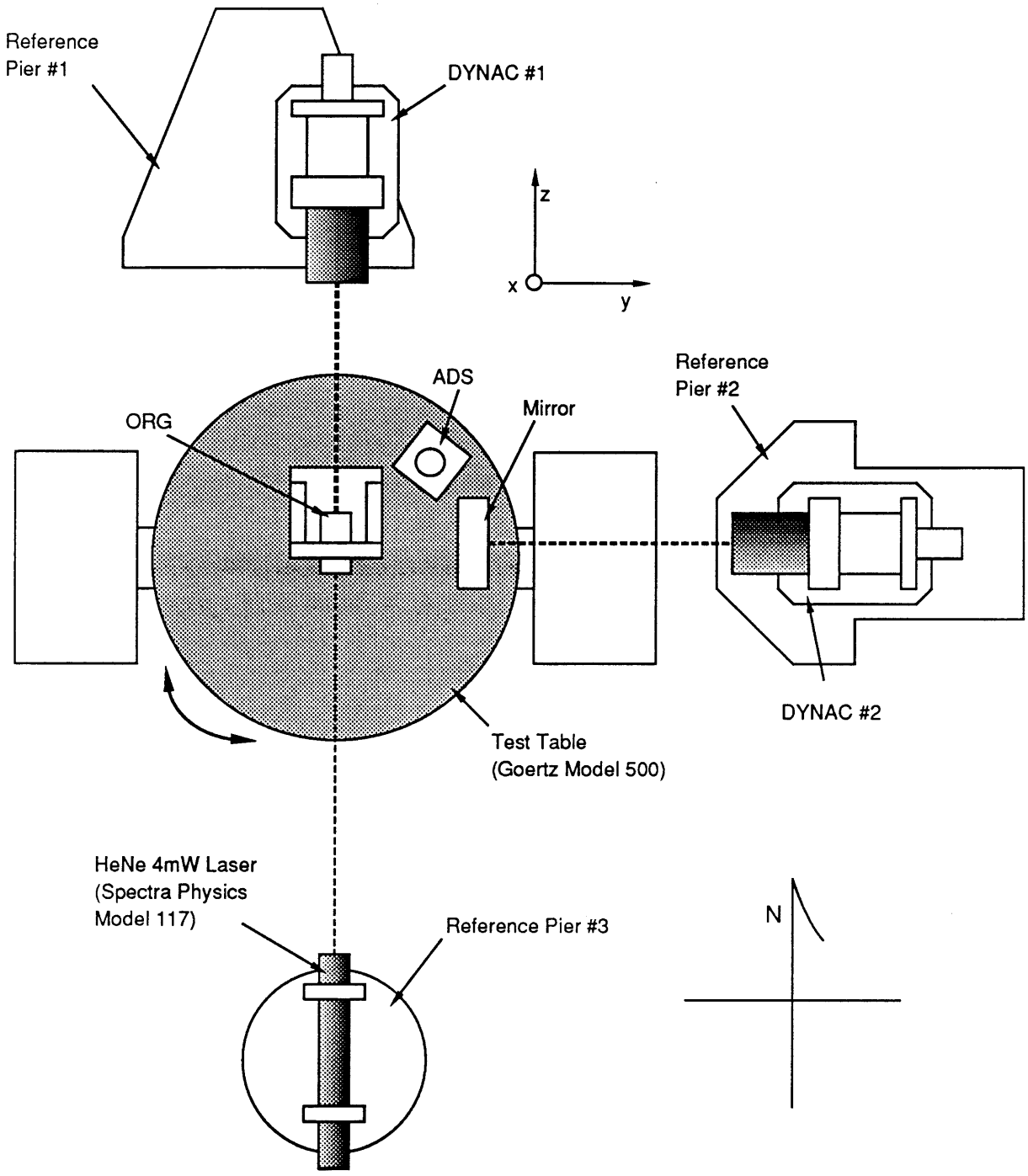

Figure 4.1-1. Diagram of isolation performance experiment.

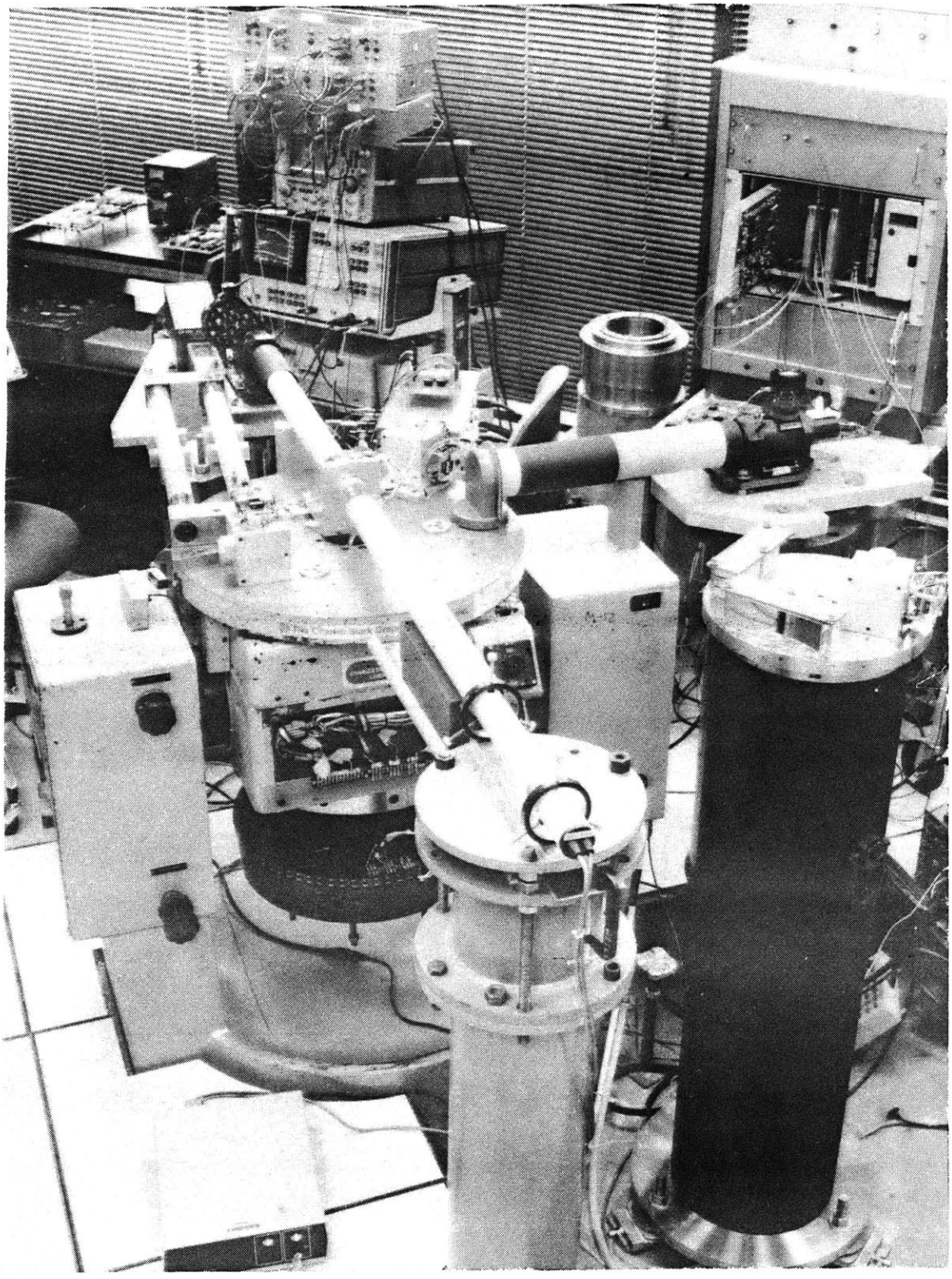

Figure 4.1-2. Photograph of isolation performance experiment.

ORG experienced.

The light source, a 4 mW HeNe laser, was placed on a stationary reference pier. The laser was positioned so as to illuminate the ORG pinhole. The laser was angled slightly so the reflection from the back of the rotor would not go back inside the laser. The polarization of the laser was placed in the vertical direction, so the DYNAC would have the greatest sensitivity in azimuth measurement. The laser head was 27" from the pinhole.

DYNAC #1 was placed on a second stationary reference pier on the other side of the ORG. It was aligned so the ORG beam went down the center of the DYNAC. The DYNAC was also aligned so azimuth and elevation measurements were both at null when the ORG rotor was at null and the table position was such that DYNAC #2 was at null. An intensity normalizer (see section 2.2.2.2) was placed on the DYNAC #1 outputs to minimize the effects of pinhole movement across the laser beam.

DYNAC #2 was placed on a third stationary reference pier perpendicular to the ORG spin axis. This DYNAC contained its own light source. It sent the light out through its optics, off a mirror mounted on the table, and back into its optics. This DYNAC measured the rotation of the table.

Cardboard tubes were placed around all the beams to cut down the noise caused by air. Even a small gap in the air protection increased the noise in the OSG measurements significantly.

Placed on the test table, along with the ORG and DYNAC #2 mirror, was an angular displacement sensor (ADS). Its sensitive axis was placed parallel to the test-table axis. The ADS was used because its scale factor was known and could be used to calibrate the ORG and DYNAC measurements. Table 4-1 summarizes what each instrument measured.

Instrument	What It Measures
DYNAC #1 (az.)	rotor-to-inertia angle about x-axis (OSG x) (θ_x)
DYNAC #1 (el.)	rotor-to-inertia angle about y-axis (OSG y) (θ_y)
DYNAC #2 (az.)	case-to-inertia angle about x-axis (θ_{Cx})
ADS	case-to-inertia angle about x-axis (θ_{Cx}>2 Hz)
ESG x	rotor-to-case angle about x-axis ($\theta_{Cx}-\theta_x$)
ESG y	rotor-to-case angle about y-axis ($\theta_{Cy}-\theta_y$)

Table 4-1. Instruments used in the ORG performance study.

The tests were performed as follows:

First, DYNAC #2, the ESG, and the OSG were calibrated. A sinewave generated by a Hewlett Packard frequency synthesizer was fed into the test table torquer. This caused the table to rotate back and forth. The sinewave was then swept in frequency. The DYNAC #2 over ADS transfer function was measured. Since the ADS scale factor was known, this gave the DYNAC #2 scale factor. Then a tight torque-rebalance loop was closed on the ORG rotor (to make the rotor move with the case), and the OSG (i.e. DYNAC #1) over DYNAC #2 transfer function was measured. This gave the OSG scale factor. Then the ORG torque-rebalance loop was opened, and the ESG over DYNAC #2 transfer function was measured. This gave the ESG scale factor.

To measure the isolation transfer function, $\theta_x(j\omega)/\theta_{Cx}(j\omega)$, again the table was dithered with a frequency-sweeping sinewave. The table movement was kept to around ±50 μrad, although sometimes it was as high ±75 μrad in order to get a reasonable signal-to-noise ratio in the OSG transfer function measurements. The isolation transfer function was obtained by measuring the DYNAC #1 over DYNAC #2 transfer function.

To measure the cross-axis isolation transfer function, $\theta_y(j\omega)/\theta_{Cx}(j\omega)$, the table was dithered as before. This time DYNAC

#1 was rotated 90° so as to measure elevation. Again, the transfer function was obtained by measuring the DYNAC #1 over DYNAC #2 transfer function.

At higher frequencies, the OSG signal was very small. To increase the signal-to-noise ratio, the Subtraction Eliminator was used on the OSG.

The measurements were taken with various amounts of gas inside the ORG. When the ORG was first received, it was filled with Helium (He) at approximately 2 psi. Later, the ORG seal was opened, and tests were run with air at 1 atmosphere. Finally, a cryogenic vacuum pump was attached to the ORG, and tests were run with the gas pressure in the ORG as low as 6 μm of mercury, a near vacuum.

In summary, the ORG was placed on a platform that rotated back and forth, and the transfer function of the movement of the ORG rotor to the ORG case was measured.

4.2 ORG Case Disturbance Attenuation

This section presents and analyzes the results of the above mentioned experiment.

4.2.1 Isolation Transfer Function

There wouldn't be an isolation transfer function if there weren't extraneous torques on the rotor due to gas, spring-restraints, etc. In other words, in an ideal two-degree-of-freedom gyro the rotor angle with respect to inertia would be completely independent of case angle with respect to inertia. But regrettably, the ORG is not an ideal gyro, and a non-zero isolation transfer function was measured.

At first, it was thought the motion detected by DYNAC #1 might be due to the pinhole not being exactly in the center of the table. If

this was the case, as the table turned, the pinhole would move across the laser beam. Since the laser beam intensity distribution is not uniform, DYNAC #1 would see an intensity variation which it might interpret as movement. To refute this conjecture, two tests were performed. First, the isolation transfer function $\theta_x(j\omega)/\theta_{Cx}(j\omega)$ was measured with and without intensity normalization. The same transfer function was achieved in both cases. This showed that the amount of light getting through the pinhole didn't change significantly as the table turned. Second, the isolation transfer function can be measured without using the ORG beam at all:

$$[(\text{DYNAC \#2}) - (\text{ESG x})]/(\text{DYNAC \#2}) = [\theta_{Cx} - (\theta_{Cx}-\theta_x)]/\theta_{Cx} = \theta_x/\theta_{Cx}, \quad (4\text{-}1)$$

which is the isolation transfer function. This measurement, although not very numerically reliable since $\theta_x << \theta_{Cx}$, gave the same general shape as the isolation transfer function measured by DYNAC #1/DYNAC #2. This also showed that DYNAC #1 was accurately measuring the movement of the ORG rotor.

As discussed in the "Basic Principles of the ORG" section (section 2), the two major extraneous torques on the rotor are gas and spring-restraints.

4.2.1.1 Gas Torques

For this section, assume the spring-restraint torques are zero. (In the next section it is shown that the spring-restraint torques are negligible anyway when the ORG spin speed is 89.4 Hz.)

Figs. 4.2-1 and 4.2-2 show the measured transfer functions of case angle about the x-axis to rotor angle about the x-axis ($\theta_x(j\omega)/\theta_{Cx}(j\omega)$) at low and high frequencies. The ORG was filled with He at 2 psi for these measurements.

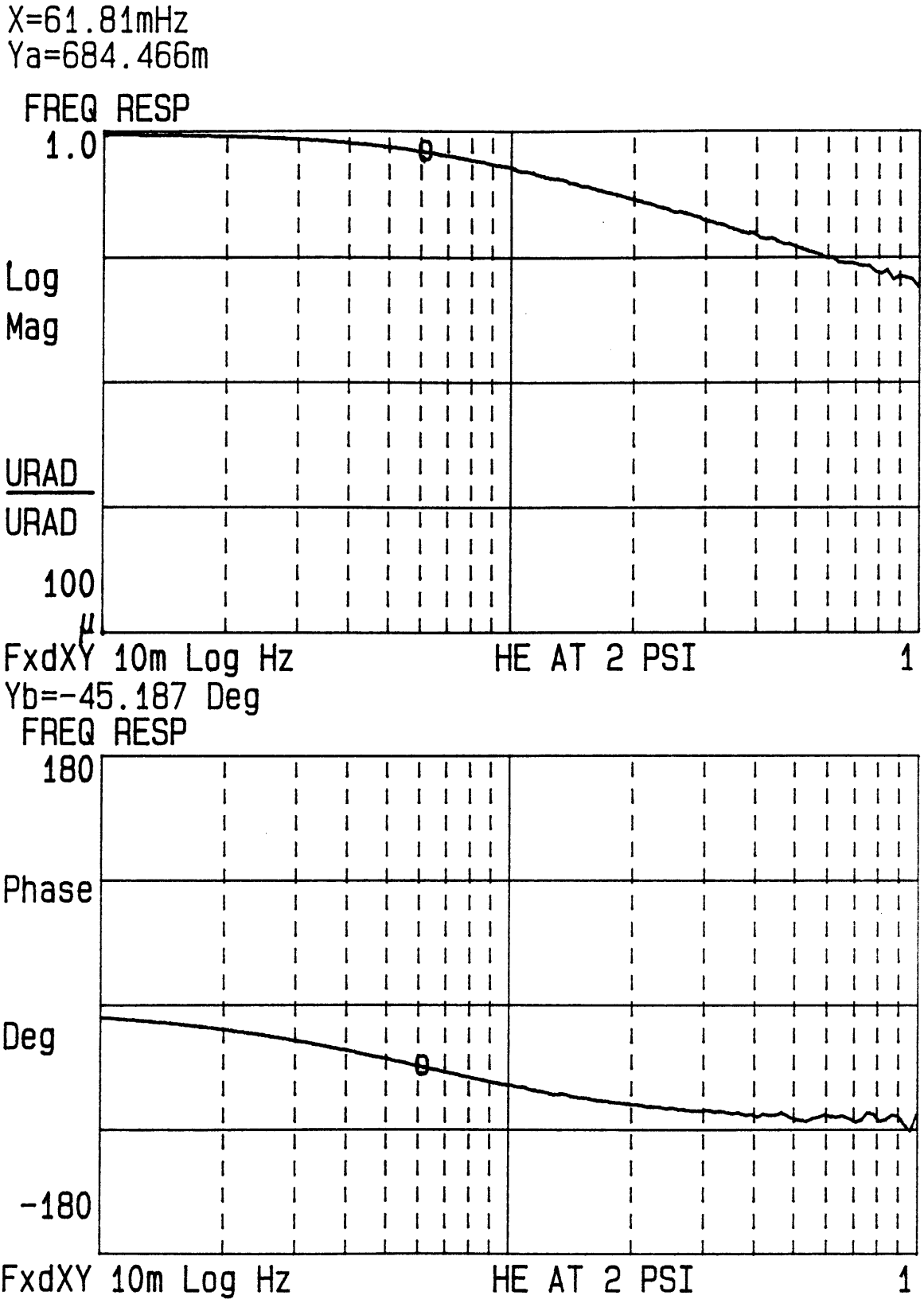

Figure 4.2-1. Low frequency portion of $\theta_X(j\omega)/\theta_{CX}(j\omega)$. ORG filled with He at 2 psi. ORG case moved ≈ ±50 μrad. Case movement measured by DYNAC. Rotor movement measured by OSG.

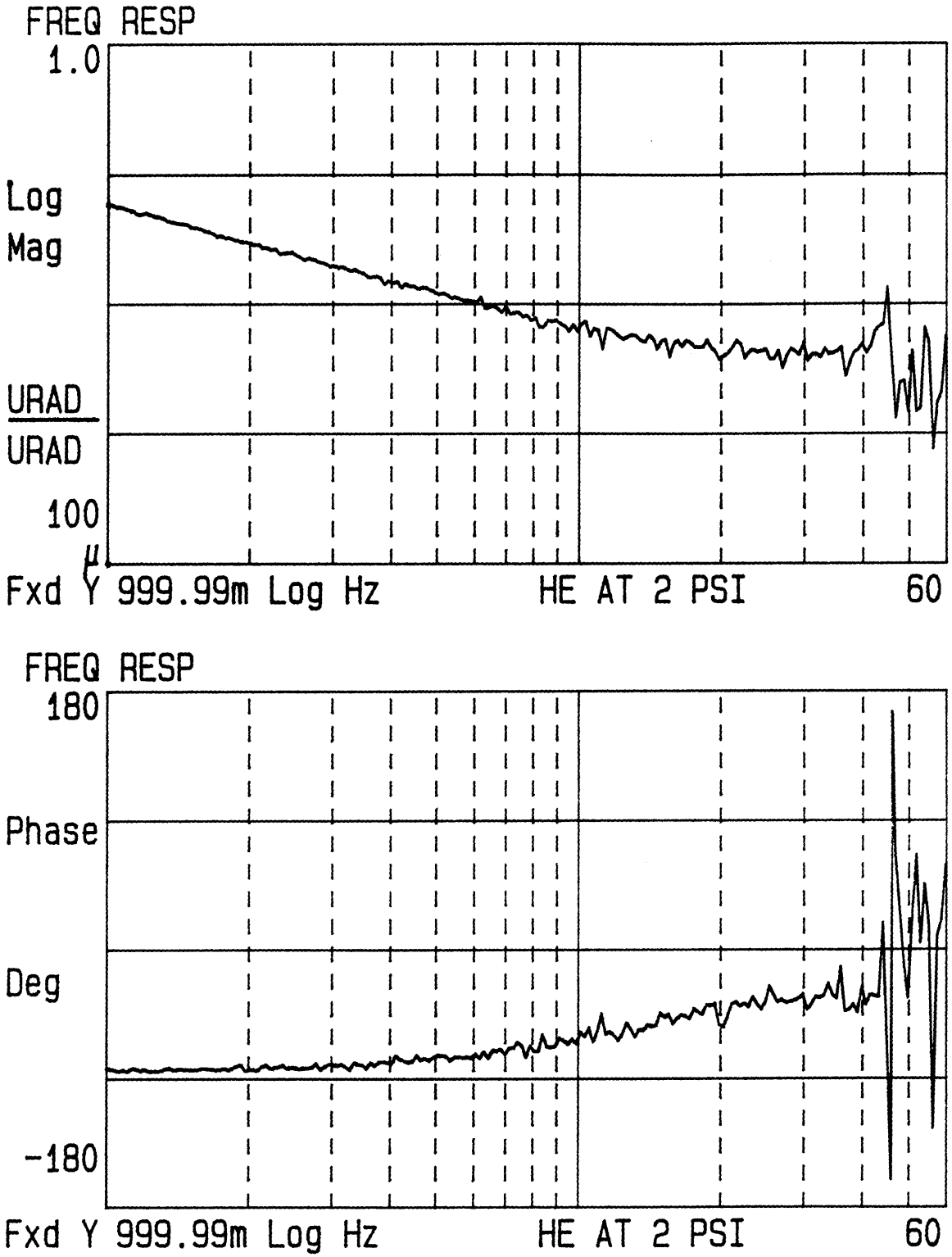

Figure 4.2-2. High frequency portion of $\theta_X(j\omega)/\theta_{CX}(j\omega)$. Status same as in previous figure.

The coupling between the case and rotor is 1:1 for very low frequencies, and then falls off at -20 dB/decade after 0.06 Hz until around 15 Hz. After 15 Hz the attenuation levels off.

Figs. 4.2-3 and 4.2-4 show the transfer function as predicted by the model given by equation 2-12. The damping coefficient c was calculated from the gyro time constant (see section 2.1.2). The time constant was calculated by dummy-directing the rotor within the case and measuring the time the rotor took to get 63% ($1-e^{-1}$) of the way back to null.

The measured and simulated transfer functions match very well below 15 Hz. Above 15 Hz, though, some unmodeled torques are being produced. It is believed that the rotor is experiencing a "squeeze film" effect. This means the rotor is experiencing some sort of air resistance at high frequencies.

Figs. 4.2-5 through 4.2-10 show the measured and simulated $\theta_x(j\omega)/\theta_{Cx}(j\omega)$ transfer functions for the ORG filled with air at 1 atm and the ORG with a near vacuum.

As less gas is inside the ORG, the rotor-to-case bandwidth moves to smaller frequencies, and the "squeeze-film" effect appears to move to higher frequencies.

The rotor also moves about the y-axis when the case is moved about the x-axis. Fig. 4.2-11 shows $\theta_y(j\omega)/\theta_{Cx}(j\omega)$ when the ORG has about 6 μm of Hg of air inside.

The transfer function magnitude is flat at about 0.003 and the phase is -180° from the $\theta_x(j\omega)/\theta_{Cx}(j\omega)$ bandwidth to at least 20 Hz.

Figs. 4.2-12 and 4.2-13 shows the corresponding computer simulation.

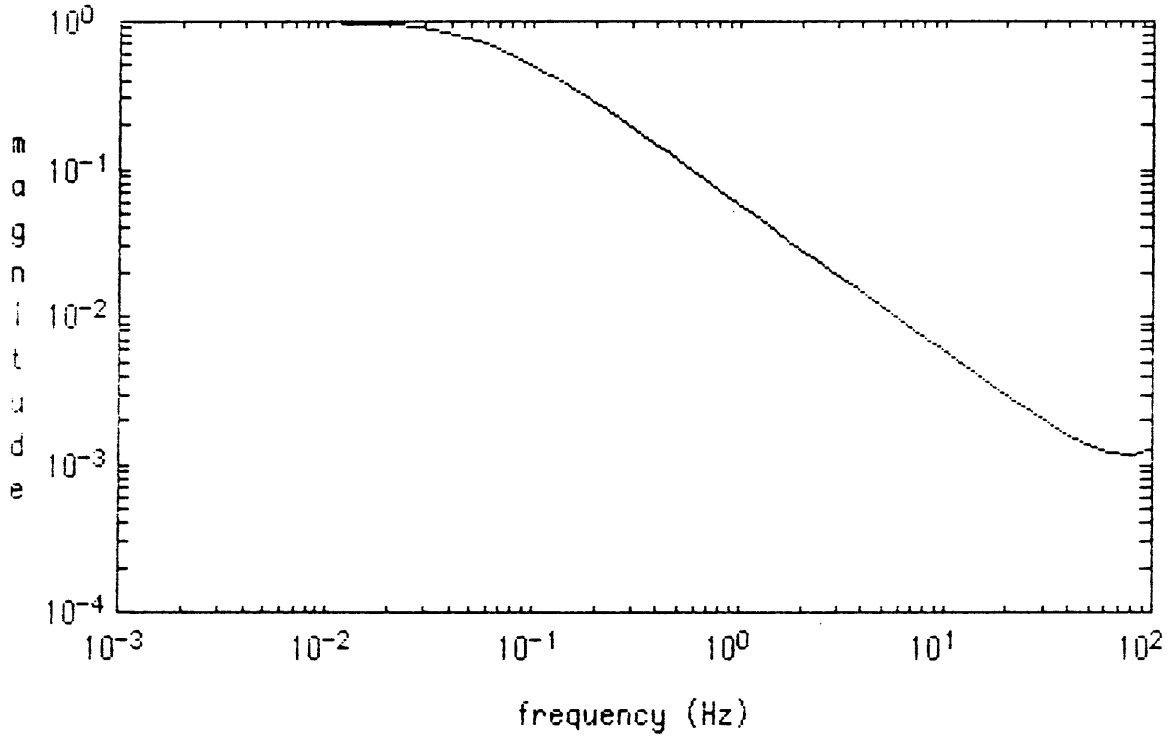

Figure 4.2-3. Computer simulation of $\theta x(j\omega)/\theta Cx(j\omega)$. Magnitude plot.

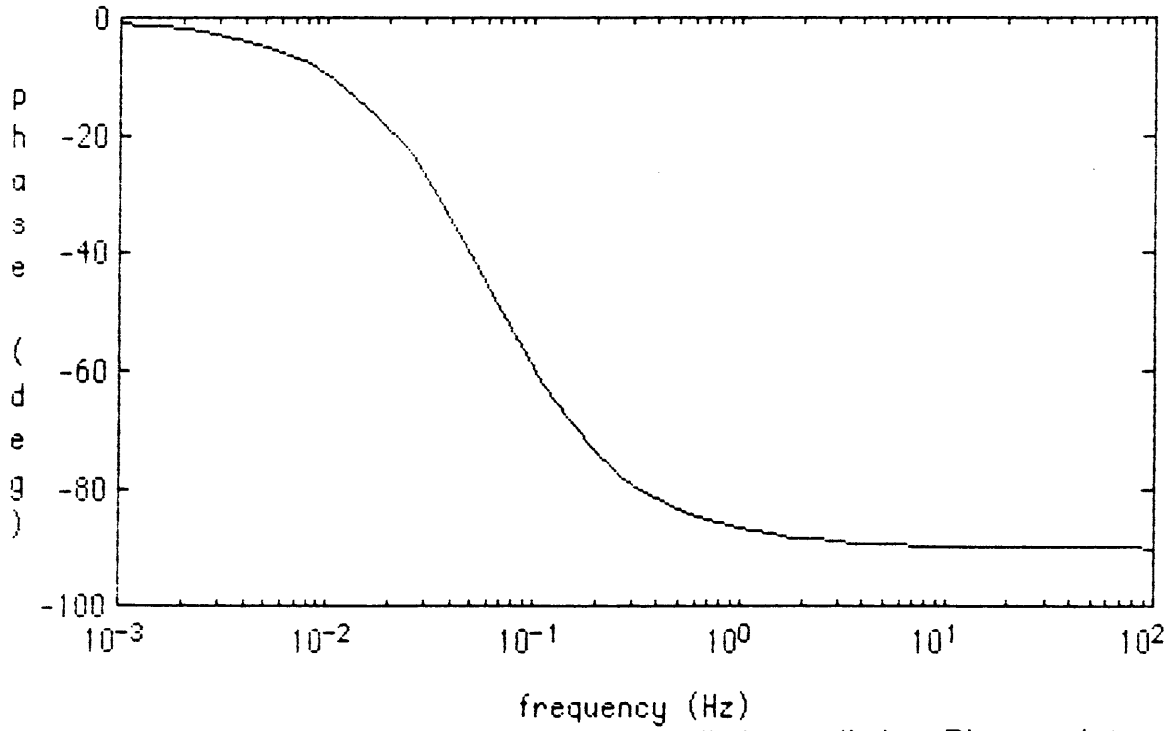

Figure 4.2-4. Computer simulation of $\theta x(j\omega)/\theta Cx(j\omega)$. Phase plot.

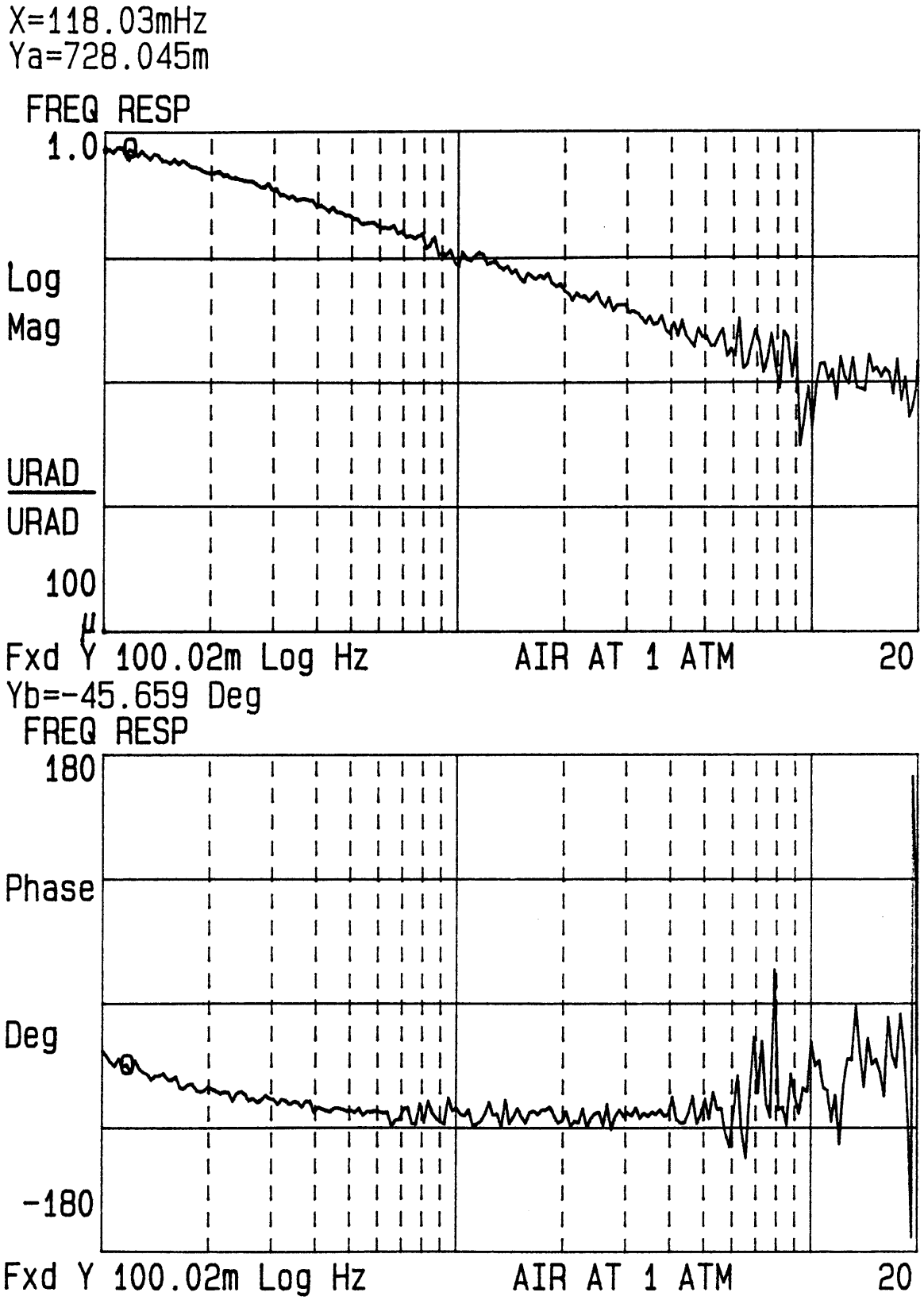

Figure 4.2-5. $\theta_X(j\omega)/\theta_{CX}(j\omega)$. ORG filled with air at 1 atm.

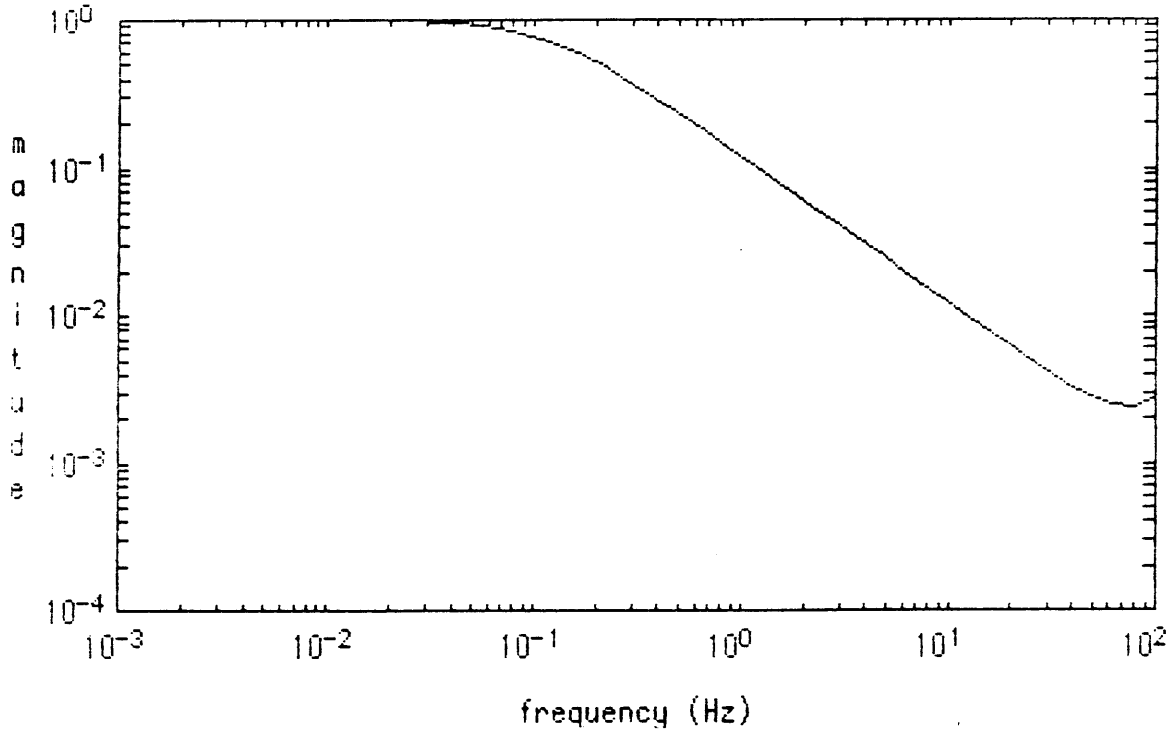

Figure 4.2-6. Computer simulation of $\theta_X(j\omega)/\theta_{CX}(j\omega)$. ORG filled with air at 1 atm. Magnitude plot.

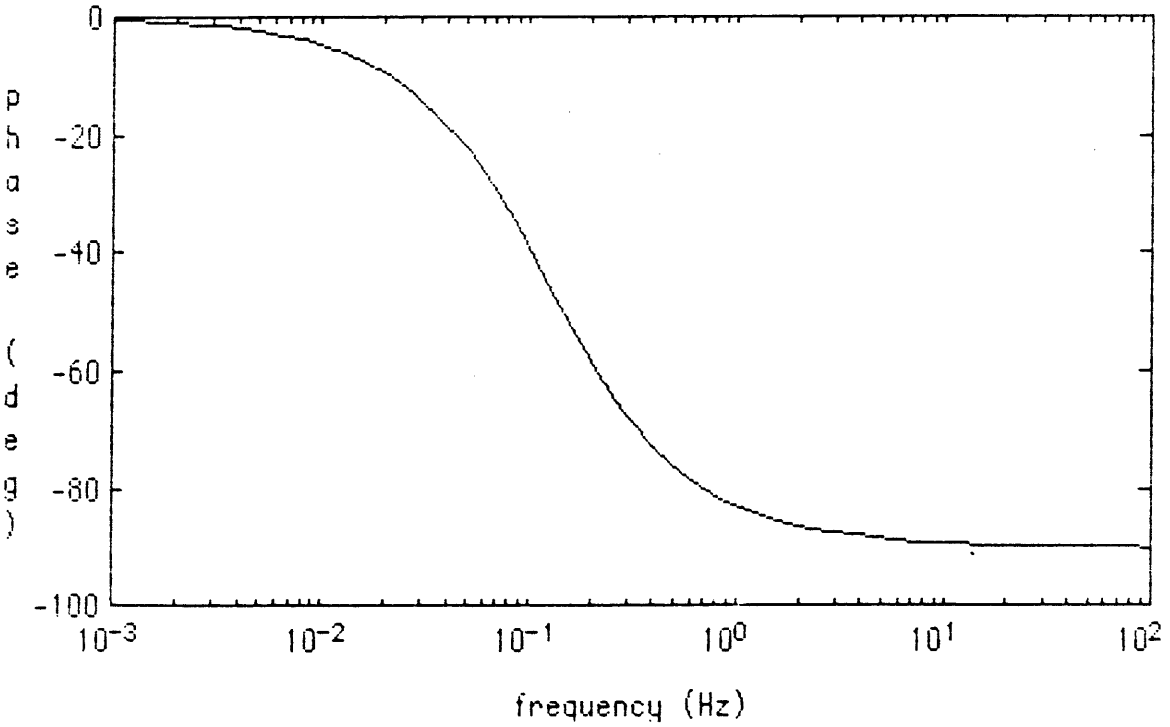

Figure 4.2-7. Computer simulation of $\theta_X(j\omega)/\theta_{CX}(j\omega)$. ORG filled with air at 1 atm. Phase plot.

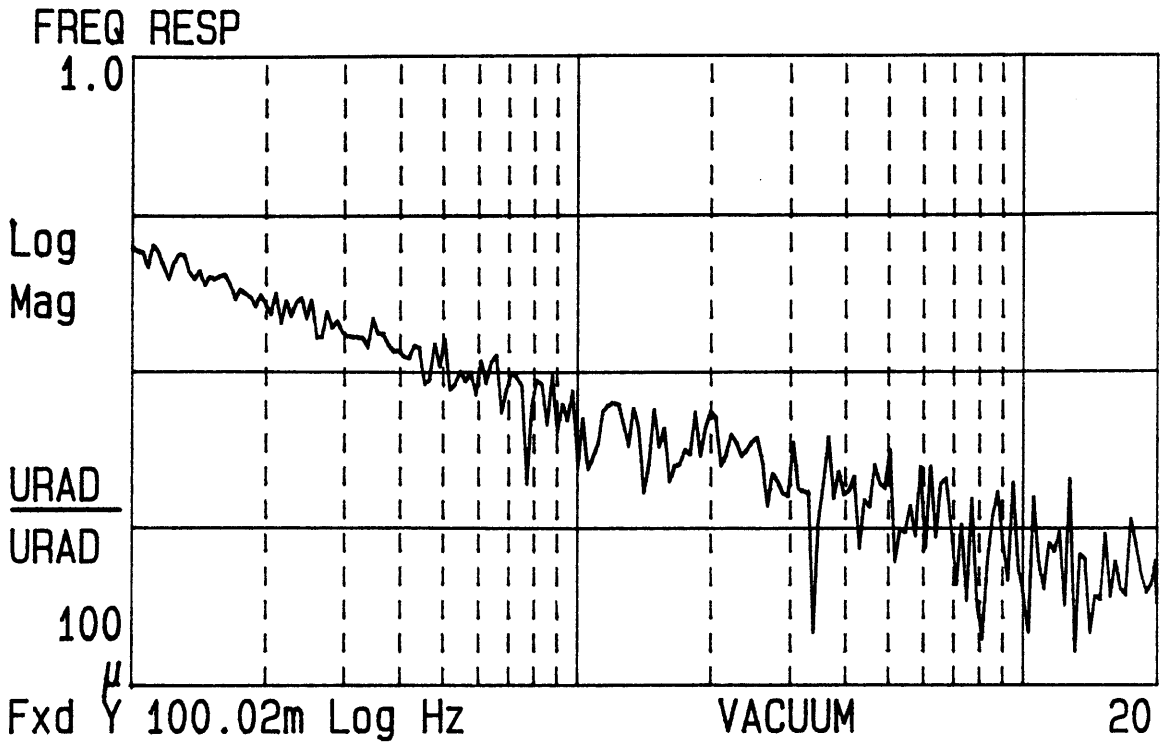

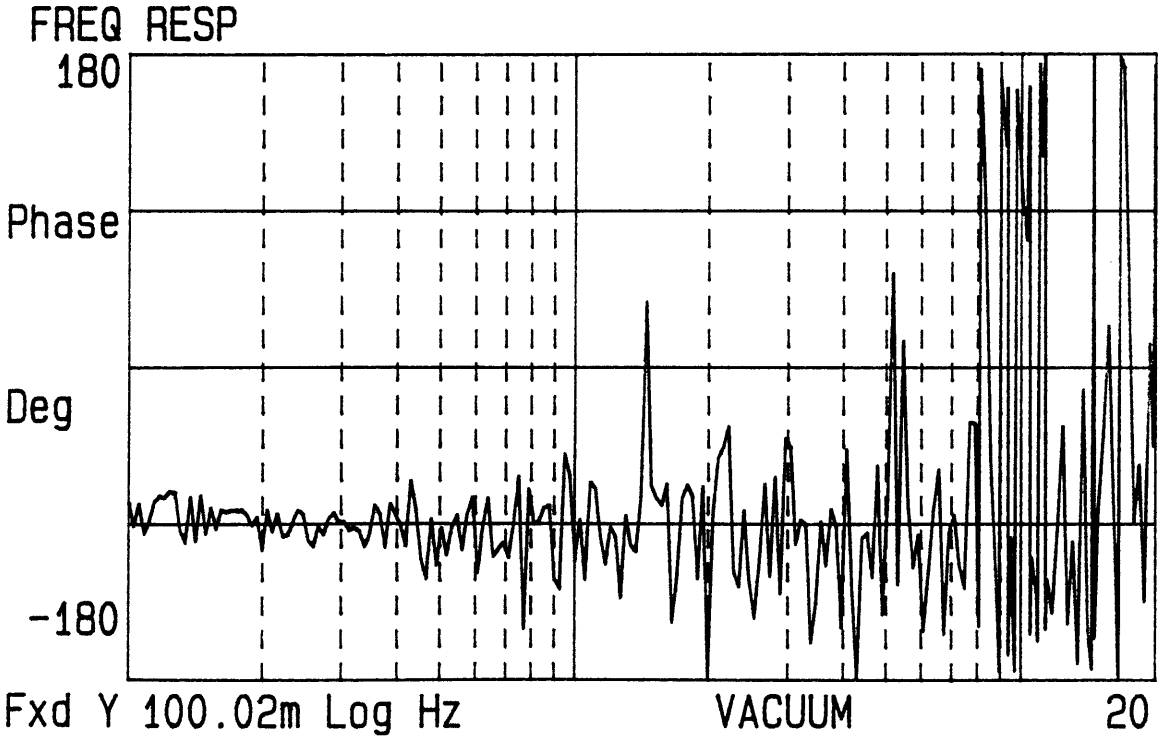

Figure 4.2-8. $\theta_X(j\omega)/\theta_{CX}(j\omega)$. ORG evacuated.

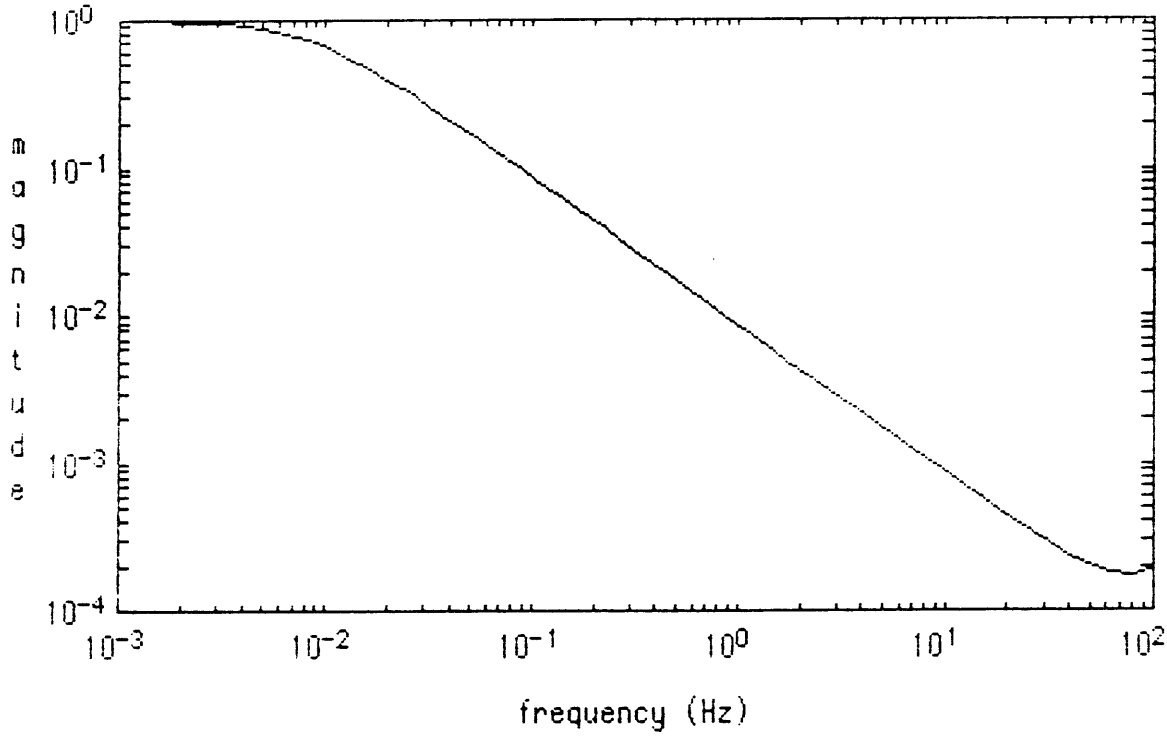

Figure 4.2-9. Computer simulation of $\theta x(j\omega)/\theta Cx(j\omega)$. ORG evacuated. Magnitude plot.

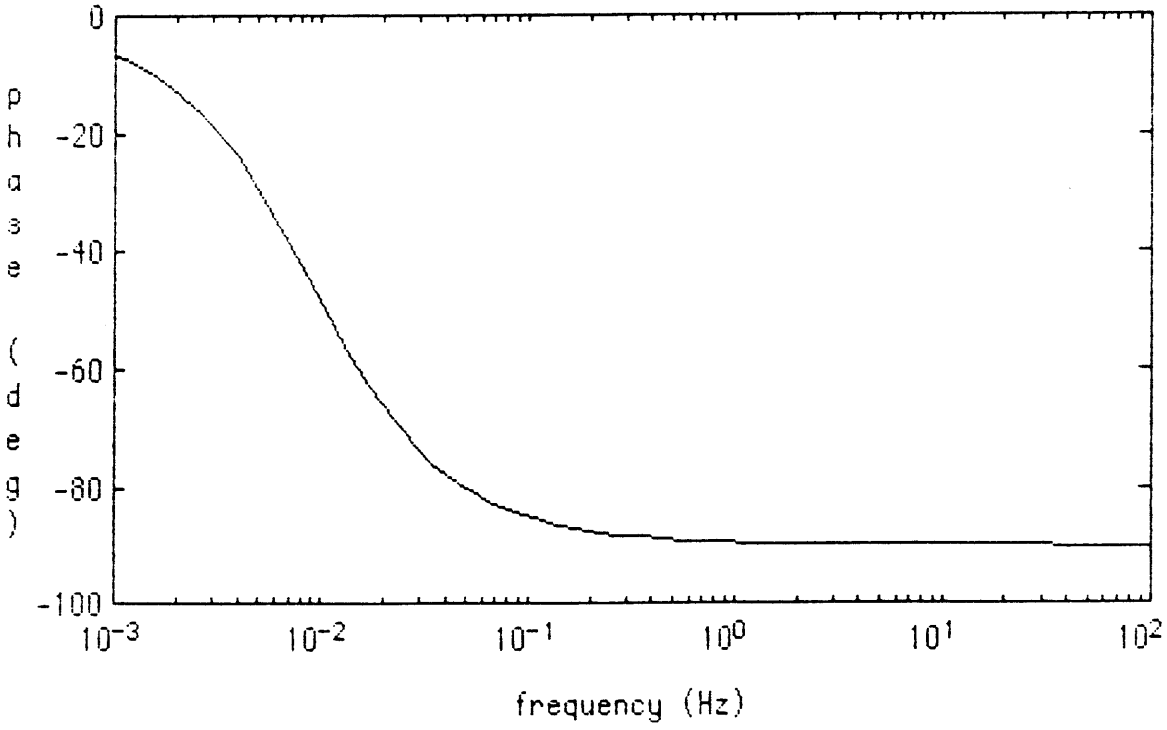

Figure 4.2-10. Computer simulation of $\theta x(j\omega)/\theta Cx(j\omega)$. ORG evacuated. Phase plot.

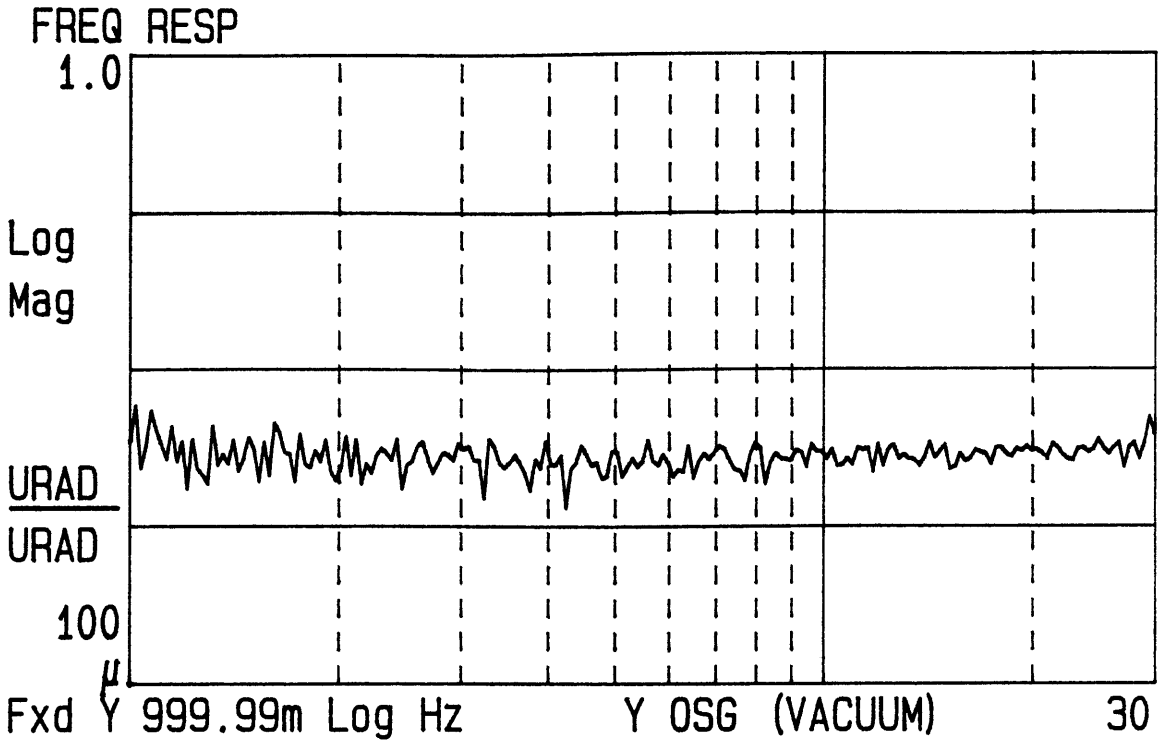

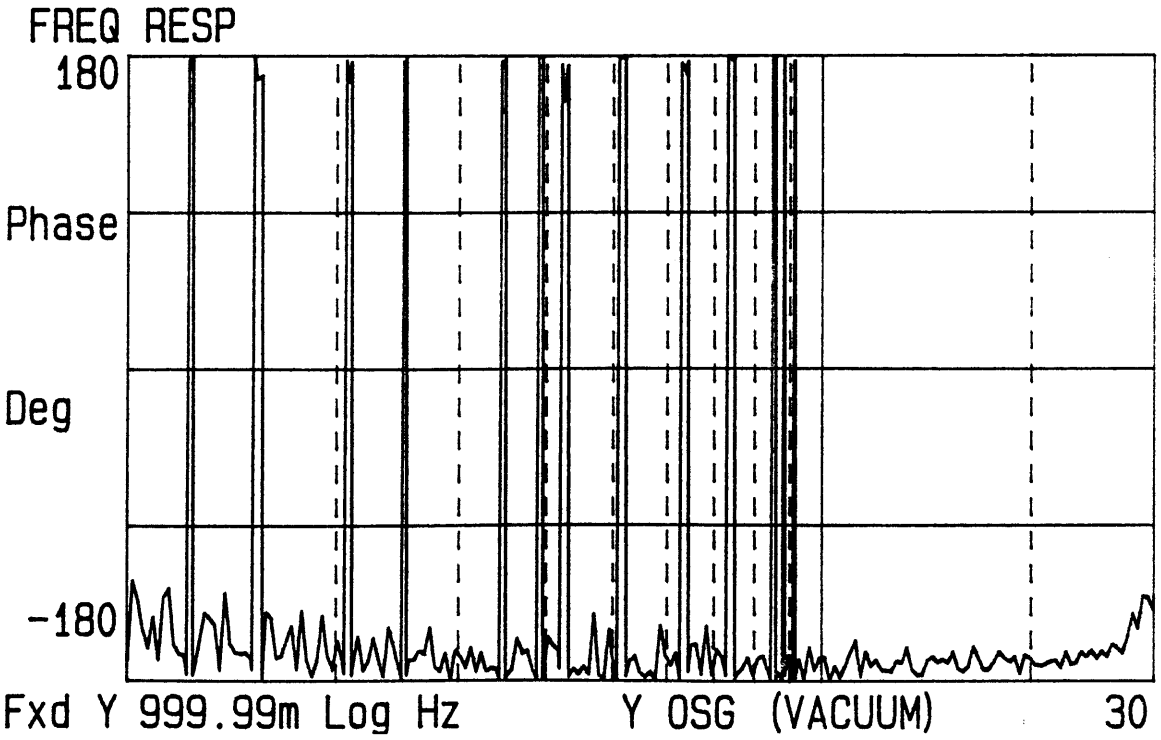

Figure 4.2-11. Measured $\theta y(j\omega)/\theta Cx(j\omega)$. ORG evacuated. ORG case moved ≈ ±75 μrad.

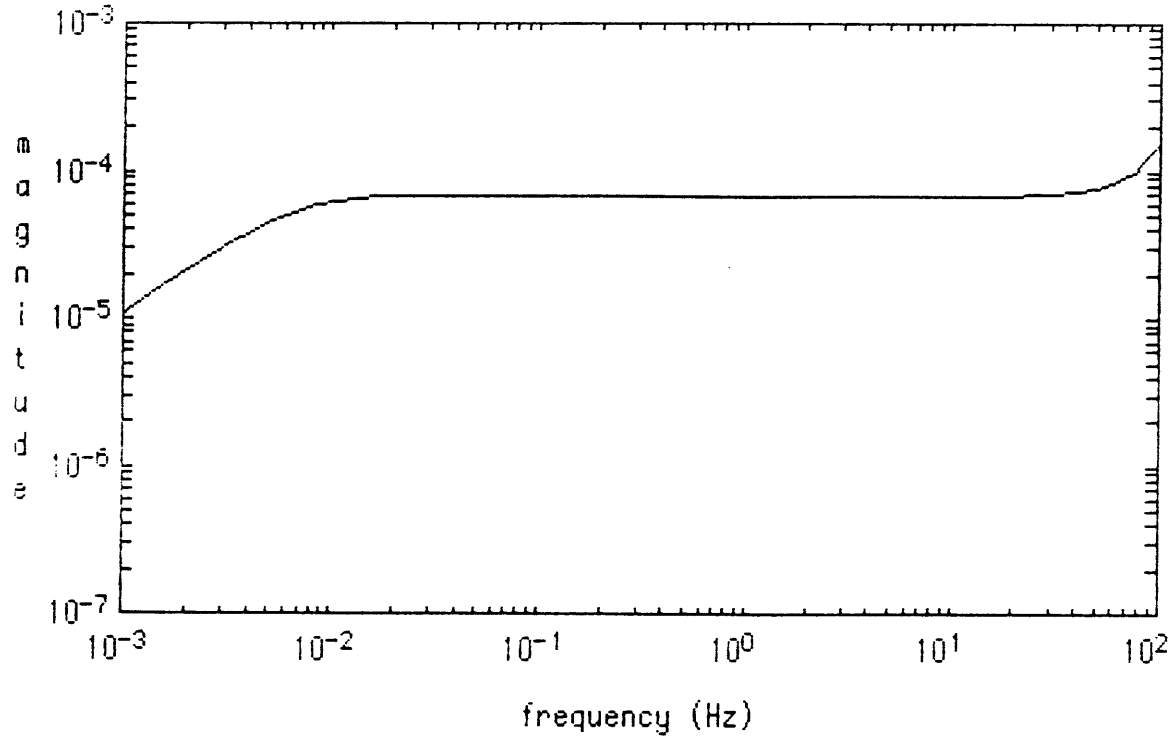

Figure 4.2-12. Computer simulation of $\theta y(j\omega)/\theta Cx(j\omega)$. Magnitude plot.

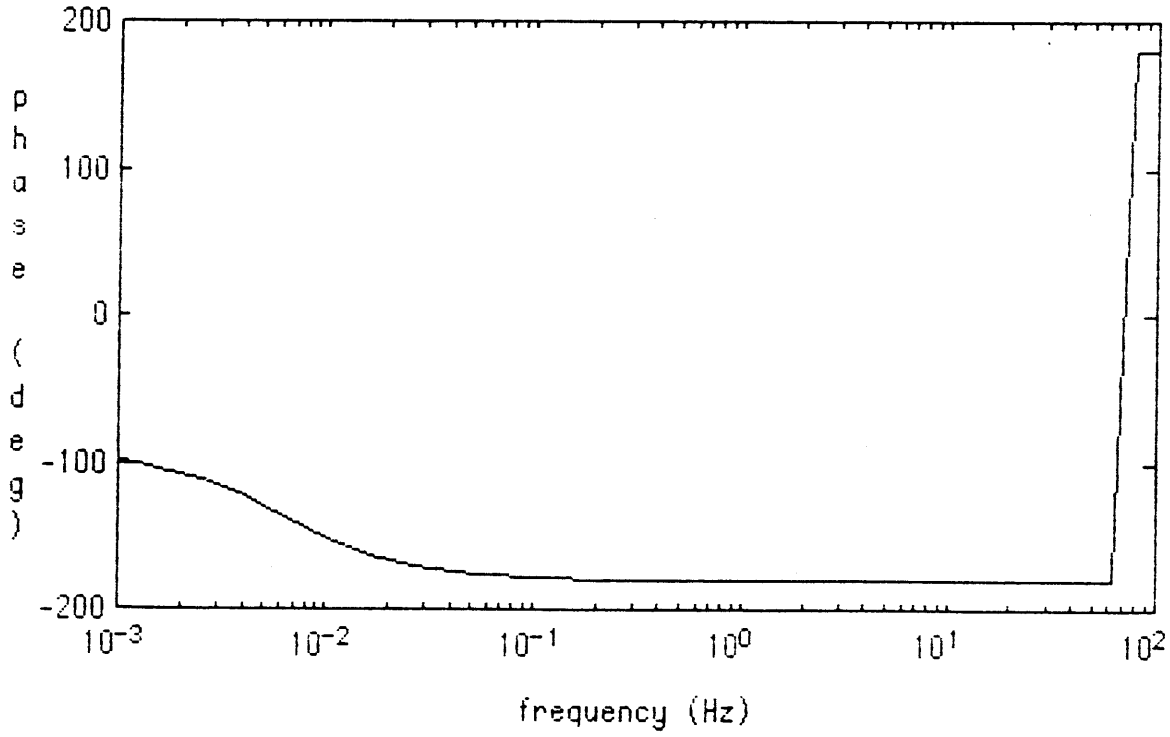

Figure 4.2-13. Computer simulation of $\theta y(j\omega)/\theta Cx(j\omega)$. Phase plot.

The simulated transfer function matches the measured transfer function well in shape and phase, but is off by about a factor of 30 in magnitude. It was thought that perhaps the increase in cross-axis movement was due to spring-restraint torques, but this cannot be the case since in the following section it is shown that the spring-restraint torques have a different phase. It was also thought there might have been a little direct-axis coupling of gas torques, but this would also produce a different phase.

4.2.1.2 Spring-Restraint Torques

Although the isolation transfer function appears to be well accounted for by the gas torques (at least below 15 Hz) this section investigates the possibility of spring-restraint torques. These torques need to be investigated because if all the gas could be removed (for example if the ORG was used in outer space), then the spring-restraint torques would most likely become the dominant torques.

Assume the spin frequency was off tuned speed by 1 Hz. This would result in a spring-restraint coefficient (see section 2.1.2) of

$$K-\omega_s^2 J = (3.5\times10^5 \text{ dyn-cm/rad})-[2\pi\times(89.4 + 1 \text{ Hz})]^2(1.1 \text{ gm-cm}) = -4100 \text{ dyn-cm/rad.}$$

Setting the gas torques to zero, and using equation 2-12, computer simulated transfer functions of $\theta_x(j\omega)/\theta_{Cx}(j\omega)$ and $\theta_y(j\omega)/\theta_{Cx}(j\omega)$ were generated. See figs. 4.2-14 and 4.2-15.

Like the gas torques, the spring-restraint torques cause the x-axis of the rotor to follow the case at very low frequencies. The bandwidth is much lower, though, than for gas even at 6 μm of Hg.

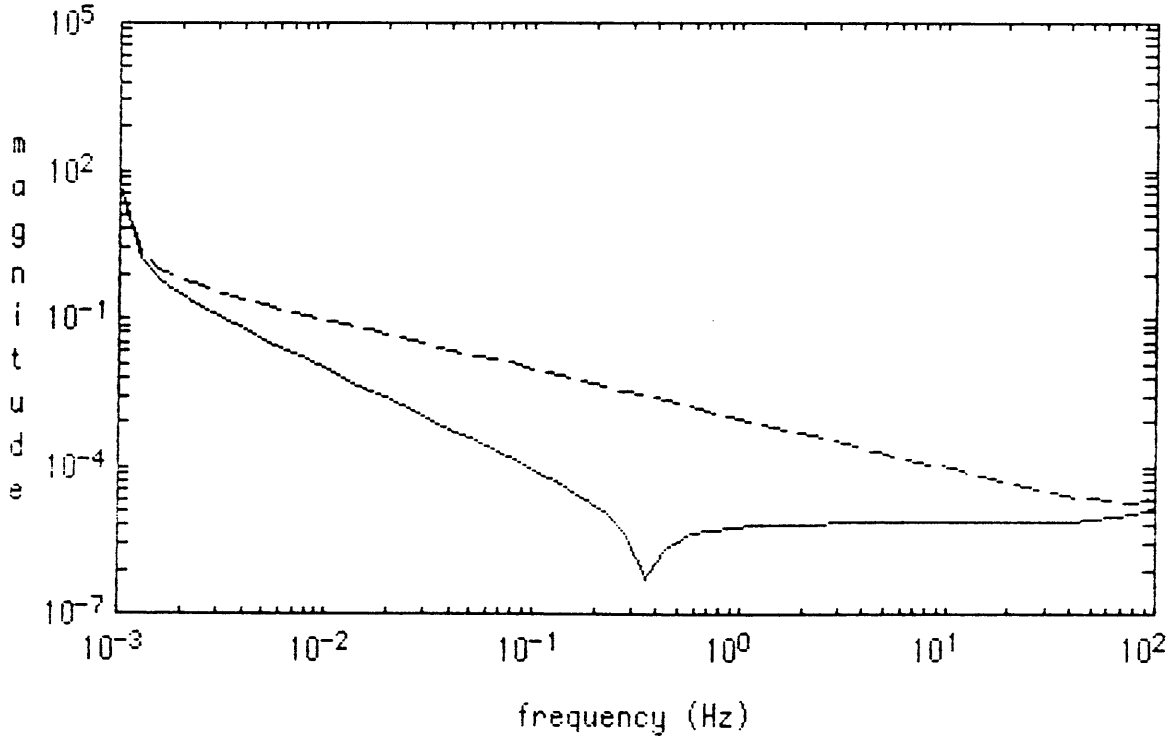

Figure 4.2-14. Computer simulation of $\theta x(j\omega)/\theta Cx(j\omega)$ and $\theta y(j\omega)/\theta Cx(j\omega)$. No gas torques. Magnitude plot.

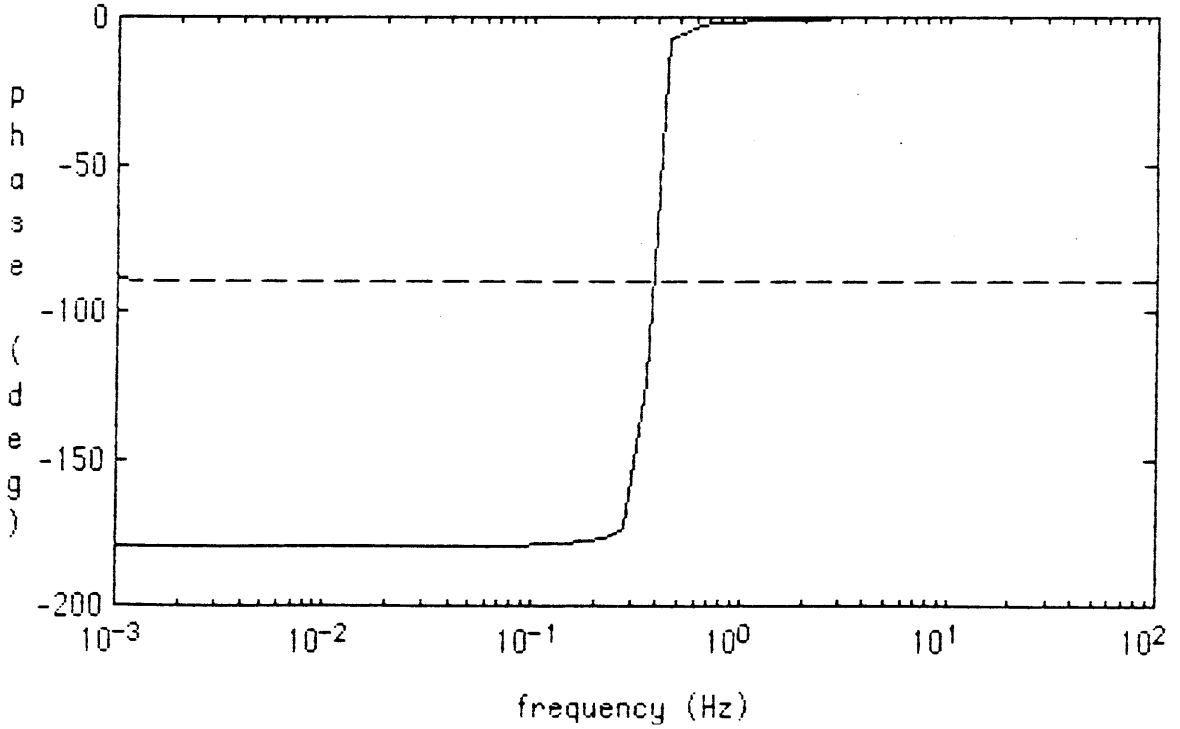

Figure 4.2-15. Computer simulation of $\theta x(j\omega)/\theta Cx(j\omega)$ and $\theta y(j\omega)/\theta Cx(j\omega)$. No gas torques. Phase plot.

Figs. 4.2-16 and 4.2-17 show the same transfer functions but with gas effects included.

The $\theta_x(j\omega)/\theta_{Cx}(j\omega)$ transfer function is basically the same as without spring restraints (compare to figs. 4.2-9 and 4.2-10), but the $\theta_y(j\omega)/\theta_{Cx}(j\omega)$ transfer function has noticeably changed. There is more coupling of the case to the y-axis of the rotor when spring-restraints are included.

Fig. 4.2-18 shows the measured $\theta_y(j\omega)/\theta_{Cx}(j\omega)$ transfer function when the spin speed was increased from tuned speed (89.4 Hz) by 0.84 Hz.

Like the simulation, there is more coupling of the case to the y-axis of the rotor with the wheel off speed.

4.2.2 Isolation Transfer Function With Eliminator

When the ORG is used as a pseudo-star, any noise in the OSG will be interpreted as movement in inertial space of the optical elements the ORG beam encounters including the optical detector. This false movement is in addition to the rotor movements caused by the case. Thus, the ultimate performance is limited by the sum of the OSG noise and the case-induced rotor movements. The discrete-frequency noises are the dominant noises in the OSG, and if these could be reduced, the pseudo-star performance would be improved dramatically.

The Eliminator was used on the OSG to remove the spin frequency noise. The isolation transfer function couldn't be measured beyond 60 Hz, though, because it took too much energy to move the platform enough to make a measurement above 60 Hz and because the platform wasn't very stiff above 60 Hz. The Eliminator did improve the quality of the measurements taken below 60 Hz, though, by improving the signal-to-noise ratio.

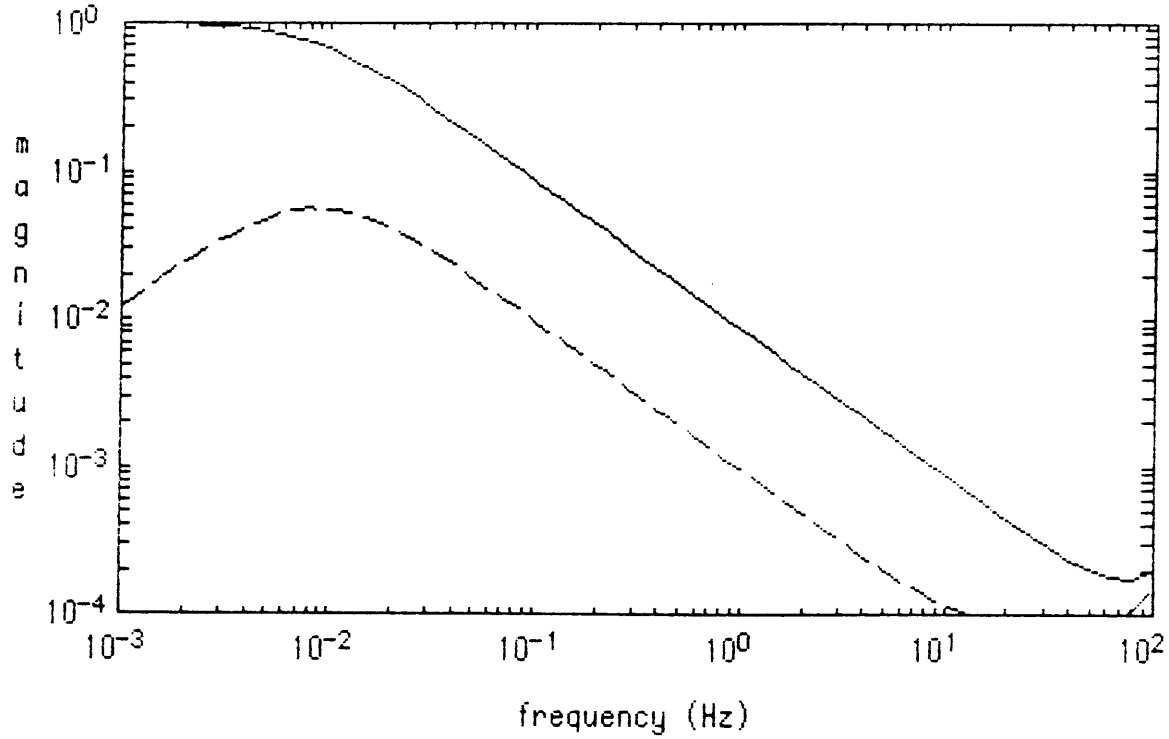

Figure 4.2-16. Computer simulation of $\theta x(j\omega)/\theta Cx(j\omega)$ and $\theta y(j\omega)/\theta Cx(j\omega)$. ORG evacuated. Magnitude plot.

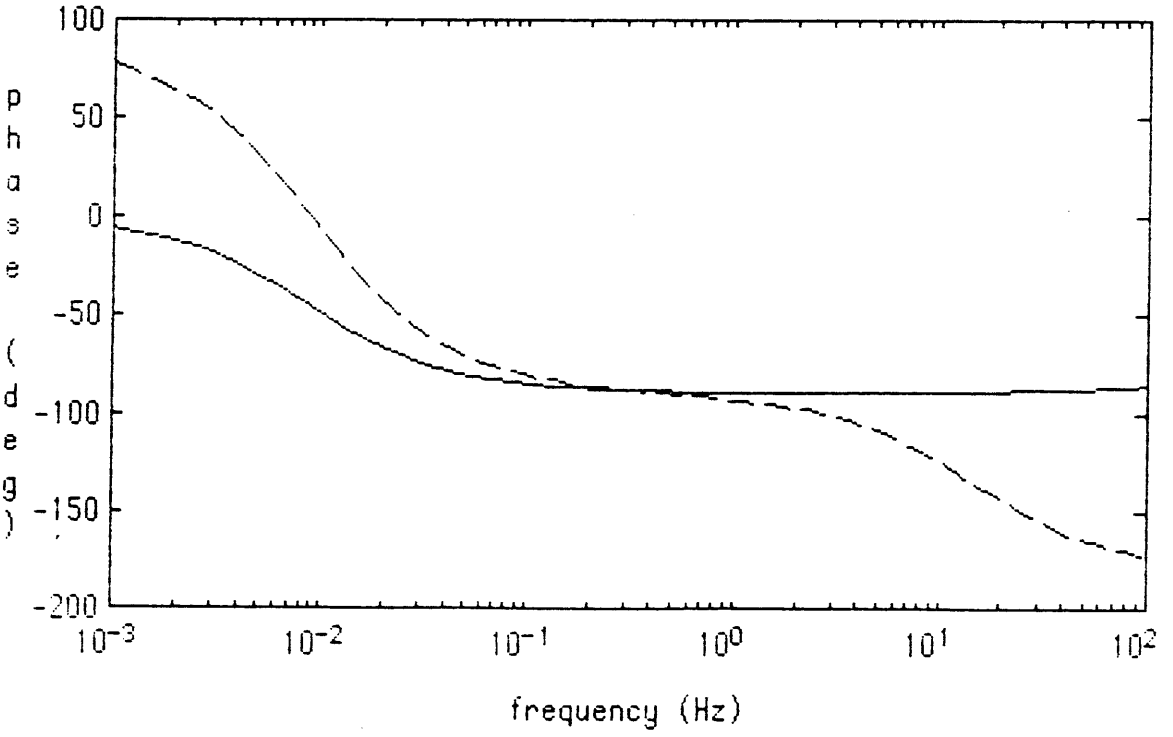

Figure 4.2-17. Computer simulation of $\theta x(j\omega)/\theta Cx(j\omega)$ and $\theta y(j\omega)/\theta Cx(j\omega)$. ORG evacuated. Phase plot.

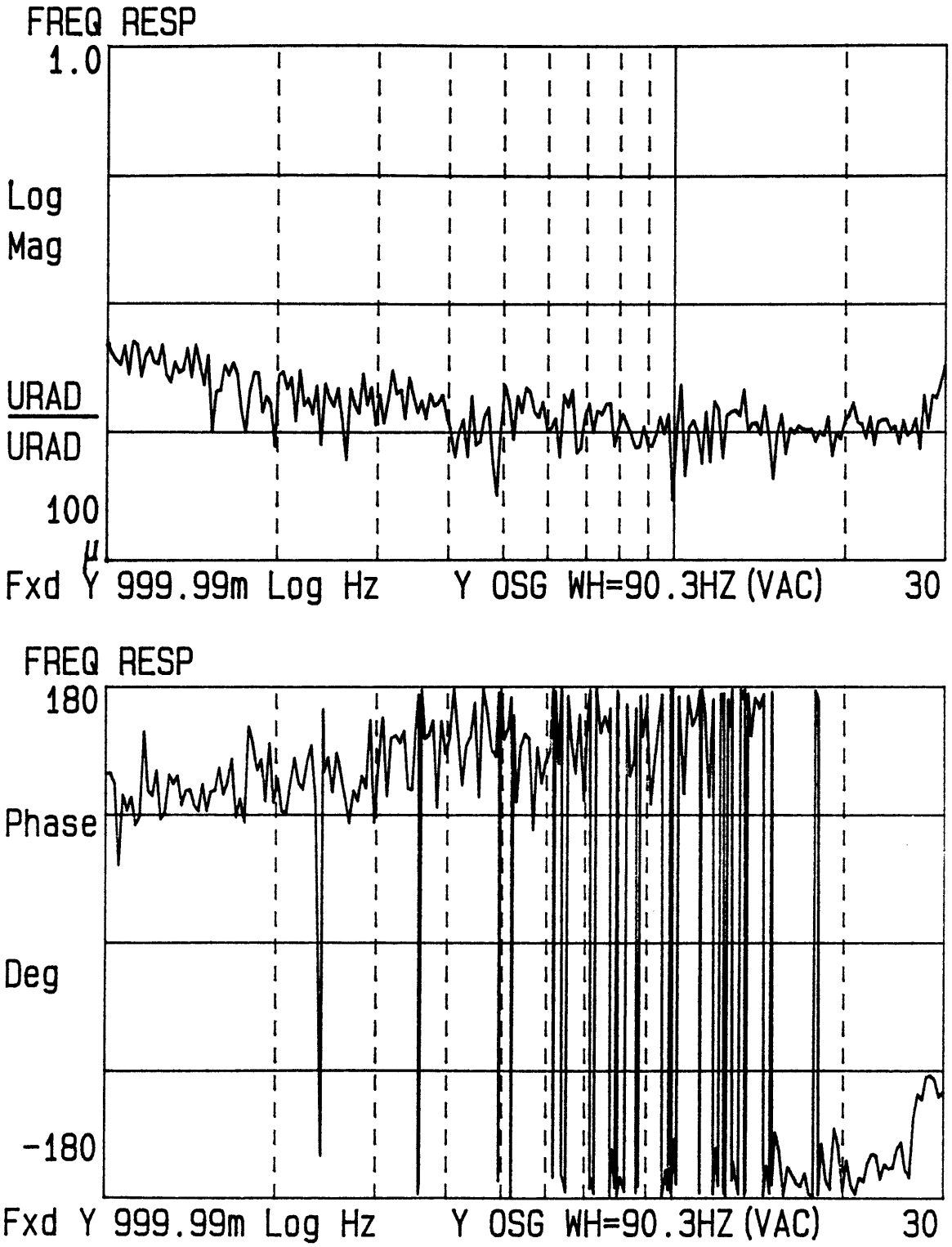

Figure 4.2-18. Measured transfer function $\theta y(j\omega)/\theta Cx(j\omega)$ with spin speed increased to 90.3 Hz. ORG evacuated.

The drawback to using the Eliminator in a pseudo-star application is it causes the rotor to follow the optical detector at and within ~±1 Hz of the spin frequency. In other words, motion of the optics train and detector at the spin frequency is reduced as well as the discrete-frequency noise.

4.3 Summary of ORG Performance Study

Nearly all of the coupling of the rotor to the outside world appears to be due to gas inside the ORG. When the rotor is spun at 89.4 Hz, the spring-restraint torques do not have a noticeable effect. The gas causes the rotor to follow the case at very low frequencies, and the coupling falls off as 1/s after a certain frequency. The amount of gas inside the ORG determines the bandwidth, and evacuating the ORG to a pressure of 6 μm of Hg decreased the bandwidth by about an order.

The Eliminator improves the isolation performance by removing the spin-frequency noise. The drawback to using the Eliminator, though, is it causes the rotor to follow the optical detector at and within ~±1 Hz (or whatever the ACL and PLL bandwidths are) of the rotor spin-speed.

5 Conclusions and Recommendations

5.1 Conclusions

The ORG beam performs well as a pseudo-star except for the following:

- The ORG beam contains wide-band noise primarily caused by backscatter into the light source, gas inside the ORG, and air outside the ORG.
- The ORG beam contains discrete-frequency noise at the spin-frequency and its harmonics that is much larger than the signal that must be measured.

• The beam is not inertially stable at very low frequencies and instead moves with the ORG case at very low frequencies. This coupling is primarily due to gas inside the ORG.

The performance was enhanced by the following:

• The wide-band noise was reduced by evacuating the ORG and aligning the light source properly.
• The discrete-frequency noise at the spin frequency was reduced to the wide-band noise by either the Subtraction Eliminator or the Torquing Eliminator. The rest of the signal was virtually unaffected. The performances of the Subtraction Eliminator and the Torquing Eliminator were nearly the same, except the Torquing Eliminator has the advantage in that it physically removes the discrete-frequency noise.
• The rotor-to-case coupling was reduced by about a factor of 10 by evacuating the ORG.

5.2 Further Work

There are several things that could be done to further improve the ORG and the Eliminator.

The following is further work to be done on the Eliminator:

1. Try a sample and hold on the ACL output. In other words, once the ACL has found the amplitude of the sinewave that exactly cancels the discrete-frequency noise, that value could be put into a sample and hold and the ACL turned off. Then if a real input occurred which had energy at the spin-speed, the output should contain that energy. In the current Eliminator, actual inputs near the spin speed are also attenuated. The reduction performance would drop though, especially over time.

2. Build an all-digital Eliminator using a computer.

3. Build more Eliminators to reduce the other spin-frequency harmonics.

4. Build a noise compensation system that will eliminate the entire periodic signal from the ORG output. Possibly this could be done by having a computer take a bunch of samples of the signal every period. Then each point in the sample could be individually used to control a point in an output signal. This output signal would then be subtracted (or torqued) from the gyro output. The sampled points would be driven to zero by ACL loops that would drive corresponding points in the output signal. Basically, the computer would be estimating the periodic signal in the gyro and subtracting (or torquing) it out. In this way, all the harmonics could be removed from the output, not just the fundamental.

5. Look into using the Eliminator for other applications, such as a replacement for the notch filter in the torque-rebalance loop. Also see how well the Eliminator can reduce lightly-damped resonances such as nutation.

The following is further work to be done on the ORG:

1. Investigate the use of a chopper to cut down the noise in the OSG due to air outside the instrument that the beam must pass through. The chopper wheel would be placed between the laser and the pinhole, and the output of the OSG would be read using a lock-in amplifier. The air noise falls off quickly with frequency. Thus by modulating the light to higher frequencies, the noise due to air could be substantially reduced.

2. Make the pinhole smaller. This would result in a larger angle to the first zero in the diffraction pattern, thus spreading out the light more. Currently, the diameter of the inner circle of the diffraction pattern is only about half the diameter of the aperture of the lens. If the light could be made to more uniformly fill the lens, the DYNAC would have a larger spot to look at and thus have a more linear

response. Note if the pinhole is made smaller, the light source will have to be brighter or else the ORG beam intensity will drop.

3. Try to quiet down the laser or find a quieter light source so the OSG wide-band noise may be reduced.

4. If a laser diode or LED will be used as a light source, look into keeping the intensity of the ORG beam constant by measuring it with a photocell and using the measurement to control the power going to the light source.

5. Try to reduce the backscatter going back to the light source. Don't make the surface around the pinhole so shiny. Perhaps paint it black or put the pinhole in the center of a convex surface so the light that doesn't go through the pinhole will be scattered away from the laser. Put in a Faraday isolator between the light source and the pinhole.

6. I had suggested putting a mirror on the rotor and reflecting a laser beam off the mirror and using that as the ORG beam. That idea is wrong! Using a mirror instead of a pinhole would make the ORG beam contain light source-to-inertia information, and the beam would not serve as a true pseudo-star. In other words, if the laser moved, the ORG beam would move.

7. Investigate further the use of an aperture to allow only the inner circle of the diffraction pattern in the ORG beam into the optical detector. This should cut down the spin-frequency harmonics in the OSG significantly.

8. Look into making a stiffer hinge so the spin speed may be increased. This will push the spin speed, nutation, and the spin-speed harmonics to higher frequencies.

9. Fix the torque-rebalance loops so they aren't so noisy.

References

1. Elwell, J.M. Jr., Carroll, R., *Guidance Seeker Definition and Analysis Program Final Report,* Draper Laboratory Report R-1347, November 1979.

2. Carson, R., Carroll, R., Kochakian, C., Walker, R., *Wheel-Speed Reversal,* Draper Laboratory Report CSDL-R-1942, January 1987.

3. Ohanian, Hans C., *Physics,* Vol. II, W.W. Norton & Company, New York, NY, 1985.

4. Best, R.E., *Phase-Locked Loops--Theory, Design, & Applications*, McGraw-Hill, New York, NY, 1984.

5. Gardner, F.M., *Phaselock Techniques*, John Wiley & Sons, Inc., New York, NY, 1966.

6. Elwell, J.M. Jr., Carroll, R., Leehey, J.R., McKern, R.A., *Forward Acquisition System Inertial Technology Development,* Draper Laboratory Report R-1444, April 1981.

7. Gilgen, R.L., *An Optical Alignment Transfer System for Tracking Dim Targets,* MIT Master's Thesis, Cambridge, MA, 1987.

8. Howe, E.W., Savet, P.H., "The Dynamically Tuned Free Rotor Gyro," *Control Engineering*, June 1964.

9. Craig, R.J.G., "Theory of Operations of an Elastically Supported, Tuned Gyroscope," *IEEE Transactions on Aerospace and Electronic Systems*, Vol. AES-8, No. 3, May 1972.

10. Stecyk, Adrian, Magee, Robert J., *DYNAC Interim Design Report,* Draper Laboratory Report CSDL-R-1773, March 1986.

3994-87